RECONFIGURABLE ANTENNAS FOR PUBLIC SAFETY AND WIRELESS GIGABIT ALLIANCE APPLICATIONS

by

Hema Swaroop Mopidevi

A dissertation submitted in partial fulfillment
of the requirements for the degree

of

DOCTOR OF PHILOSOPHY

in

Electrical Engineering

Approved:

Dr. Bedri A. Cetiner Major Professor	Dr. Doran J. Baker Committee Member
Dr. Jacob Gunther Committee Member	Dr. Ryan Gerdes Committee Member
Dr. T.C. Shen Committee Member	Dr. Mark R. McLellan Vice President for Research and Dean of the School of Graduate Studies

UTAH STATE UNIVERSITY
Logan, Utah

2014

Abstract

Reconfigurable Antennas for Public Safety and Wireless Gigabit Alliance Applications

by

Hema Swaroop Mopidevi, Doctor of Philosophy

Utah State University, 2014

Major Professor: Dr. Bedri A. Cetiner
Department: Electrical and Computer Engineering

This dissertation work builds on the concept of reconfiguring the antenna properties (frequency, radiation pattern) using Radio Frequency (RF) Micro Electro Mechanical Systems (MEMS) and pin-diodes. This is a part of the overall research performed at the RF Micro/Nano Electro Mechanical Systems (μNϵMS) Laboratory at Utah State University, which includes design, micro-fabrication, test, and characterization of μNϵMS integrated cognitive wireless communication systems.

To support multi-band multi-mode wireless communication systems for Public Safety (PS) applications, the design, fabrication, and characterization of a MEMS integrated antenna which operates over PS bands, e.g., 220 MHz, 470 MHz, 800 MHz, and 4.9 GHz while maintaining the integrity of radiation pattern, is accomplished. The second project involves the design, fabrication, and characterization of a pin-diode integrated beam steering Multi-functional Reconfigurable Antenna (MRA) operating over 4.94-4.99 GHz band which supports Multi-Input Multi-Output (MIMO) PS systems. As a final project, the design of a beam steering MRA and 2x1 Multi-functional Reconfigurable Antenna Array (MRAA) to operate over 57-66 GHz band for Wireless Gigabit alliance (WiGig) applications is accomplished.

(130 pages)

Public Abstract

Reconfigurable Antennas for Public Safety and Wireless Gigabit Alliance Applications

by

Hema Swaroop Mopidevi, Doctor of Philosophy

Utah State University, 2014

Major Professor: Dr. Bedri A. Cetiner
Department: Electrical and Computer Engineering

The main goal of this research is to develop a new type of antenna, called reconfigurable antenna, which can replace multiple antennas required to enhance the effectiveness of a robust communication system. A reconfigurable antenna integrated with switching elements can dynamically change its properties, namely, frequency of operation, radiation pattern (the three-dimensional coverage of antenna), and polarization (the electrical orientation of the antenna). Depending on the requirement, a single antenna can function as multiple antennas, therefore, the name Multi-functional Reconfigurable Antenna (MRA). United States (US) Public Safety (PS) responders (police, fire-fighters, emergency medical services, etc.) can effectively respond to human-made or natural catastrophies if they are equipped with robust communication systems supported by MRA. Wireless implementations of computer accessories (wireless HDMI, wireless storage to external hard-drive, etc.) that require high speed data communication are supported by 60 GHz communications. Equipping these devices with MRA could further increase the speed of communication, thereby resulting in a robust communication.

In this work, pin-diodes and Micro Electro Mechanical Switches (MEMS) are integrated on the MRAs to reconfigure (dynamically change) its properties namely frequency and radiation pattern. An MRA capable of operating over 220, 470, 800, 4900 MHz PS bands

is designed, manufactured, tested, and characterized. Another MRA capable of changing its radiation pattern over 4.94-4.99 GHz band is designed, manufactured, tested, and characterized. The design of radiation pattern reconfigurable MRA and Multi-functional Reconfigurable Antenna Array (MRAA) for 60 GHz communication is also accomplished. The MRAA is designed in order to enhance the MRA's capability to receive or transmit more power.

Dedicated to the Almighty, Sarvam Shree Uma Maheshwara Parabrahmarpanamastu!

Acknowledgments

I would like to express my highest regards and gratitude to my advisor and mentor, Dr. Bedri A. Cetiner, who believed in me right from the beginning of my career as a research assistant at USU. He not only gave me the required knowledge to pursue my research through the subjects he taught, but also always gave the required moral support during my hard times. He inculcated in me a never-ending motivation and zeal towards my research efforts, as well as encouraged my presentation skills on a regular basis. I would like to express my gratitude to Dr. Mehmet Unlu, who shared his vast practical knowledge on MEMS which was used in one of the projects. I would like to thank my committee members, Dr. Ryan Gerdes, Dr. T.C. Shen, Dr. Doran Baker, and Dr. Jacob Gunther, who extended their support. I would also like to thank Dr. Oguz Kaynar, a visiting scholar from Turkey, for sharing his expertise on multi-objective genetic algorthims.

I would like to thank all my friends in Logan: Rajsekhar, Susheel, Swathi, Jahnavi, Karthik, Amrita, Harsha, Vikranth, and the list goes on. I never felt lonely or dejected, and the only reason I never missed my parents is the unending support they have given. I would also like to thank my friends at RF MEMS lab: Zhouyuan; Dani, who was our visiting scholar from Spain; Yuan; and Yasin for their help on various occasions. I would like to especially thank Dani for sharing his expertise on antenna design.

I would also like to thank my wife's brother and his family for having taken care of me in hard times. Lastly, the constant love and affection from my family (including my parents and wife) is the backbone of any successful endeavor in my life. Without their constant support and encouragement for quality education I would never have achieved the right kind of exposure to fulfill my dream of working in my area of interest.

Hema Swaroop Mopidevi

Contents

List of Tables

List of Figures

Acronyms

3-D	Three-Dimensional
BCB	Benzocyclobutene
BW	Bandwidth
CB	Conductor-Backed
CPW	Coplanar Wave Guide
Cu	Copper
EM	Electro Magnetic
GHz	Giga Hertz
Gnd	Ground
HFSS	High Frequency Structure Simulator
LTCC	Low Temperature Co-fired Ceramic
LTE	Long Term Evolution
MEMS	Micro Electro Mechanical Systems
MHz	Mega Hertz
MIMO	Multi-Input Multi-Output
MRA	Multi-functional Reconfigurable Antenna
PCB	Printed Circuit Board
PIFA	Planar Inverted-F Antenna
PS	Public Safety
QAM	Quadrature Amplitude Modulation
RF	Radio Frequency
SEM	Scanning Electron Microscope
SMD	Surface Moutable Devices
SOL	Short Open Load
US	United States
WiGig	Wireless Gigabit alliance

Chapter 1

Introduction

The need for the efficient use of and easy access to the electromagnetic spectrum, a limited precious natural resource, is driving the recent development efforts on the interoperable multi-band multi-mode wireless communication systems. Such robust communication systems are needed for the United States (US) Public Safety (PS) agencies while dealing with natural or man-made catastrophes which result in band congestion. To improve the effectiveness of such systems, advanced antenna design and manufacturing techniques become important. Accordingly, a single antenna capable of operating in the PS bands-220, 470, 800, and 4960 MHz is advantageous in reducing the overall size and cost of the communication system.

Also, the scarcity of electromagnetic spectrum and explosive demand for higher data rates has led to the developmental efforts on multiple-input multiple-output (MIMO) systems in different dimensions. Particularly, the use of multiple transmitting and receiving antennas facilitate in generating multiple streams of data for enhanced spectral efficiency and increased capacity of MIMO systems [1]. However, using multiple antennas in a MIMO system causes a significant increase in cost, size, and radio-frequency (RF) power consumption due to multiple RF chains. Also, the mutual coupling of multiple antennas in array configuration reduces the MIMO system capacity [2]. A multi-functional reconfigurable antenna (MRA) [3–5] with enhanced pattern reconfigurable properties can replace the multiple antennas of a MIMO system to alleviate these drawbacks. This type of spectrally efficient wireless communication finds particularly useful for United States (US) Public Safety (PS) applications. Especially, the 4940-4990 MHz frequency band is narrow and often congested while dealing with natural or man-made calamities. In order to enable the PS personnel (e.g., police, fire-fighters, and emergency medical services) with spectrally efficient commu-

nication, a pattern reconfigurable antenna capable of providing beams in different directions at 4960MHz is desirable. For this purpose, a parasitic layer based pattern reconfigurable antenna is chosen.

The same parasitic layer based pattern reconfigurable technology can be quite useful in enhancing Wireless Gigabit alliance (WiGig) communications (IEEE 802.11ad protocol - 60 GHz communication). As the ever increasing demand for higher data rates continues, WiGig wireless technology (57 - 66 GHz) enabling wireless data, voice, and video applications at multi-gigabit speeds has recently been attracting much interest in both academia and industry [6]. At mm-wave frequencies ($\sim$60GHz WiGig) the antenna design and manufacturing posses some challenges due mainly to the small dimensions, which may be as small as $\sim 20\mu$m, and lossy material characteristics that are deleterious for antenna performances. Therefore, not only an effective micro-fabrication approach along with appropriate material use must be adopted, but also such considerations as being low-cost, compact, and easy integration with transceiver must be taken into account.

The objectives of this dissertation are as follows:

- Design, fabrication, and characterization of a single antenna capable of operating in the following PS bands - 220, 470, 800, 4900 MHz while maintaing pattern integrity;
- Design, fabrication, and characterization of a parasitic layer based pattern reconfigurable antenna operating over 4940 - 4990 MHz band providing nine different beam directions pertaining to: $\theta \in \{-30^o, 0^o, 30^o\}$; $\phi \in \{-45^o, 0^o, 45^o, 90^o\}$;
- Design, fabrication, and characterization of a parasitic layer based MRA and linear MRAA operating over 57 - 66 GHz band providing nine different beam directions pertaining to: $\theta \in \{-30^o, 0^o, 30^o\}$; $\phi \in \{-45^o, 0^o, 45^o, 90^o\}$.

1.1 Research Flow of Objective 1

To design a single antenna capable of operating in the PS bands- 220, 470, 800, and 4960 MHz, the following design methodologies are available in the literature, a multi-frequency antenna to cover each band [7–12], a broadband antenna to cover the entire frequency

range [13–16], a frequency reconfigurable antenna capable of tuning to the desired band of operation [17–19], or a multi-layered array configuration to operate at distant resonances [20, 21]. In the first and second design methodologies (see Figures 1.1 and 1.2) [7,14] maintaining the integrity of radiation pattern becomes increasingly difficult as the frequencies become wide apart. The third option shown in Figure 1.3 [17] may provide a compact design with pattern integrity. However, using a large number of switches to cover widely spaced multiple frequency bands complicates the biasing networks in the architecture [19]. The multi-layered array antenna, shown in Figure 1.4 [20], requires multiple layers fed separately which reduces the compactness of design.

In this work, an intelligent combination of the aforementioned techniques [7, 13, 19, 20] has lead to a robust and compact antenna design with simple architecture capable of providing radiation pattern integrity at all the PS bands. Before presenting the final

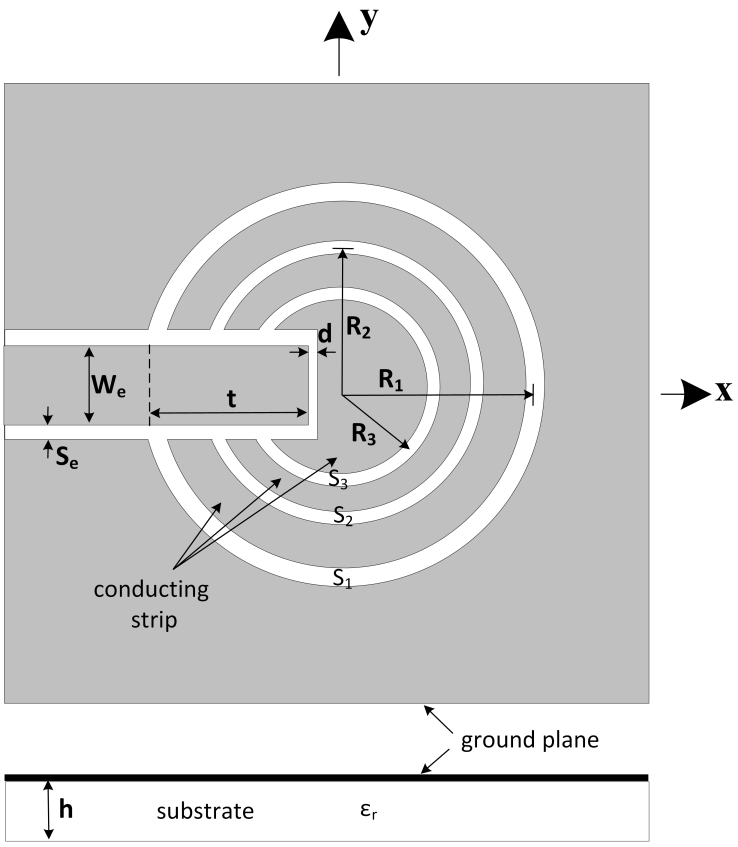

Fig. 1.1: Geometry of CPW-fed multi-frequency annular-ring slot antenna.

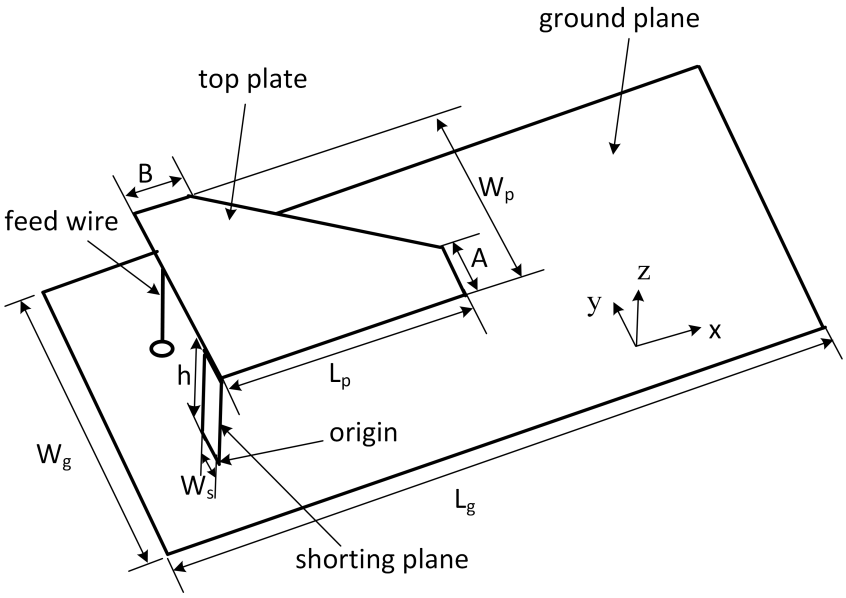

Fig. 1.2: Configuration of broadband tapered type PIFA.

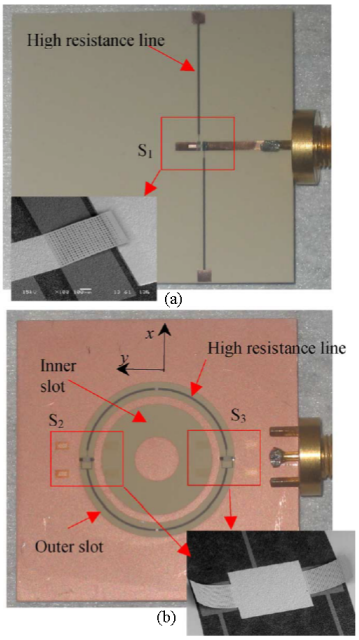

Fig. 1.3: Photograph of reconfigurable antenna annular-slot (a) Microstrip feed-line integrated with a single-arm Micro Electro Mechanical Systems (MEMS) actuator, and (b) Annular-slot integrated with two double-arm MEMS
actuators.

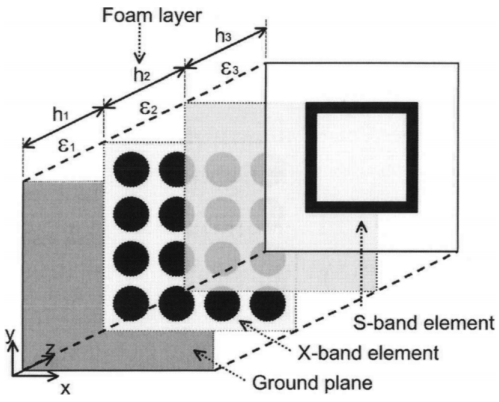

Fig. 1.4: The multi-layer structure of the dual-band dual-polarized array antenna.

design, the evolution of prototype is shown in a sequence of dissertation chapters. Chapter 2 presents a broadband antenna capable covering 400 - 800 MHz band while preserving the integrity of radiation pattern. Chapters 3 and 4 present frequency reconfigurable antenna designs, and finally Chapter 5 shows the final working prototype of the novel antenna which uses an intelligent combination of the above mentioned techniques [7, 13, 19, 20] to cover all the PS bands.

1.2 Research Flow of Objective 2

In Chapter 6 of this work, the design, fabrication, and characterization of a parasitic layer based [22, 23] pattern reconfigurable antenna operating over 4.94-4.99 GHz band are presented. The advantages of integrating switches on a parasitic layer as opposed to within the active antenna region are described in Yuan et al. [23]. The pattern reconfigurable antenna consists of a coaxial fed patch with a parasitic layer on top. The MRA design presented offers enhanced pattern reconfigurable functionalities with beams pointing in nine different directions when compared to design in Rodrigo et al. and Yuan et al. [22, 23]. The parasitic layer achieves this by utilizing only 3 x 3 metallic patches (called pixels) as opposed to the use of 5 x 5 pixels in the designs of Rodrigo et al. and Yuan et al. (see Figure 1.5 [22, 23]). This translates to minimizing the number of switch interconnections on the reconfigurable pixel parasitic while enhancing the beam diversity. Pin-diodes are used as

switching elements in this MRA due to their attractive features like low actuation voltage and high switching speeds. The deleterious effects of DC bias circuitry were mitigated by de-limiting them with RF chokes and placing them perpendicular to the polarization of the patch antenna which resulted in reduced electro-magnetic (EM) coupling. This resulted in a fully functional pattern reconfigurable antenna. This work, in Chapter 6, presents a practical implementation of a parasitic layer based patch antenna with successful impedance characterization. The simulated results agree well with measurements demonstrating a robust reconfigurable antenna design.

1.3 Research Flow of Objective 3

Antennas operating at mm-wave frequencies have thus far mainly been implemented using either low temperature co-fired ceramic (LTCC) [24–26] or polymer substrates [27]. Although LTCC can create mechanically robust and hermetically sealed packages with high yield, it might create unwanted surface waves due to the high dielectric constant of substrate. Recently, planar antennas have also been realized on benzocyclobutene (BCB) polymers at mm waves (see Figure 1.6 [27]). BCB ($\epsilon_r = 2.65$, $\tan \delta = 0.0008$), due to its electrical properties, is an excellent choice for improved antenna performance. However, BCB does not enable easy deposition as it requires multiple spins to achieve the desired thickness of a dielectric that could provide a reasonable operational bandwidth (BW) to a planar antenna within the IEEE 802.11ad band (57 - 66 GHz). Also, the very short shelf life time of BCB under room temperature is another disadvantage. In order to create thick enough substrates, SU-8 ($\epsilon_r = 3.1$, $\tan \delta = 0.021$) [28] is an excellent choice. However, its high loss tangent is the drawback for using it as a dielectric for planar antennas. Techniques such as creating holes, air cavities, etc., to reduce the effect of dielectric loss on the antenna performance exist in the literature [29, 30]. Combining the advantages of SU-8 along with these techniques yields an antenna substrate which is both electrically and mechanically an efficient solution. Hence, in this paper, micro-fabricated SU-8 based 3-D structures with air cavities are used as low-loss alternative substrates for WiGig antennas.

Before designing a broadband beam steering antenna at 60 GHz, the design, fabrication,

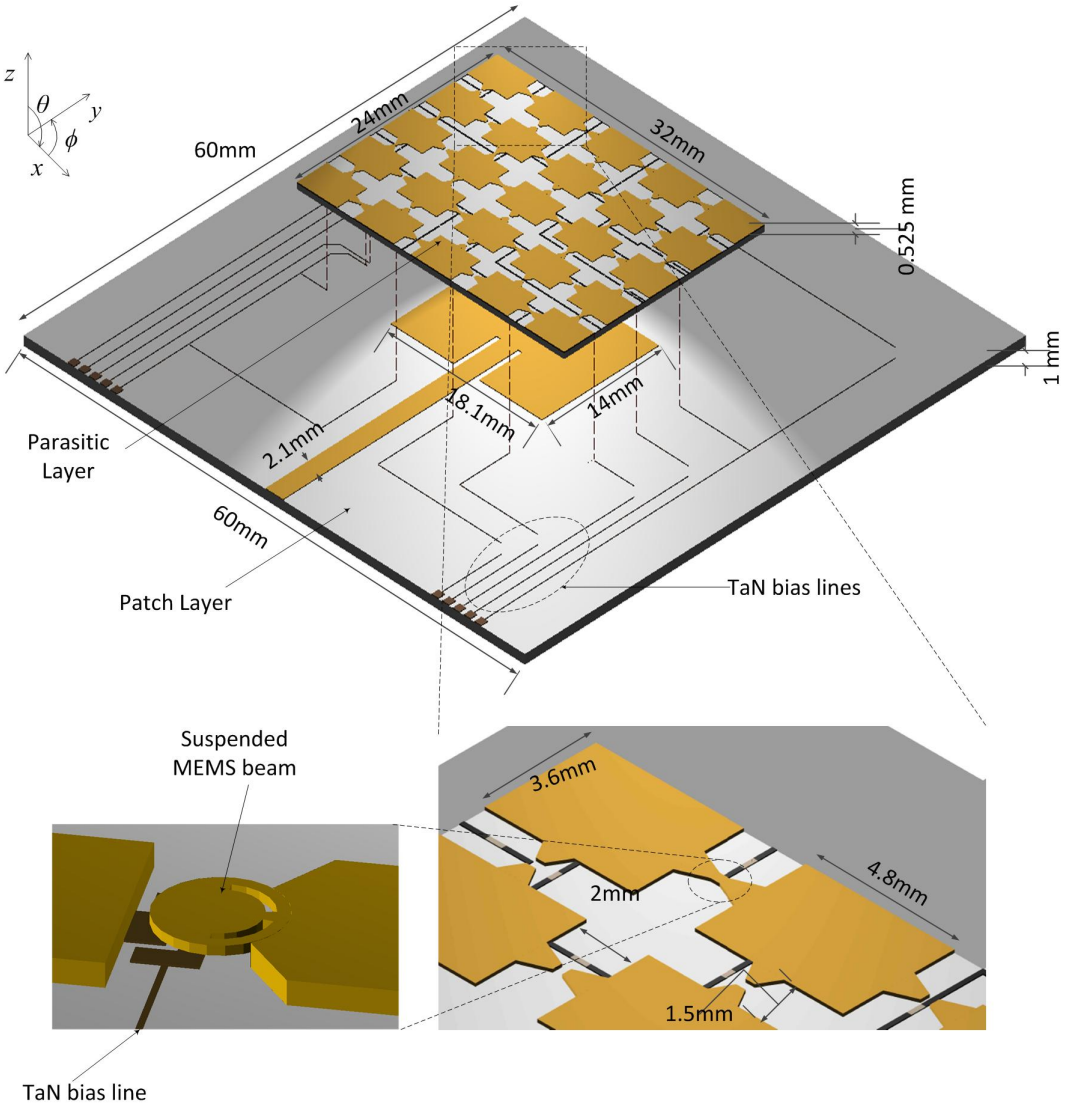

Fig. 1.5: 3-D schematic of the MRA parasitic with 5 x 5 pixel metallization and interconnecting MEMS switch (For the sake of illustration, the parasitic layer is suspended on top of the patch).

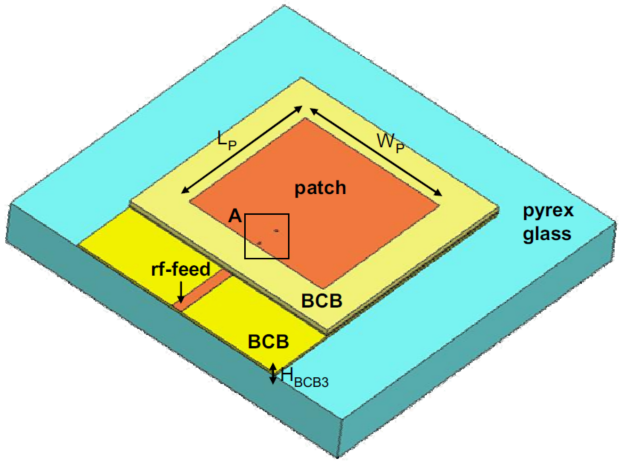

(a) Proposed antenna on a glass substrate.

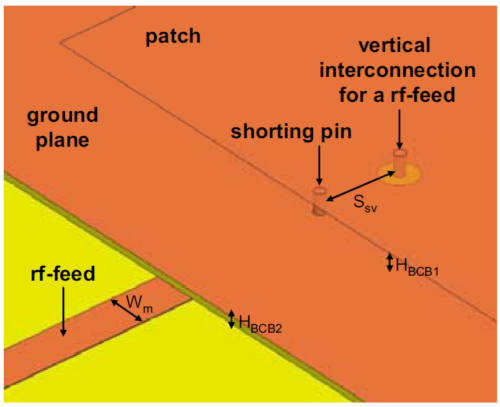

(b) Enlarged view of A in Figure 1.6(a).

Fig. 1.6: Geometry of the proposed BCB antenna.

and characterization of a micro-fabrication compatible broadband patch antenna capable of covering the entire US WiGig band (57 - 66 GHz) should be completed which is given in Chapter 7. Taking this as a building block, the parasitic layer based MRA with perfect open/short switches is presented in Chapter 8. It should be noted that the gain requirement of WiGig communication is high and it depends on the transmitter to receiver distance and the modulation scheme used. For example, for a 5 meter distance between transmitter and receiver, the sum of transmitter and receiver antenna gains should be 19 dB for 16-Quadrature Amplitude Modulation (QAM) supporting 4Gbps data speed. Also, as the dimensions are quite small at such high frequencies ($\sim$60 GHz), without occupying much space, the advantages of a linear array and an MRA can be combined in a novel fashion [31]. This leads to the design of a 2 x 1 MRAA in Chapter 8 which is quite useful in providing robust WiGig communication.

Chapter 2

Compact and Broadband Antenna for LTE and Public Safety Applications

2.1 Introduction

The demand for the radio frequency spectrum, which is a naturally limited resource, is mainly being driven by the next-generation wireless communication services offering multimedia applications on mobile broadband networks. The Long Term Evolution (LTE) [32] standard is promising in this context with its ability to interconnect with other access technologies providing interoperable mobile wireless communication with spectral efficiency. This type of robust communication is also critical when dealing with human-made and natural catastrophes to accommodate a large number of emergency responders [public safety (PS) personnel: police, firefighters, and emergency medical services] operating over different bands. Correspondingly, the emergency responders are increasingly being equipped with wireless laptops, handheld computers, and mobile video cameras to prevent or respond to incidents, thereby extending the eyes and ears of PS agencies. This ensures that the emergency responders have sufficient capacity and means for communications on the field and to/from the infrastructure. Moreover, the demand for various wideband wireless services like e-mail, web browsing, database access, and video streaming in addition to basic modes of wireless communication (like voice and messaging) is desired to effectively combat emergency situations. An antenna for a wireless communication scenario that can accommodate both LTE and US PS bands in emergency situations while maintaining its compact size and radiation integrity is a challenging design task. The legacy planar inverted-F antenna (PIFA) [33] suits the purpose well with its compact size, but has an inherent disadvantage of bandwidth (BW) being 10%. Various BW enhancement techniques for the PIFA have

been employed in the literature such as patch tapering [34], T-shape ground plane [15], and a combination of the aforementioned techniques with a capacitive feeding [16]. In this work, the T-shape ground plane in Khoshniat et al. [16] is modified to a stepped T-shape architecture to create a dual-resonance behavior due to the excitation of two monopole-like structures, which almost doubles the BW with a compact antenna structure. These two resonances are combined in a very simple manner without the use of any active circuitry [35, 36]. The antenna designed in this work is aimed to cover both US PS and LTE bands [32] covering 426 - 861 MHz. Although the architecture of the presented antenna suggests a Planar Inverted F Antenna (PIFA) structure, the working mechanism approaches a printed monopole. Similar to the performance of the presented antenna, printed monopole designs for broad-BW operations above 2 GHz have also been reported [37, 38].

2.2 Antenna Structure and Design Approach

The proposed antenna with a stepped T-shape architecture is depicted in Figure 2.1, which shows the main components of the structure: top patch with capacitive feed, stepped T-shape structure, and shorting wall. The capacitance of the capacitive feed is in the form of metal - insulator - metal, which is formed by the top patch metallization, dielectric of RO 4003C substrate, and bottom capacitor metallization (capacitor patch) as shown in Figure 2.1(a). The antenna is fed by a coaxial cable, whose inner and outer conductors are soldered to the capacitor patch and the stepped T-shape structure, respectively. The shorting wall is soldered to the top patch on one end and to the stepped T-shape structure on the other. The photograph of the prototype antenna is also shown in Figure 2.1(b). This structure of the coaxial-fed antenna with tapered patch results in the initial dual-resonance behavior as shown in Figure 2.2. Having dual-resonance behavior is the advantage of the stepped T-shape architecture over straight T-shape [16]. This is due to fact that the stepped T-shape structure acts as a $\lambda/4$ monopole at two frequencies, which are $f_{c1} = 390$ MHz and $f_{c2} = 585$ MHz for this initial design. The stepped T-shape architecture transforms to a straight T-shape [16] when W_1 and W_3, shown in Figure 2.1, are made equal to L_g. As shown in Figure 2.2, the corresponding reflection coefficient loses its dual-band behavior.

The initial stepped T-shape structure is then jointly optimized with the parameters of patch tapering method and capacitively coupled feed [39] to combine the resonances to obtain 68% impedance and radiation BW as will be shown in the following sections.

2.2.1 Stepped T-Shape Structure

The surface current plots on the stepped T-shape structure and the top patch of the antenna are shown in Figure 2.3(a) and Figure 2.3(b). From the surface current plot in

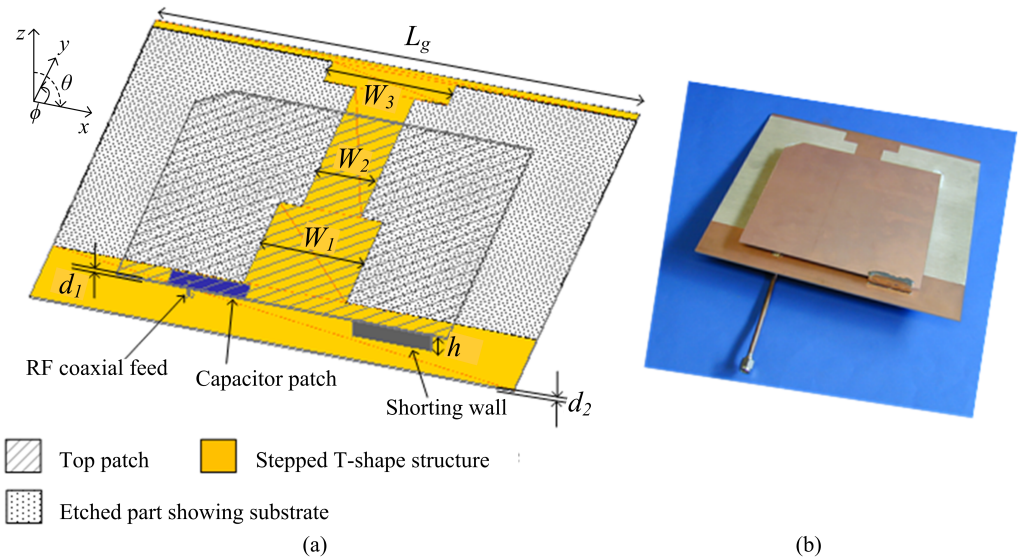

Fig. 2.1: (a) 3-D schematic, and (b) Photograph of the antenna with stepped T-shape structure ($d_1 = 0.813\ mm$, $d_2 = 1.525\ mm$, $h = 7\ mm$).

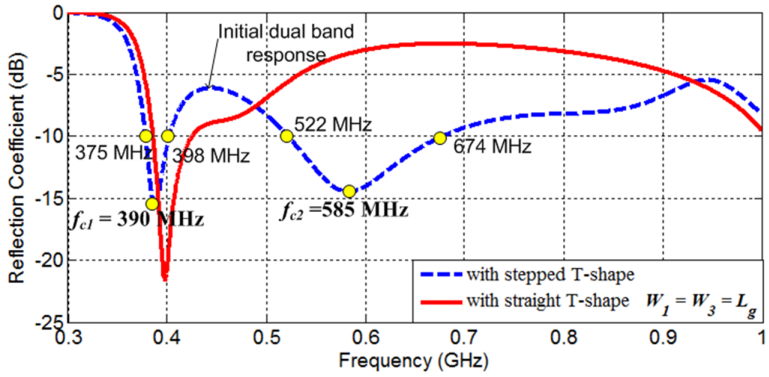

Fig. 2.2: Comparison of reflection coefficients of antenna designs having stepped T-shape and straight T-shape geometries.

Figure 2.3(a), it is evident that the stepped T-shape structure acts as a $\lambda/4$ monopole at $f_{c2} = 585$ MHz with the top patch functioning as a ground plane. The quarter-wavelength (L_1) at $f_{c2} = 585$ MHz is responsible for the impedance match from 522 to 674 MHz as shown in Figure 2.2. Similar behavior is seen in Figure 2.3(b) where the surface current plot indicates a monopole behavior with L_2 being a quarter-wavelength at $f_{c1} = 390$ MHz, which provides an impedance match from 375 to 398 MHz as shown in Figure 2.2. The parameters W_1 and W_2 shown in Figure 2.3 help broaden the BW obtained in each band. The parameters l_3 and W_3 are useful in improving the impedance match in a fine-tuned manner. $L_{s=1to2}$ and $l_{s=1to3}$ are mathematically related as

$$L_1 = g + W_1/2 + l_1 + l_2/3, \tag{2.1}$$

$$L_2 \sim g + W_1/2 + l_1 + l_2 + l_3 + L_g/2, \tag{2.2}$$

where g is measured as the distance in the x-direction from the coaxial feeding point location (indicated by a dashed line) to the edge of the pole structure as shown in Figure 2.3.

2.2.2 Parametric Control of Individual Resonances

To further investigate the working mechanism of the proposed antenna, the impact of the parameters L_1 and L_2 on the reflection coefficient and current distribution was studied. As shown in Figure 2.4(a), varying L_1 ($L_{11} = 118$ mm, $L_{12} = 128$ mm, and $L_{13} = 138$ mm) while keeping L_2(193 mm) fixed changes the higher resonant frequency f_{c2}($f_{c21} = 548$ MHz, $f_{c22} = 585$ MHz, and $f_{c23} = 635$ MHz) with negligible change in the lower resonance at $f_{c1} \sim 390$ MHz. The variable lengths of L_{11}, L_{12}, and L_{13} correspond to $\lambda/4$ monopole lengths at the resonant frequencies of f_{c21}, f_{c22}, and f_{c23}, respectively, where we also observed the similar monopole-type current distributions at each frequency as shown in Figure 2.3. The same analysis was also performed, when L_2 was varied ($L_{21} = 193$ mm, $L_{22} = 210$ mm, and $L_{23} = 227$ mm) while L_1 was kept (128 mm) fixed. The corresponding reflection coefficients are shown in Figure 2.4(b). As can be seen, L_2 parameter controls

the lower resonant frequency f_{c1} with negligible impact on the shift in higher resonance at f_{c2}. However, increasing L_2 parameter results in the loss of input matching of the antenna at f_{c2}. Now, the variable lengths of L_{21}, L_{22}, and L_{23} correspond to $\lambda/4$ monopole lengths at the resonant frequencies f_{c11}, f_{c12}, and f_{c13}, respectively. These parametric analyses reconfirm that the stepped T-shape structure acts as monopole at two frequencies.

2.2.3 Patch Tapering and Capacitive Feed

Introducing a linear taper to the top patch, as shown in Figure 2.1, is a well-known

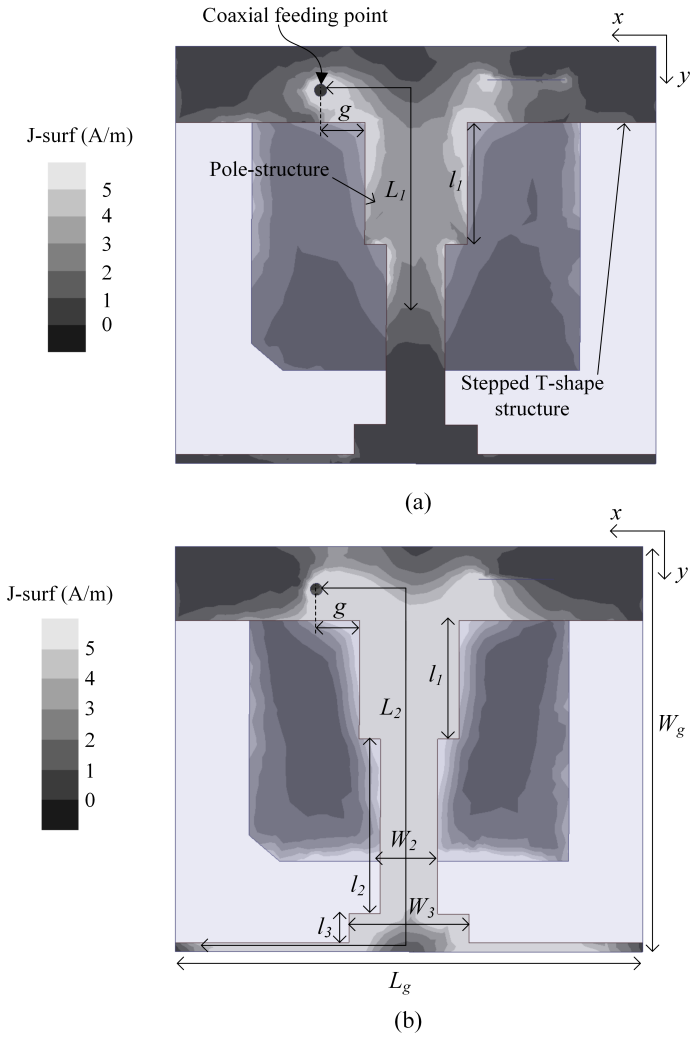

Fig. 2.3: Simulated surface current plot of stepped T-shape structure and top patch at (a) $f_{c2} = 585$ MHz, and (b) $f_{c1} = 390$ MHz.

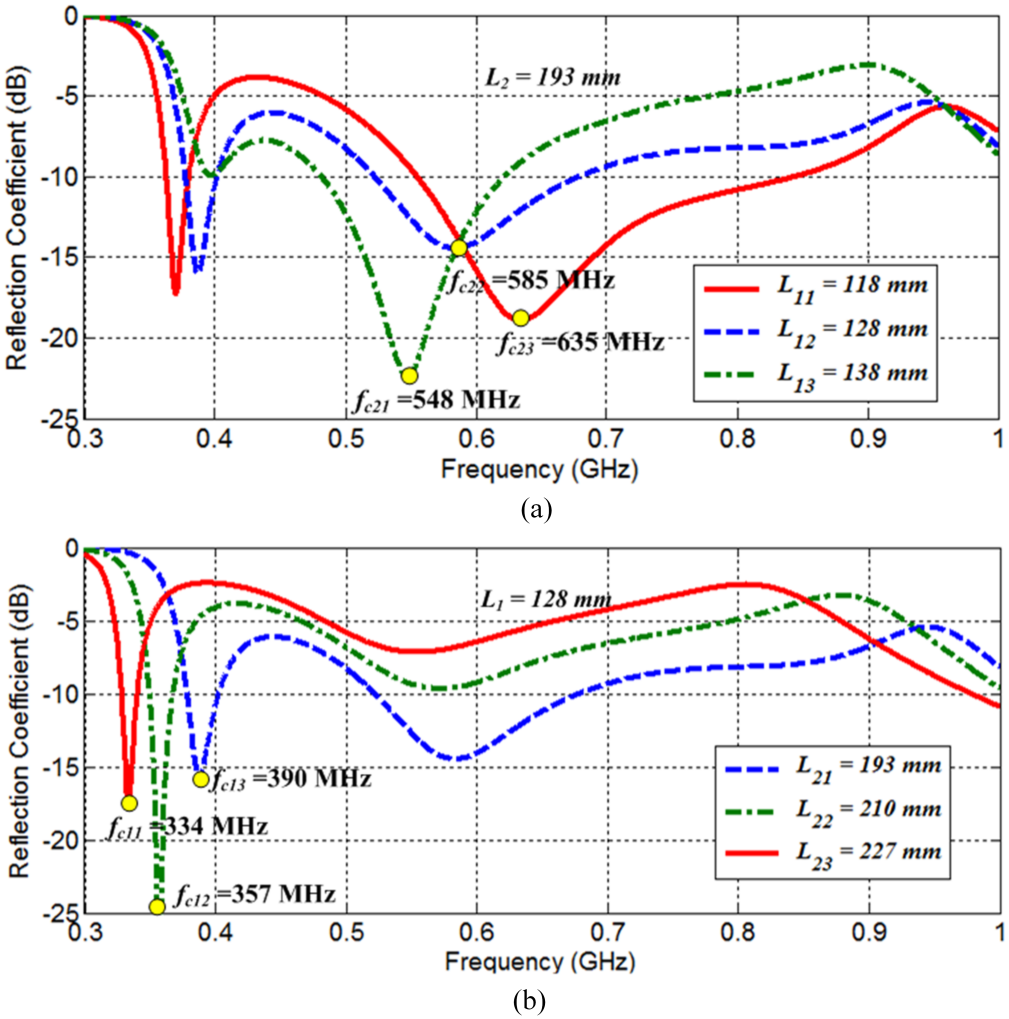

Fig. 2.4: Impact of change in the parameters: (a)L_1 (b)L_2.

BW enhancement technique [34]. The parameters associated with this technique are A, B, L_p, and W_p as shown in Figure 2.5. To accommodate the capacitive feed, (shown in Figures 2.1 and 2.5) in the design, which compensates for the inductance effect of the coaxial feed, a RO4003C substrate ($d_1 \sim 0.8$ mm) is sandwiched by the bottom conductive plate of the capacitive feed (capacitor patch) and top patch metal of the antenna. The essential design parameters are L_c, W_c, which correspond to the size of the capacitor patch, and d_c, which corresponds to the optimum location of the capacitor patch, as shown in Figure 2.5.

2.3 Final Design

Initially, a dual-band response is obtained from the antenna fed by a coaxial cable without capacitive feed mechanism, as shown in Figure 2.2. A capacitive feed is introduced into the design and is jointly optimized with the parameters of the stepped T-shape structure and the tapered top patch to merge the two separately excited bands. In this process, shorting wall width W_s and height h of the structure are also optimized. The design param-

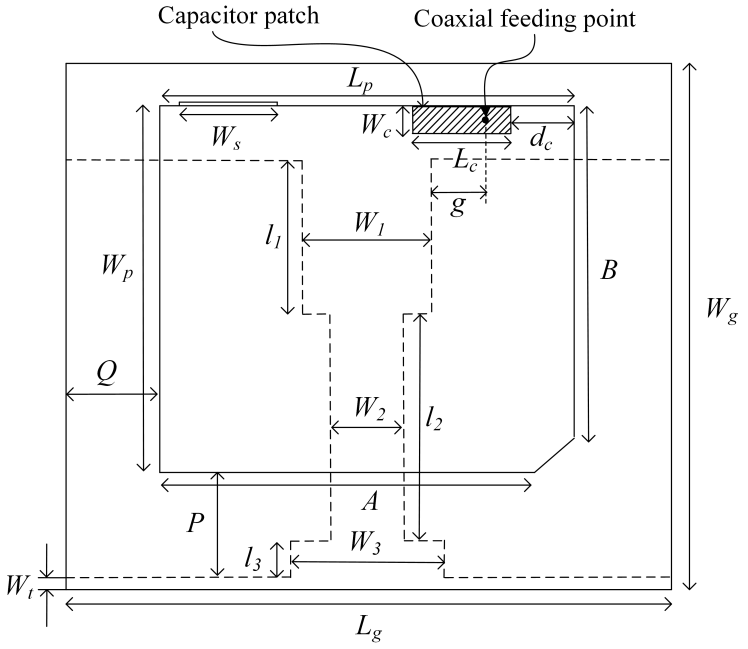

Fig. 2.5: 2-D schematic of the antenna with stepped T-shape structure showing design parameters.

eters of the antenna are shown in Figures 2.1 and 2.5 with the following final dimensions in millimeters: The top patch $L_p \times W_p$ is 132.5 × 117.5; the location of the top patch Q = 30.6, P = 33.9; substrate thickness of top patch d_1 = 0.813; the tapering lengths A = 119.9, B = 106.8 ; the stepped T-shape structure parameters W_1 = 41.25; W_2 = 23.75; W_3 = 49.7; l_1 = 49.3; l_2 = 72.8; l_3 = 12; W_t = 3.75; g = 17; the capacitor patch $L_c \times W_c$ is 31.25 × 8.75, d_c = 20; the width of the shorting wall is W_s = 31.25; the substrate size of the stepped T-shape structure is $L_g \times W_g$ = 193.75 × 168.75; the substrate thickness of the stepped T-shape structure is d_2 = 1.525; the height of the antenna h = 7. As shown in Figure 2.6, this final design significantly improved the initial impedance match (Figure 2.2).

2.4 Fabrication and Measurements

The fabrication of the antenna, with the above dimensions, involves copper-layer removal of RO4003C Rogers substrates by mechanical etching to define the planar geometrical features of different parts of the antenna, which are the top patch including the capacitive feed, vertical wall, and stepped T-shaped structure. The top patch along with capacitive feed are formed by using a substrate with a thickness of d_1 = 0.813 mm, while the stepped T-shape structure and vertical wall are formed by using separate substrates with a thickness of d_2 = 1.525 mm. Finally, these individual parts of the antenna along with the coaxial

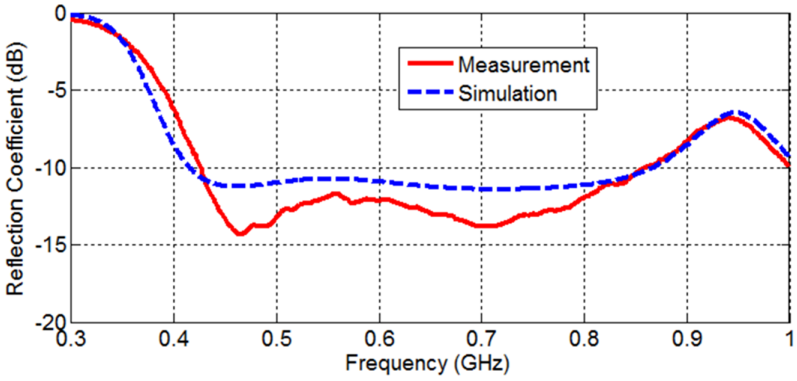

Fig. 2.6: Measured and simulated reflection coefficients of the antenna with stepped T-shape structure.

feed are soldered together to obtain the 3-D architecture of the antenna as shown in Figure 2.1. Although the antenna architecture is not as simple as a single-layer printed antenna, it provides improved performances as will be shown.

The measured reflection coefficient of the fabricated antenna is well in agreement with the simulation results in HFSS [40], which resulted in a wideband performance of 68% covering the frequency range of 426 - 861 MHz for as shown in Figure 2.6.

The radiation patterns showing the normalized total electric field intensity in two planes: xz and yz at frequencies 450, 550, 650, 750, and 850 MHz are given in Figures 2.7 and 2.8. The radiation patterns are consistent with the current distributions presented in Figure 2.3. Since the surface currents have y-orientation and are condensed in the central section of the stepped T-shape structure, the radiation patterns are omnidirectional, being uniform over the xz-plane and directional over the yz-plane. As seen from Figure 2.7, the measured and simulated radiation patterns (in HFSS) agree well, showing that the antenna maintains the integrity of the patterns over the broad frequency band from 426 to 861 MHz.

Figure 2.9 shows the measured efficiencies, which confirm that the presented antenna does not only maintain the integrity of radiation pattern, but also it is highly efficient (90%) over the 426861-MHz bandwidth. The efficiency measurements were performed by using the well-known Wheeler-Cap method. The circle-fitting method described in Miskovsky et al. [41] has been used to postprocess the efficiency data. Combining the directivity and efficiency, the measured gain at each frequency is calculated. As shown in Figure 2.9, the measured and simulated gain values (in HFSS) agree well with good gain flatness observed over the entire frequency BW. The average gain is $\sim$ 2 dBi. This proves that the flat reflection coefficient characteristic has resulted in flat gain and consistent radiation patterns, which would be desirable for an antenna in PS where performance reliability is important.

2.5 Conclusion

A compact and broadband antenna that employs stepped T-shape structure along with patch tapering and capacitive feeding mechanisms results in 68% bandwidth both in

terms of impedance and radiation properties. This antenna combines the responses of two monopoles with minimum impedance variation and without the use of any active circuitry. The integrity of the radiation pattern is maintained over the broad frequency range 426 - 861 MHz with approximately 90% efficiencies and good gain flatness covering the required US PS and LTE bands.

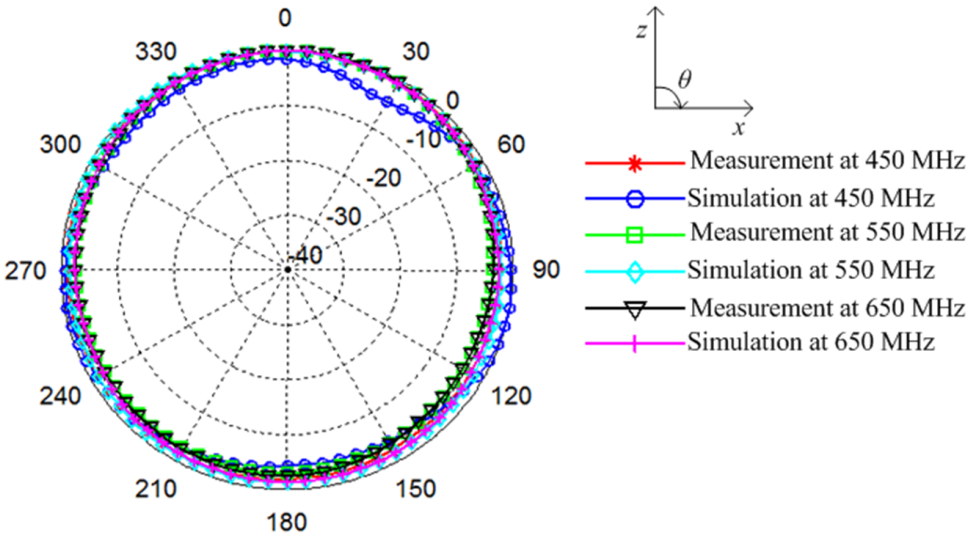

(a) xz - plane at 450, 550, and 650 MHz.

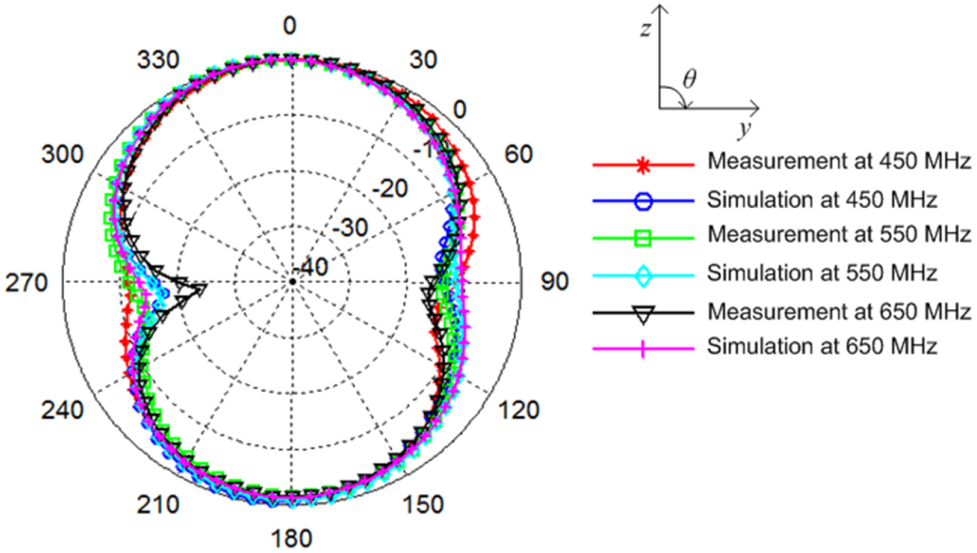

(b) yz - plane at 450, 550, and 650 MHz.

Fig. 2.7: Total normalized electric field intensities.

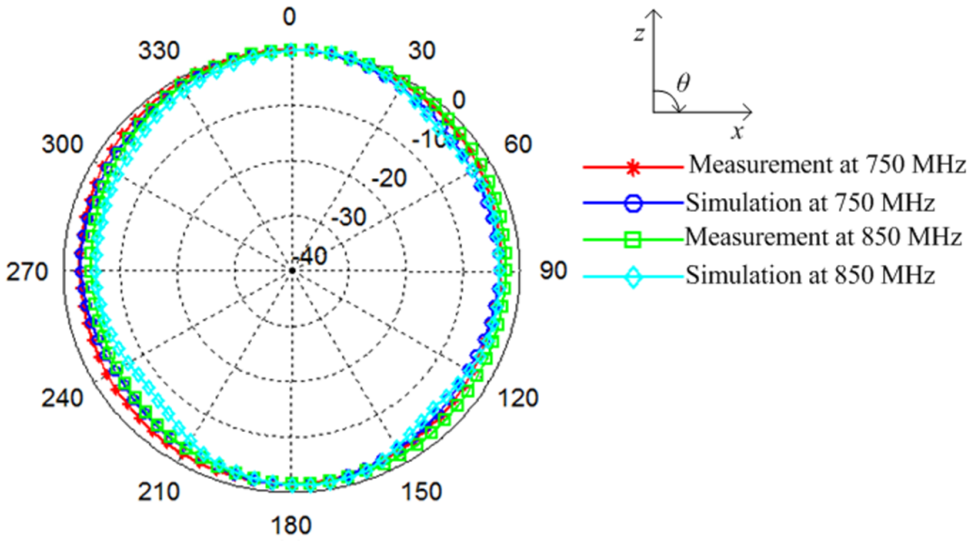

(a) xz - plane at 750, and 850 MHz.

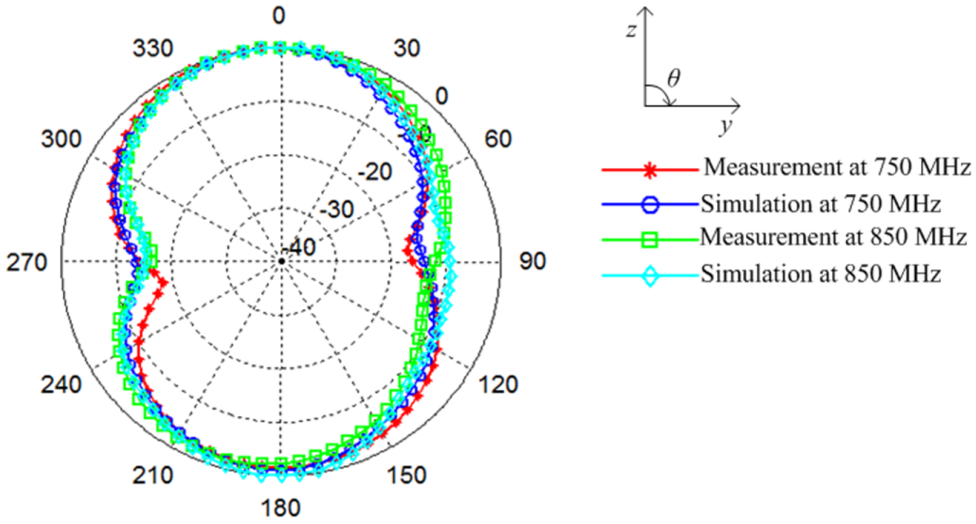

(b) yz - plane at 750, and 850 MHz.

Fig. 2.8: Total normalized electric field intensities.

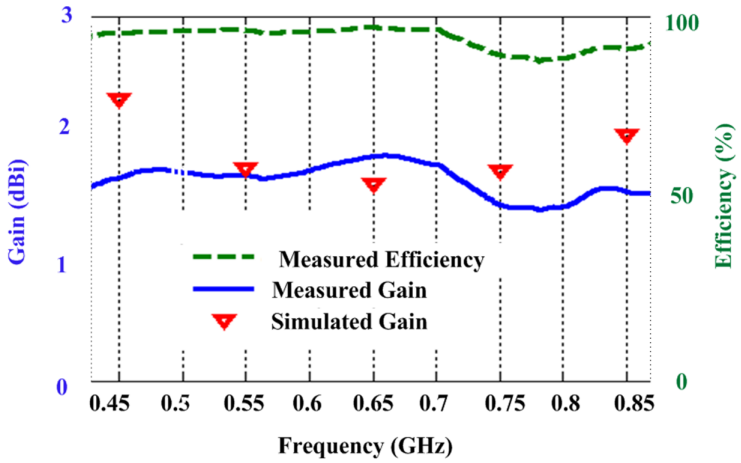

Fig. 2.9: Simulated and measured gains (dBi) along with the measured efficiency of the antenna with respect to frequency.

Chapter 3

Reconfigurable, Tri-Band RF MEMS PIFA Antenna

3.1 Introduction

Multi-input multi-output systems (MIMOs) have been demonstrated by many recent research results which target to make the best use of limited and costly wireless bandwidth by exploiting the high spectral efficiencies offered by multiple antenna systems. Public Safety is one of the application areas of MIMOs where a large number of mobile users need to communicate with each other instantaneously using a number of frequency bands. These bands (152-162 MHz, 400-500 MHz, and 700-900 MHz) are well-separated from each other while broadband operation is required in some of the bands. So, a compact antenna, which covers these bands with broadband operation can increase the functionality, provide interoperability, and reduce the complexity of the whole communication system.

Planar inverted F-antennas, shortly PIFAs [33], are used for meeting these requirements. As the impedance BW of legacy PIFA is low, bandwidth enhancement techniques are employed, such as using a T-shaped ground layer [15], tapering of the patch [34], or a combination of techniques [16]. These tecniques aim to maximize BW while minimizing the use of reconfiguration techniques. Many RF MEMS-based reconfigurable antennas, on the other hand, have been presented that utilize the advantages brought by the MEMS technology [42–45]. However, no effort has been presented up to date that targets obtaining all of the aforementioned bands with such a high band-switching ratio.

This chapter presents a reconfigurable, tri-band PIFA antenna that operates around the center frequencies 160, 450, and 800 MHz Public Safety bands. The reconfigurability is achieved via ohmic contact RF MEMS switches, which are used for alternating the RF current flow paths physically, and hence, the antenna is operated in desired reconfigurable mode of radiation. Bandwidth enhancement techniques, such as patch tapering and the T-

shaped ground layer, are also employed in order to increase the instantaneous bandwidths in each band.

3.2 Design

The proposed antenna is a PIFA which is depicted in Figure 3.1. The antenna has mainly two layers, which are the top patch and the ground layer. RO4003C ($\epsilon_r = 3.38$, $\tan \delta = 0.002$) is used as substrate for both layers. In addition, the gap between these two layers is also filled with stacked laminates of this material in order to obtain size reduction. The substrate that is placed just on top of the ground layer has a large gap in the middle. This layer is called the packaging layer and used as a 2-level packaging for the RF MEMS switches. Two bandwidth enhancement techniques, namely T-shaped ground-layer and patch tapering, are employed and optimized. The simulations of the antenna are done using HFSS v12 [46].

3.2.1 Operation Modes

The antenna has three operation modes and switching between these modes is achieved by means of RF MEMS switches. All of the MEMS switches are placed strategically on the ground layer, which is the major radiating element of the antenna. The top view of the ground layer is presented in Figure 3.2(a), where the positions of the MEMS switches are also given.

The idea of changing the resonance frequency of the presented antenna stems from changing the shape of its pole on the T-shaped ground layer. The dimensions of the pole are very effective on the resonance frequency and bandwidth of the antenna. So, for the first mode of operation, mode 1, a meandered line is inserted on the pole and the antenna is optimized to resonate at 160 MHz. A submeander is also added to the meandered line so that there will be two closely separated resonances around 160 MHz. In this mode, Group 1 and 3 switches are always on, and Group 4 switches are on or off depending on the required resonance frequency as illustrated in Figure 3.2. For mode 2, the meandered line is switched off, and the RF current is forced to follow the straight path. In this mode, the

antenna is optimized to have a resonance around 450 MHz. In order to attain the required impedance bandwidth, the width of the pole structure is adjusted. In this mode, Group 2 and 3 switches are on. As the width of the pole structure is strongly effective on the impedance bandwidth, the antenna is optimized to operate in mode 3, which is centered on 800 MHz, by decreasing the width of the pole structure. However, the design is challenging as the other two modes needs to be kept undisturbed while designing the third mode. In this mode, only Group 2 switches are on. Figure 3.2(b) shows the active parts of the ground plane in each mode where Table 3.1 gives final design dimensions of the antenna.

3.2.2 RF MEMS Switches and Bias Lines

Ohmic contact, series RF MEMS switches are used for the antenna which are designed and fabricated by the authors. The fabrication process is a five-layer surface micromachining process. The measured switch performance shows that it has isolation better than -33 dB

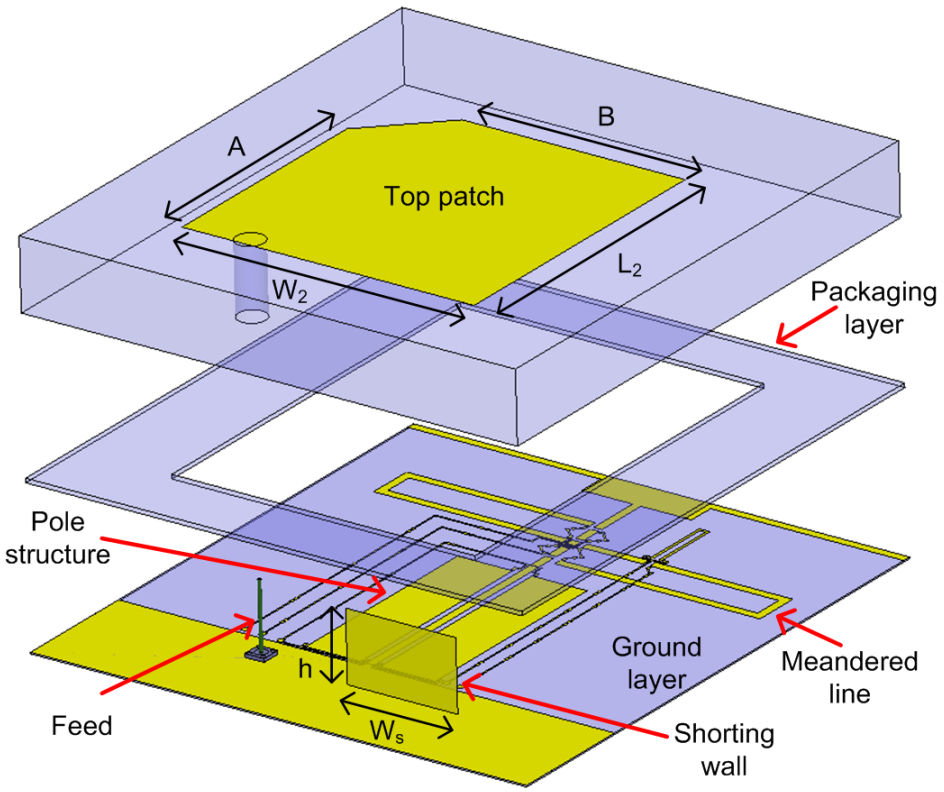

Fig. 3.1: The 3-D view of the proposed reconfigurable PIFA.

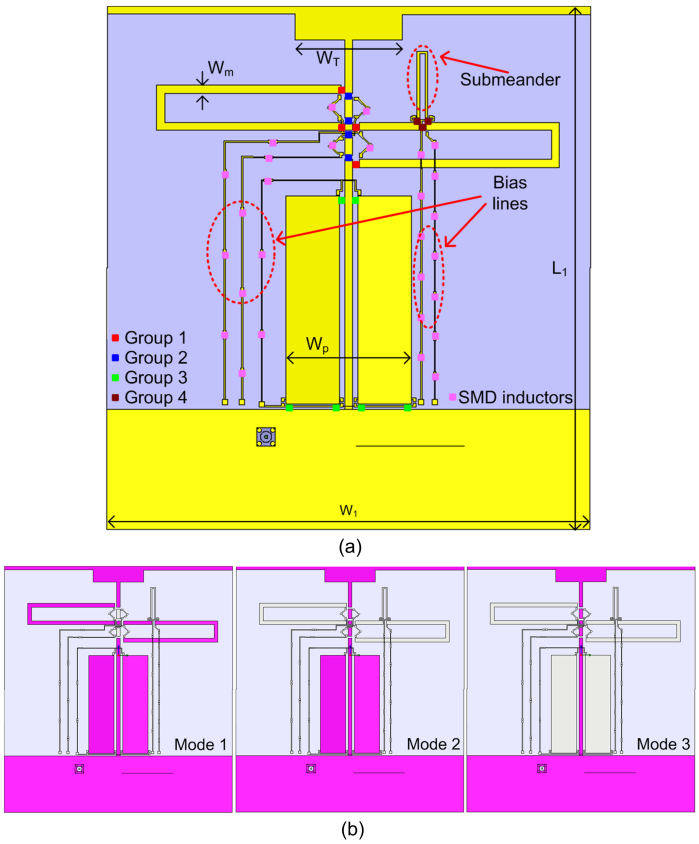

Fig. 3.2: (a) The top view of the reconfigurable ground plane, and (b) The active parts of the ground layer in all three modes of operation.

at 2 GHz and -12 dB at 20 GHz. The measured insertion loss is better than 0.25 dB at 20 GHz and the measured DC resistance varies between 1.5 to 20 Ω. The actuation voltage of the switch is measured as 80V. Figure 3.3 shows the photograph and Scanning Electron Microscope (SEM) of the fabricated switch.

Five bias lines are used in the antenna in order to distribute the DC actuation voltages

Table 3.1: The dimensions of the designed antenna, H = 25 mm.

Parameter	*Value*	*Parameter*	*Value*
W_2	108 mm	W_m	3mm
L_2	106 mm	W_T	40mm
A	84 mm	W_p	33mm
B	81 mm	W_1	180mm
W_s	40 mm	L_1	195mm

to the switches. The bias lines are physically comparable to the size of the antenna, and they can be deleterious to the antenna performance if implemented only with metals. So, in order to reduce their effects, the bias lines are delimited by SMD inductors. CoilCraft SMD inductors with 270 nH inductance are used in the presented antenna. SMD resistors with 500 kΩ resistance are also employed in addition to the on-chip resistors on the MEMS switches for biasing purposes. Although the SMD inductors and resistors do not completely eliminate the effects of the bias lines, they help significantly with the paid price of a slight increase in the loss of the antenna.

3.3 Measurement Results

Figure 3.4 shows the photographs of the fabricated ground plane and final form of the antenna. The fabricated antenna is measured in 100 to 1000 MHz band using Agilent E5061A network analyzer with one-port open-short-load calibration. The measured and simulated return losses are given in Figures 3.5 and 3.6. During the measurements of the antenna, RadantMEMS RMSW100 switches [47] are also used in order to have a reference performance of the antenna.

All of the measurement results show good agreement with the simulations. The measured instantaneous -10 dB impedance bandwidths are 7%, 11%, and 19% for the three modes, respectively. Figure 3.5 shows the measurement results for mode 1, where the measured resonance is shifted from 167 MHz to 185 MHz and the bandwidth is widened. This

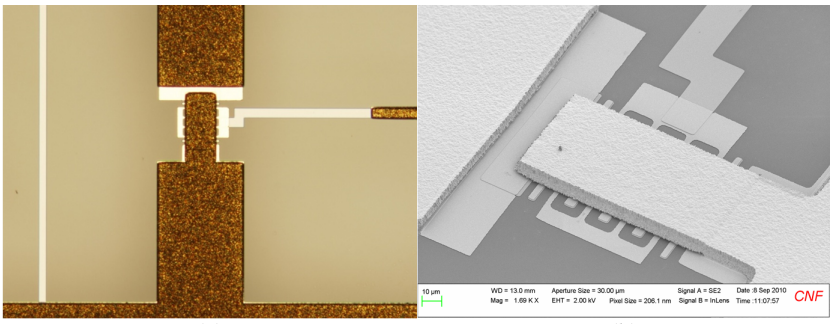

(a) (b)

Fig. 3.3: (a) Photograph, and (b) SEM of the fabricated ohmic contact, series RF MEMS switch.

is because one of the bias lines was omitted in the simulations due to the unaffordable mesh size of the HFSS simulations. The increase in bandwidth in this mode is a result of increasing loss of the antenna, which is caused by high number of SMD resistors on the bias line that could not be included in the simulations. Figure 3.6 shows the return losses of mode 2. Here, the measured impedance bandwidth is 376-to-425 MHz, which is 25 MHz shifted version of the targeted 400-450 MHz. The reason of the shift is again the limitations in the HFSS simulation environment. However, these results are good for the targeted US public safety bands. The measurement result of mode 3, which is presented in Figure 3.7, shows an impedance bandwidth from 760 MHz to 925 MHz. In the simulation of this mode, none of the bias lines were taken into account as they cause a very large mesh size, and the simulation fails to converge. However, the simulations could guess the impedance matching band and the traces roughly follow each other anyway, and the antenna demonstrates the desired bandwidth with a small shift.

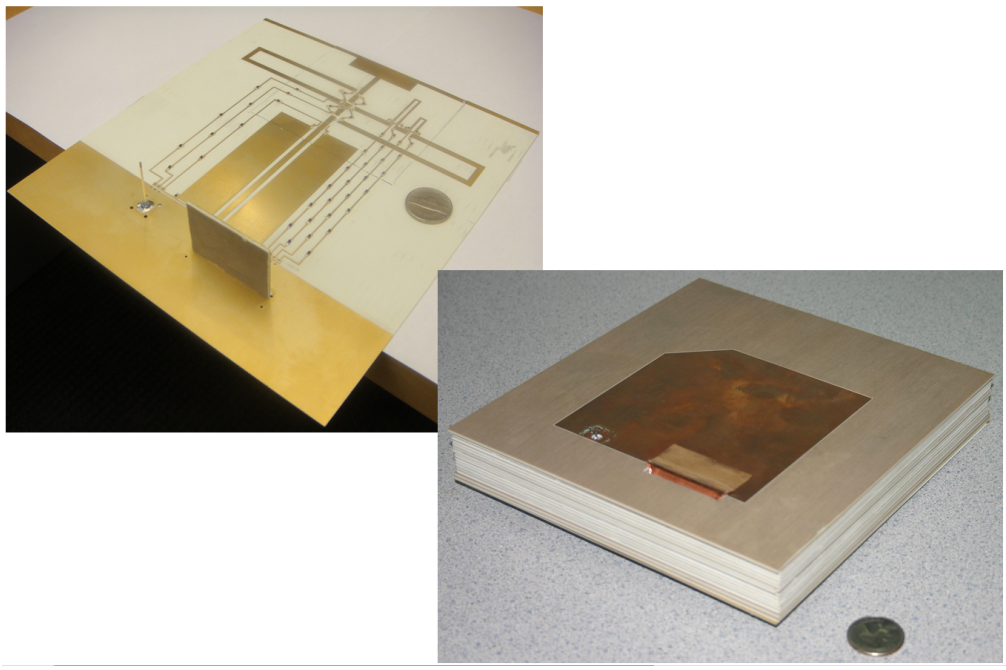

Fig. 3.4: Photographs of the fabricated ground plane and the antenna.

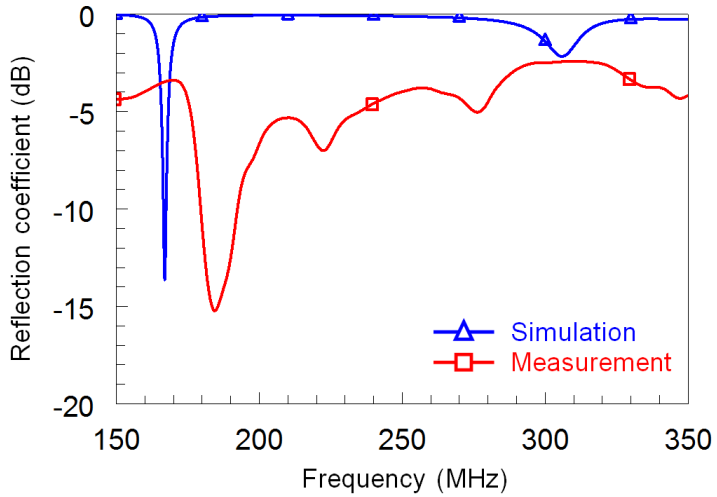

Fig. 3.5: The measurement results of the proposed PIFA compared with the simulations in mode 1.

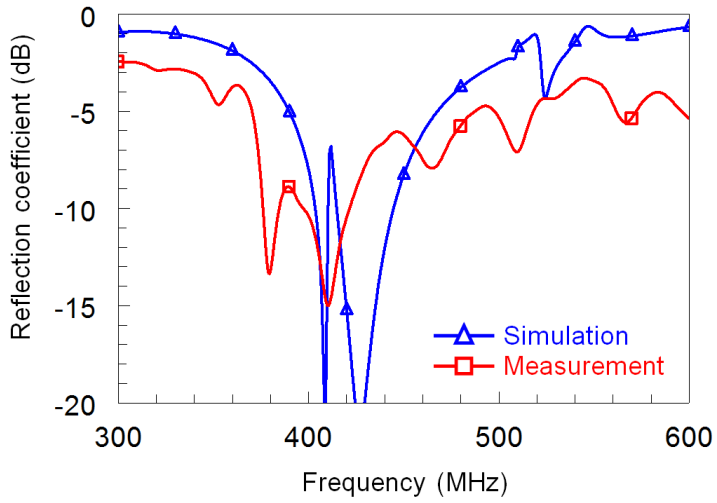

Fig. 3.6: The measurement results of the proposed PIFA compared with the simulations in mode 2.

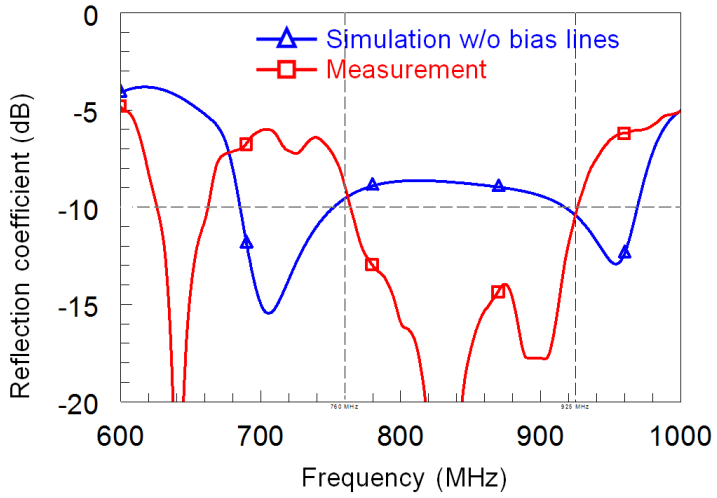

Fig. 3.7: The measurement results of the proposed PIFA compared with the simulations in mode 3.

Chapter 4

Frequency Reconfigurable, 220 - 5000 MHz, Five-Band RF MEMS PIFA

4.1 Introduction

The need for the efficient use of limited and costly bandwidth (BW) in the wireless communication systems has increased significantly over the last decades. The growth of market of the mobile devices that can perform interoperable communication over various frequency bands plays the main role in this situation. Correspondingly, this result in an increasing demand on the Multiple-Input Multiple-Output Systems (MIMO), and one important application area for MIMO is the United States (US) Public Safety (PS) communications. PS communication systems require a large number of mobile users that need to communicate over several frequency bands. These bands (220-222 MHz, 406-512 MHz, 698-894 MHz, 932-941 MHz, and 4940-4990 MHz) are wellseparated from each other. If a separate antenna is used for each of the bands, the system complexity increases drastically. Hence, a reconfigurable, compact antenna, which covers these bands can increase the functionality, provide interoperability, and eventually reduce the complexity of the whole communication system.

Planar inverted F-antennas (PIFAs) [33], commonly used in mobile devices, have limited instantaneous bandwidth. BW enhancement techniques presented in the literature [15, 16, 34] in conjunction to the frequency reconfigurability introduced by MEMS switches can result in an antenna design that can operate in all the aforementioned PS bands resulting in a high operational frequency ratio. Although, many reconfigurable antenna designs are presented in the literature [42–44, 48, 49] a single antenna with a high operational frequency ratio of 22 (4960/220) has not been designed up to date.

In this work, a frequency reconfigurable PIFA that can operate in five US PS bands centered on 221, 470, 620, 935, and 4960 MHz (named as modes 1 - 5, respectively), is presented. The antenna actually functions as two different PIFAs that are fed from a common coaxial feed. The reconfigurability is achieved via ohmic contact Radio Frequency (RF) Micro Electro Mechanical Switches (MEMS), which are used 1) to connect/disconnect the parts of the antenna structure so that the antenna is electrically scaled, and 2) to alternate the RF current flow paths physically on the reconfigurable ground so that the band of resonance is changed. Hence, the whole antenna structure is operated in desired reconfigurable mode of operation, and it provides a very high operational frequency of 22.

4.2 Design

4.2.1 The Antenna Geometry

The antenna structure, shown in Figures 4.1 and 4.2, contains two antennas fed from a common coaxial feed. The first antenna, which is responsible for the operation of modes 1 - 4, is a capacitive fed PIFA with a reconfigurable ground and top patch. The reconfigurable ground has two T-shaped ground metallizations, which are physically connected or disconnected by means of RF MEMS switches. Among the two T-shaped ground metallizations, the one extended by the meandered line is responsible for mode 1 (220 MHz) operation. This is required in order to obtain the necessary electrical length for the lowest frequency of operation. The other T-shape ground is responsible for the operation of modes 2 - 4. Patch tapering, T-shaped ground, and capacitive feeding are employed to obtain wider instantaneous bandwidth in modes 1 - 4.

The second antenna which is a miniaturized version of the first antenna is responsible for mode 5 operation and is included in the first antenna responsible for all other modes of operation. It is a capacitively loaded, directly fed PIFA. The capacitive feed of the first antenna acts as the top patch for this antenna and the capacitive loading element is the isolated rectangular loading plate on the top patch. A separate T-shaped ground (mode 5) is located as a third layer between the top patch (responsible for modes 1 - 4)

and reconfigurable ground layer, and it becomes the major radiating element of the second antenna. The second antenna is connected to/ isolated from the first one using RF MEMS switches on the top patch and ground plane.

A reconfigurable stub is also introduced in the design to improve the return loss in mode 1 without disturbing the other modes of operation. Two MEMS switches integrated on the stub at strategic locations helps to achieve this task.

All four layers of the whole antenna structure are fabricated using RO4003C substrate ($\epsilon_r = 3.38$, $\tan\delta = 0.002$). The substrate thickness is 0.813 mm for all layers. The critical design parameters are given in Table 4.1. The substrate thickness also determines the distance between the capacitive feed and loading plate, which is also an important parameter for mode 5 operation. Air is used as a substrate to increase the radiation efficiency of the antenna.

4.2.2 Modes of Operation

Among the five modes of operation (modes 1 - 5), the first four modes are attained by

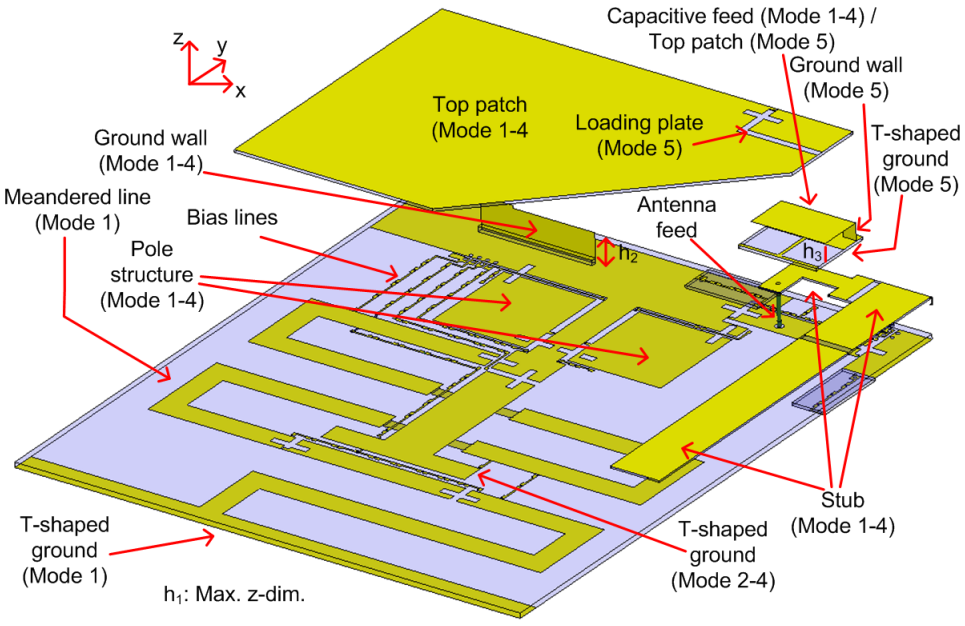

Fig. 4.1: The 3-D view of the proposed reconfigurable PIFA.

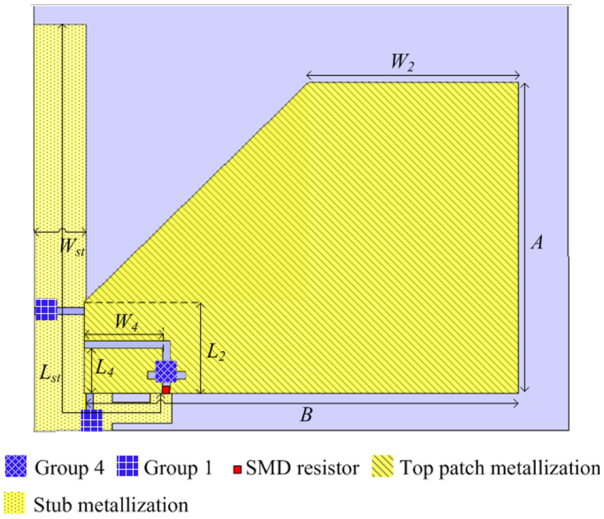

(a) Top patch.

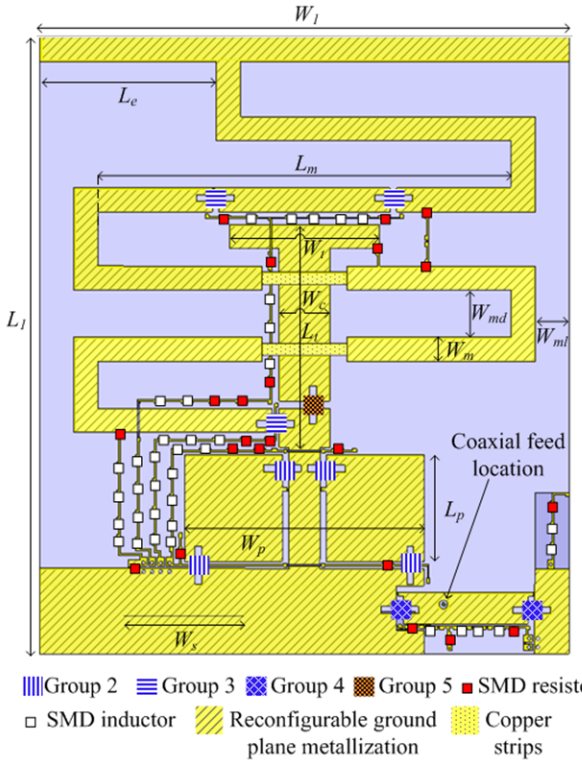

(b) Reconfigurable ground.

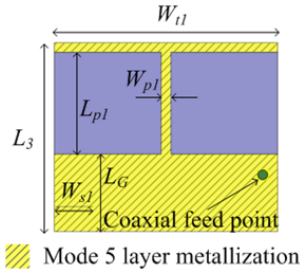

(c) T-shaped ground for mode 5.

Fig. 4.2: The layout of the antenna parts with MEMS and Surface Mount Device (SMD) components.

reconfiguring the ground and stub of the first antenna, whereas the fifth mode is obtained by disconnecting all parts of the first antenna from the second one.

Figure 4.2 shows a detailed description of the RF MEMS switches and other components that are utilized for the reconfiguration of the proposed antenna. Figure 4.3 presents the active parts of the antenna in all five modes, whereas Table 4.2 summarizes the states of the RF MEMS switches in each mode. In mode 1, the longest RF path which includes the meandered line is chosen by the corresponding status of MEMS switches (shown in Table 4.2) to obtain the lowest frequency of operation. Secondly, in the dual band operation of modes 2 and 4 the surface current is made to stay only on the pole-structure (see Figure 4.3) and T-shape ground (responsible for modes 2 - 4) by disconnecting the meandered line. In this mode, the reconfigurable stub plays a role in broadening the bands. On the other hand, in mode 3, the stub is switched off, which pushes the 470 MHz band of mode 2 to higher frequencies (620 MHz).

Finally in mode 5, the small T-shaped ground plane responsible for 4900 MHz operation should alone resonate. This is done by disconnecting the small PIFA from the rest of the antenna using the appropriate switch configuration in Table 4.2. Correspondingly, Figure 4.3 shows that only the parts responsible for mode 5 operation are active. An island is created on the top patch (responsible for modes 1 - 4) to kill the excessive surface current which would shift the resonance in mode 5. This island eventually loads the small PIFA capacitively. It should be noted here that all modes of operation should be jointly optimized in a reconfigurable antenna design.

Table 4.1: The optimized parameters of the proposed antenna design (in mm).

Par.	*Value*	*Par.*	*Value*	*Par.*	*Value*	*Par.*	*Value*	*Par.*	*Value*
W_1	155	B	970	L_G	8.3	L_4	13.2	W_{p1}	1
L_1	179	L_m	121	W_S	35	W_m	7	W_{st}	15
W_2	60.9	L_e	51.8	W_t	44	L_{p1}	11	W_{ml}	10
L_2	26.4	h_1	9.5	L_p	31	L_{st}	143	W_{t1}	23.9
L_3	20.2	h_2	8.6	W_p	70	W_{md}	13.6	A	90
W_4	22.8	h_3	5	W_c	15	W_{S1}	121	W_S	45

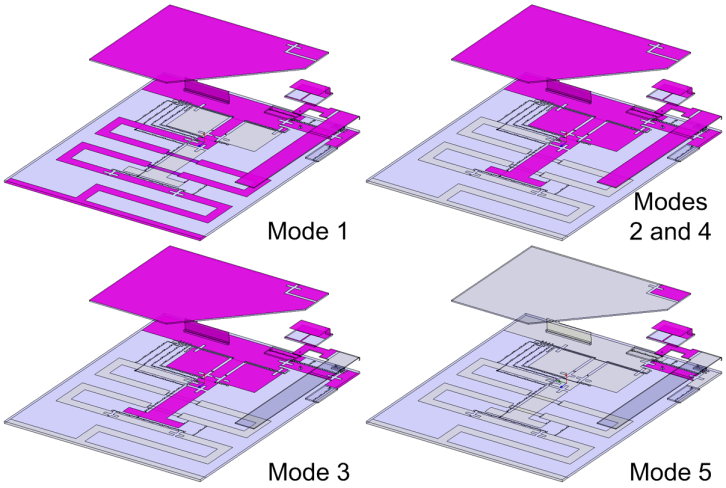

Fig. 4.3: The active parts of the antenna structure in all five modes of operation.

4.3 MEMS Modeling and the Effects of the Bias Lines

The modeling of RF MEMS switches and their DC bias lines have major impact on the performance of the proposed antenna. Ohmic contact, series RF MEMS switches, which have been designed and fabricated, have been used in the antenna design. The fabrication process is a five-layer surface micromachining process. The measured switch performance shows that it has isolation better than -33 dB at 2 GHz and -12 dB at 20 GHz. The measured insertion loss is better than 0.25 dB at 20 GHz and the measured DC resistance varies between 1.5-to-2Ω. The actuation voltage of the switch is measured as 80V. Figure 4.4 shows the photograph and SEM of the fabricated switch.

The effects of the RF MEMS switches are modeled using a simple series capacitor that corresponds to the off-state parasitic capacitance of the switch (=30fF, extracted from

Table 4.2: The states of the RF MEMS switch groups in all modes of operation.

Groups	*mode1*	*mode2*	*mode3*	*mode4*	*mode5*
$M1$	ON	OFF	OFF	OFF	OFF
$M2$	OFF	ON	ON	ON	OFF
$M4$	ON	ON	ON	ON	OFF
$S1$	ON	ON	OFF	ON	OFF
$S2$	ON	ON	OFF	ON	OFF
P	OFF	ON	ON	ON	OFF

previous measurements) in HFSS simulations. More complex models are not chosen as in Yang et al. [44] or Huff and Bernard [48] because the antenna size is already big; moreover, it contains 13 RF MEMS switches and 6 bias lines, which makes it difficult to simulate in HFSS v13 [50].

The bias lines are necessary for carrying the actuation signals to RF MEMS switches. Since the RF MEMS switches are distributed to almost all parts of the antenna, the long bias lines which cover a significant part of the antenna surface affect the antenna performance drastically if not properly delimited by SMD inductors and resistors. The positions of these components (see Figure 4.2) are optimized so that the antenna performance is affected minimally. A total of 6 bias lines have been used for this antenna on which 40 resistors (330KΩ, 500KΩ) and 80 inductors (270 nH and 8 nH) have been soldered.

4.4 Fabrication

The fabrication of the antenna is composed of two main steps, which are: the assembly of different parts into a single 3-D antenna, and the integration of RF MEMS switches onto the antenna.

The antenna body is composed of four layers which are, from top to bottom: the big top patch (modes 1 - 4), small top patch (mode 5)/capacitive feed, small T-shaped ground (mode 5), and reconfigurable T-shaped ground. There are also three additional layers. Two of them are used for extending the DC bias lines to the dipswitches, which are used for distributing the DC signal to the groups of RF MEMS switches. There is also another layer on top of the big top patch (modes 1 - 4) that protects the antenna and increases its robustness. The substrate of the top patch is sandwiched by the top patch metal and the capacitive feed on both sides of it. For all of the layers, 0.813 mm thick RO4003 substrates are used. All the different layers of the antenna are assembled and soldered together to result in a 3-D antenna.

The final step is the integration of the RF MEMS switches with the antenna body. Since antenna has a 3-D structure and the body has to be built first, it is not possible to integrate the switches as wire-bonding is not possible. Hence, small, three terminal

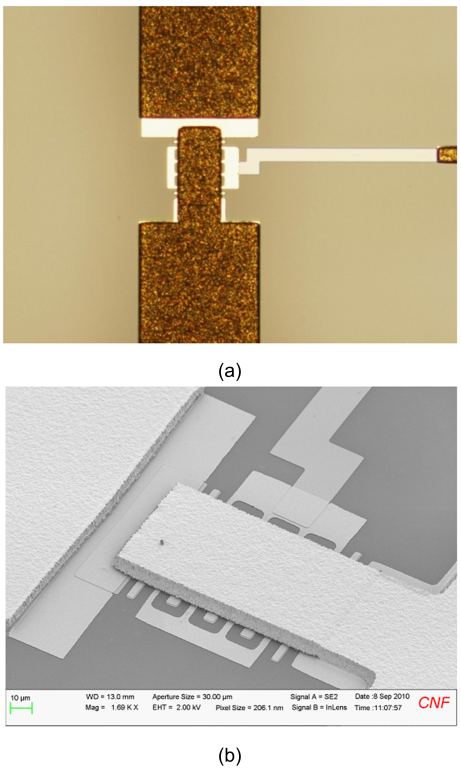

Fig. 4.4: (a) Photograph, and (b) SEM of the fabricated ohmic contact, series RF MEMS switch.

PCB parts are utilized that are made of 0.508 mm thick, Au coated RO4003 substrates. Each switch has been epoxied and wire-bonded to a small PCB, which is then soldered to the antenna body. A total of 13 MEMS switches have been used for the antenna. The photographs of the fabricated antenna are presented in Figure 4.5.

4.5 Results

The reflection coefficient measurements of the fabricated antenna are made using Agilent 8722ES network analyzer with a one-port Short Open Load (SOL) calibration in 100 MHz- 6000 MHz frequency band. In Figure 4.6, the measurement results in comparison to their simulations which shows good agreement have been depicted. As the resonances in modes 1 and 2 were slightly shifted, the antenna is tuned and optimized by adjusting the location of the additional Cu strips (see Figure 4.5) to shift the resonances. Since, the modeling for the final DC cabling to the Keithley 2400 supply is not included in HFSS minor

differences between simulations and measurements are noticed. The measured fractional bandwidths are 10%, 5%, 8%, 7%, and 8% in modes 1-to-5, respectively.

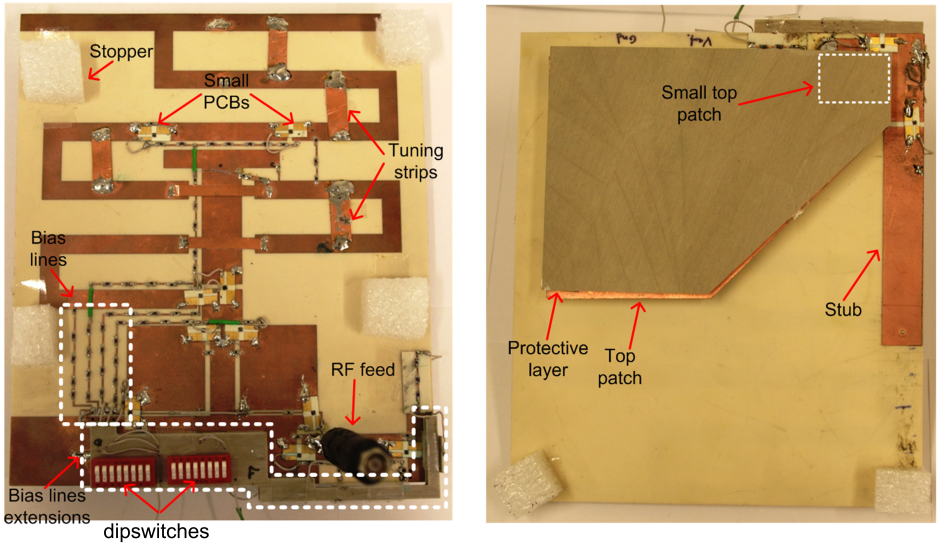

Fig. 4.5: The photographs of the fabricated antenna in (a) bottom view, and (b) top view.

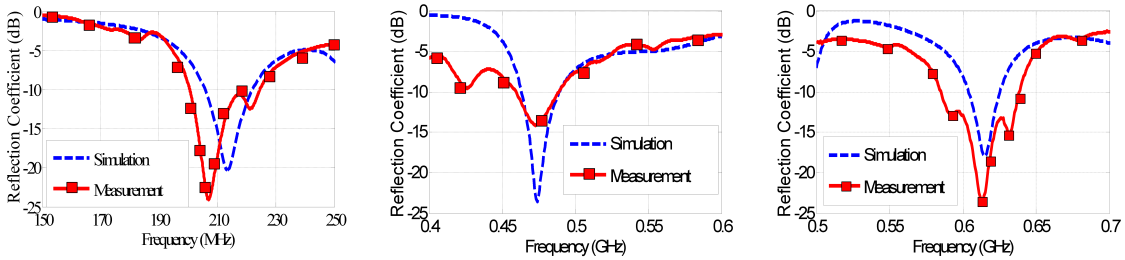

(a) mode 1. (b) mode 2. (c) mode 3.

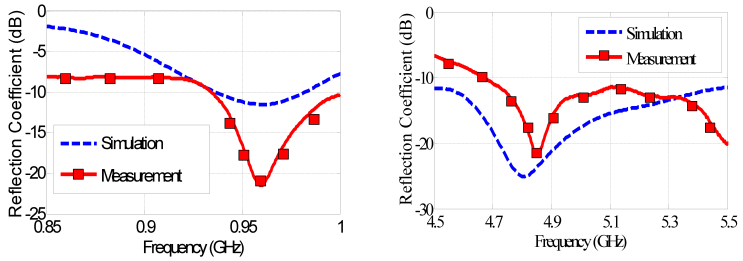

(d) mode 4. (e) mode 5.

Fig. 4.6: The simulated and measured reflection coefficient plots of the fabricated antenna in all five modes of operation.

Chapter 5

RF MEMS Integrated Frequency Reconfigurable Quad Band Antenna

In this chapter, an intelligent combination of techniques in the previous chapters and also in Zhong et al. [21] has lead to a robust and compact antenna design with simple architecture capable of providing radiation pattern integrity at all the PS bands: 220 MHz, 470 MHz, 800 MHz, and 4900 MHz. This antenna is electrically small with lateral dimensions being $\sim 0.13\lambda$ x 0.11λ at the lowest frequency of operation (220 MHz). It uses two Radio Frequency (RF) Micro Electro Mechanical Systems (MEMS) switches to reconfigure between two modes of operation. While operating in mode 1, the antenna is designed to provide triple-band operation covering 220, 470, and 4960 MHz bands. Mode 2 provides the operation at 800 and 4960 MHz bands. The broadening of bandwidth at 800 MHz is achieved by U-shaped slot technique [51]. To excite the highest frequency band (4960 MHz), which is largely separated from the other three bands, a physically small antenna element with similar radiating properties as the former one is integrated into the common coaxial feed in a multi-layered architecture. The measured and simulated fractional bandwidths of $\sim$ 3%, 4%, 21%, and 17% have been obtained at 220, 470, 800, and 4960 MHz bands, respectively. The measured and simulated radiation patterns and efficiencies also agree well demonstrating reasonably well integrity in radiation pattern.

5.1 Antenna Structure and Working Mechanism

5.1.1 3-D Architecture

The 3-D schematic and cross section view of the antenna are depicted in Figures 5.1 and 5.2, respectively. Figure 5.1 shows the main components in a multi-layered fashion:

top patch layer with capacitive feed, reconfigurable layer with two RF MEMS switches, and small antenna element. Magnified pictures of the top patch and reconfigurable layers with the critical design parameters are also provided in Figures 5.3 and 5.4. The substrate material used for all the layers is RO4003C ($\epsilon_r = 3.55$, $\tan\,\delta = 0.0021$) with corresponding thicknesses shown in Figure 5.2. Notice that RO4003C is used for the mechanical integrity of the antenna structure, whereas the electrical substrate is air. The antenna is fed by a capacitively coupled coaxial feed, whose inner and outer conductors are soldered to the capacitive feed and reconfigurable layer metallizations, respectively (see Figure 5.2). The capacitance of the capacitive feed is formed by top patch metallization, RO4003C substrate ($126 \times 134 mm^2$, thickness (t) = 0.813 mm), and capacitive feed metallization in the form of a metal-insulator-metal. The top patch metallization has a U-shaped slot (see Figures 5.1 and 5.3), which is used to enhance the bandwidth for 800 MHz operation. The reconfigurable layer metallization, which is formed on a single-sided copper clad RO4003C substrate ($160 \times 178 mm^2$, $t = 1.525$ mm), consists of meander, asymmetric arm, and pole-structure metallizations (see Figure 5.1) responsible for 220, 470, and 800 MHz operations, respectively. The DC bias circuitry used to actuate RF MEMS switches is also formed on reconfigurable layer. The small antenna element is formed by properly etching on one side of another RO4003 substrate ($16 \times 20 mm^2$, $t = 0.813$ mm) while the copper on the other side of substrate is etched away completely. Later, the short wall, as a separate structure, is attached to it by soldering (see Figure 5.2). This entire structure, namely small antenna element is responsible for 4900 MHz operation. After all the individual layers (top patch layer, reconfigurable layer, and small antenna element) are fabricated on the corresponding substrates, the following steps are needed to form the 3-D architecture:

1. Solder both the outer conductor of coax and ground wall to the reconfigurable layer metallization.

2. Attach the small antenna element to the inner conductor of the coaxial cable by soldering.

3. Solder the other end of the short wall (on small antenna element) and the inner conductor of the coaxial cable to the capacitive feed metallization.

4. Solder the ground wall to the top patch metallization on the other end.

To aid in the mechanical robustness of the 3-D architecture, polymethacrylimide foams (r=1.043) [52] are placed underneath the top patch layer and small antenna element. Two MEMS switches are integrated at strategic locations of the reconfigurable layer metallization to provide reconfigurability between mode 1 and mode 2 of operations. The bias lines on the reconfigurable layer namely V_{cc} and Gnd (see Figure 5.4) are used to apply the necessary DC actuation voltage to activate the RF MEMS switches. These bias lines are delimited by surface mountable (SMD) inductors and resistors (RF chokes - 8.7 nH; resistors - 500 k) to eliminate their deleterious coupling effect on antenna performances. The critical design parameters of the antenna provided in Figures 5.1, 5.2, 5.3, and 5.4 are optimized by using ANSYS HFSS [53] as explained in the following sections.

5.1.2 Mode 1: 220, 470, and 4960 MHz Operation

ANSYS HFSS ver. 13 [53] was used to carry out numerical analyses for the design. The OFF state capacitance (=30fF) and ON state resistance (=1Ω) of the RF MEMS switch are taken into account during the design, which was modeled using impedance boundary conditions. The operation of mode 1 is achieved when both the MEMS switches on the reconfigurable layer are switched ON. With this switch status in mode 1, the pole-structure is connected to the asymmetric arm and meander metallizations (see Figures 5.5(a) and 5.5(b)).

The metallization connecting the outer conductor of coaxial cable to the pole-structure and ground wall, namely RF Ground is depicted in Figure 5.4. The RF energy is coupled to the top patch through the capacitive feed to compensate for the inductance of coaxial feed. The RF ground metallization in the reconfigurable layer is extended by means of pole-structure and meander metallizations as shown in Figures 5.1 and 5.4. These two

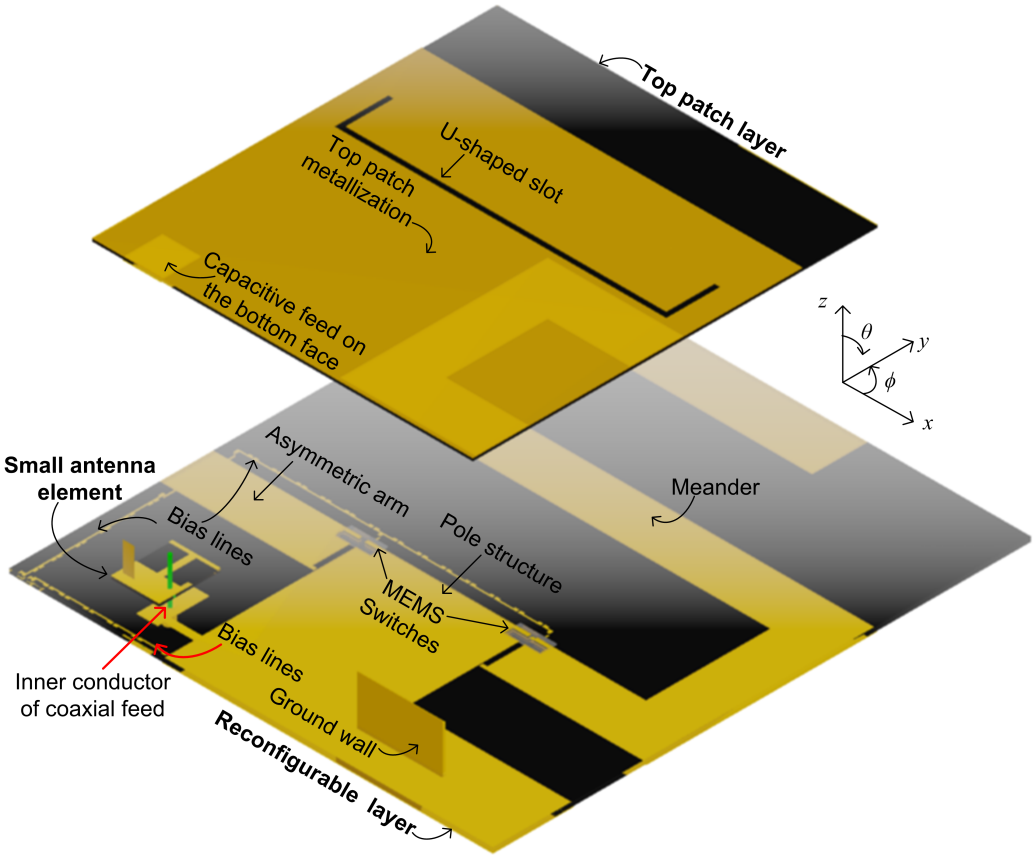

Fig. 5.1: 3-D schematic of the antenna (for the sake of illustration the top patch layer is suspended on top of the reconfigurable layer).

metallizations, as shown in Figure 5.5(a), together provide the $\lambda/4$ resonant length at 220 MHz denoted by

$$L_{F1} \sim L_{sp} + L_P + L_{m1} + L_{m2} + L_{m3}/2 + W_{md} + W_{md1}. \tag{5.1}$$

(Please find L_{F1} in Figure 5.5(a); for the rest of parameters see Figure 5.4). The working mechanism of the antenna at 220 MHz is similar to that of inverted-F meander antenna in Saito and Fukusako [54], in which the meander is $\lambda/4$ resonant. The difference in the design presented in this work, is that the meander is implemented as an extension to the RF ground. This approach has the advantage of creating broadband behavior at 800 MHz as explained in Section 5.1.3. The electro-magnetic (EM) coupling from top patch metallization sources the $\lambda/4$ resonant structure (meander + pole-structure) and the ground wall provides series

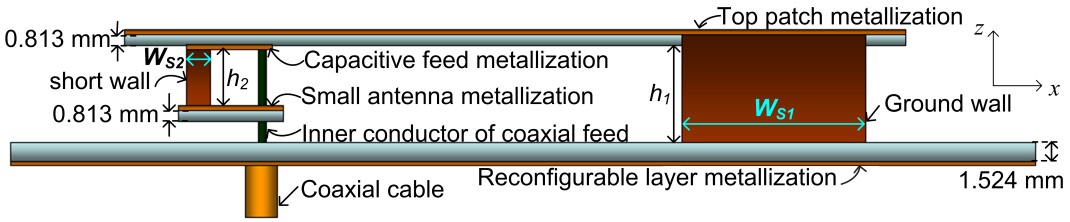

Fig. 5.2: Cross section view of the antenna.

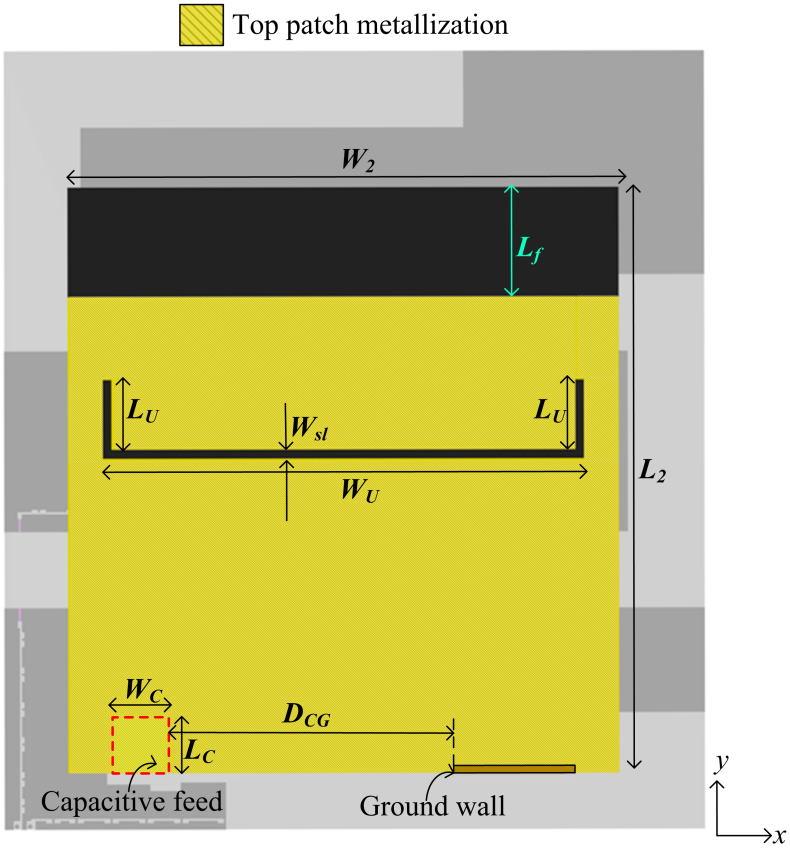

Fig. 5.3: Top view of the antenna showing critical design parameters of top patch.

reactive tuning to enhance the input matching at 220 MHz. An air layer of height h_1 is used between the reconfigurable and top patch layers to improve the antenna performances. As this is not a perfectly unbalanced structure, an RF choke balun is also used in the coaxial feed structure.

At 470 MHz, the working mechanism is similar to an asymmetric dipole. The EM coupling from top patch metallization sources the two arms of the dipole with surface currents L_{F2a} and L_{F2b} as shown in Figure 5.5(b). Accordingly, the surface current

$$L_{F2} = L_{F2a} + L_{F2b}, \tag{5.2}$$

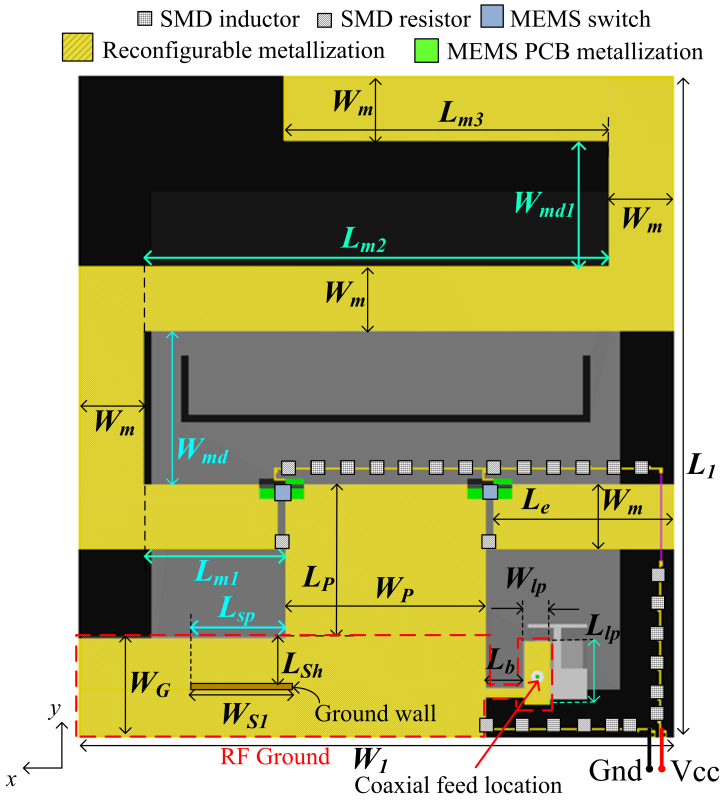

Fig. 5.4: Bottom view of the antenna showing critical design parameters of reconfigurable layer.

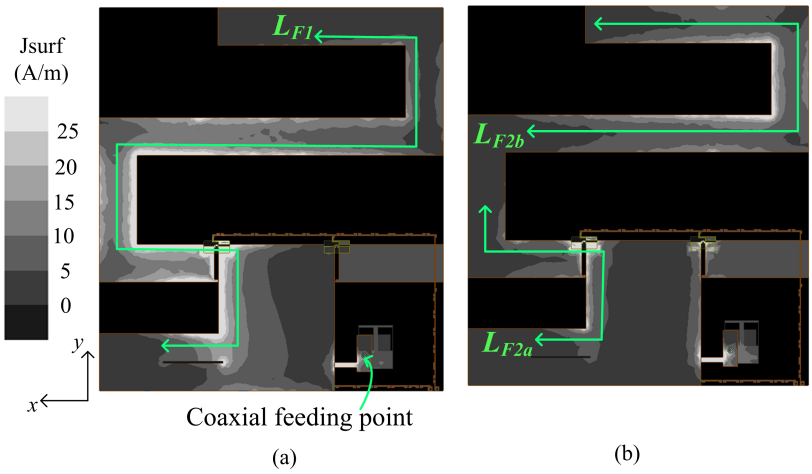

Fig. 5.5: Simulated surface current plot of the antenna (bottom view) at (a) 220 MHz, and (b) 470 MHz.

provides $\sim \lambda/2$ resonant length at 470 MHz, where, the corresponding lengths of surface currents are

$$L_{F2a} \sim L_{sp} + L_P + L_{m1} + W_{md}/3, \tag{5.3}$$

and

$$L_{F2b} \sim L_{m2} + W_{md1} + L_{m3}. \tag{5.4}$$

(Please find parameters L_{F2a} and L_{F2b} in Figure 5.5(b); for the rest of parameters see Figure 5.4). In order to understand the effect of the asymmetric arm, on 470 MHz resonance, HFSS [53] simulations were run. The reflection coefficient results of these simulations, shown in Figure 5.6, compare the performance of designs with and without the asymmetric arm. It is evident from these results that the asymmetric arm creates an extra resonance at ∼600 MHz which helps in impedance matching of antenna at 470 MHz.

To further investigate the behavior of the antenna, the effect of lengths of surface currents L_{F1} and L_{F2} on the reflection coefficient at 220 MHz and 470 MHz is studied. Change in the design parameter L_{m3} (in Figure 5.4) varies both L_{F1} and L_{F2}. As shown in Figure 5.7, change in the length of surface current L_{F1} resulted in a shift in the resonant frequency of 220 MHz operation, with L_{F11} (= 405 mm), L_{F12} (=360 mm), and L_{F13} (=300 mm) being $\sim \lambda/4$ resonant lengths at f_{c11} (212MHz), f_{c12} (217MHz), and f_{c13} (223MHz),

respectively. Moreover, as the resonance f_{c1} varies, the frequency f_{c2} also shifts, with L_{F21} (=405 mm), L_{F22} (=360 mm), and L_{F23} (=300 mm) being $\sim \lambda/2$ resonant lengths at f_{c21} (421MHz), f_{c22} (456MHz), and f_{c23} (496MHz), respectively. Hence, in this design, a careful design optimization needs to be employed to jointly obtain the targeted frequency bands: 220 MHz and 470 MHz without losing the impedance matching in either of them. The working mechanism of the antenna at the highest frequency of operation (4960 MHz) is explained in a separate section (Section 5.1.4) as it is common to modes 1 and 2.

5.1.3 Mode 2: 800 and 4960 MHz Operation

For the antenna to operate at 800 MHz in mode 2, both the MEMS switches need to be

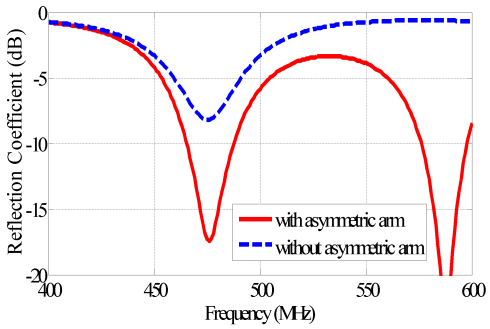

Fig. 5.6: Comparison of reflection coefficient plots of designs with and without asymmetric arm metallization.

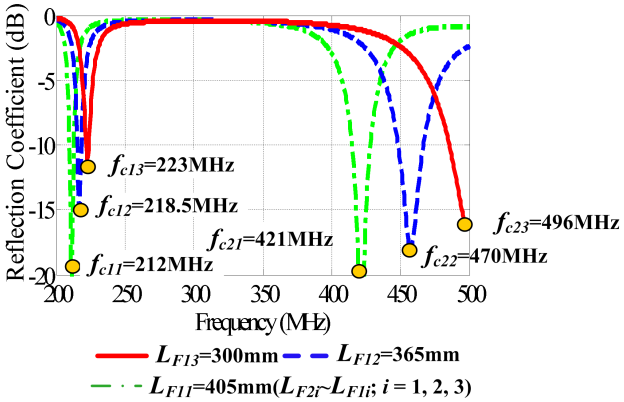

Fig. 5.7: Effect of change in parameter L_{F1} (which is $\sim L_{F2}$) on 220 MHz and 470 MHz bands.

switched off. In other words, the pole-structure metallization should be disconnected from the meander and asymmetric arm metallizations. In order to create a broadband behavior at 800 MHz, two closely spaced resonances at 750 MHz and 830 MHz were combined in this design. The pole-structure metallization in Figure 5.8(a), when disconnected from the rest of the reconfigurable layer metallization provides $\sim \lambda/4$ resonant length at 750 MHz denoted by

$$L_{F3} \sim L_P + L_{sp}. \tag{5.5}$$

(Please find parameter L_{F3} in Figure 5.8(a); for the rest of parameters see Figure 5.4) In addition to this, the U-shaped slot etched on the top patch metallization in Figure 5.8(b) contributes $\sim \lambda/4$ resonant length at 830 MHz which is denoted by

$$L_{F4} \sim L_U + W_U/2. \tag{5.6}$$

(Please find parameter L_{F4} in Figure 5.8(b); for the rest of parameters see Figure 5.3).

In addition to this, Figure 5.8(b) depicts the presence of surface current around the U-shape slot having a symmetry with respect to y-axis. In essence, the surface currents on the top patch cancel in x-direction and add up in y-direction to effectively orient the slot in y-direction. This phenomenon preserves the pattern integrity at 800 MHz as the main

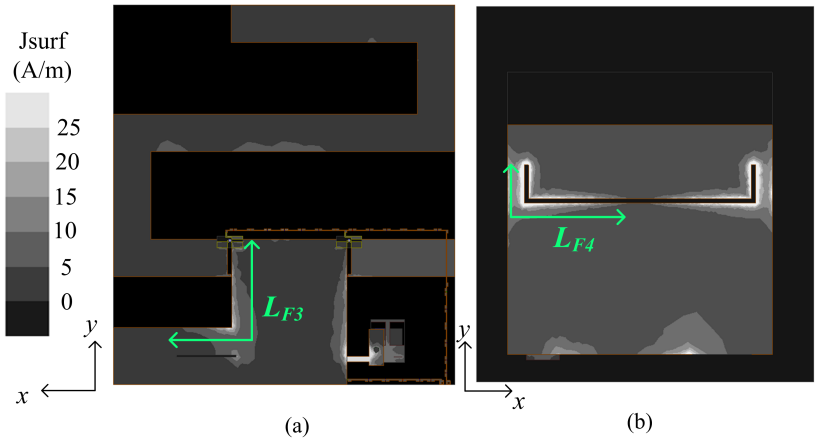

Fig. 5.8: Simulated surface current plot of the antenna at (a) 750 MHz (bottom view), and (b) 830 MHz (top view).

radiating elements in all the other bands of operation (220 MHz, 470 MHz, 750 MHz, and 4960 MHz) are also oriented along y-direction.

The broadband behavior of the antenna can be further analyzed by understanding the effect of parameters L_{F3} and L_{F4} on 750 MHz and 830 MHz bands, respectively. For this parametric study, the lengths of surface currents, L_{F3} and L_{F4} are varied by the design parameters L_P and L_U, respectively. As shown in Figure 5.9, change in the parameter L_{F3} when L_{F4}(=79 mm) is fixed resulted in a shift in the resonant frequency, with L_{F31}(=90 mm), L_{F32}(=80 mm), and L_{F33}(=70 mm) being $\sim \lambda/4$ resonant lengths at f_{c31}(650MHz), f_{c32}(690MHz), and f_{c33}(750MHz), respectively. Similarly, in Figure 5.10, the resonant frequency f_{c4} is controlled by the parameter L_{F4} with L_{F41}(=79 mm), L_{F42}(=73 mm), and L_{F43}(=67 mm) being $\sim \lambda/4$ resonant lengths at f_{c41}(830MHz), f_{c42}(880MHz), and f_{c43}(960MHz), respectively, when the parameter L_{F3} (=70mm) is fixed. Hence, both the frequencies can be controlled independently by polestructure and U-shaped slot dimensions and suitably combined to result in a broadband behavior.

5.1.4 Operation at 4960 MHz Band

The geometrical structure of small antenna element is very similar to the larger antenna (responsible for 220, 470, and 800 MHz bands) into which it is integrated in a multi-layered architecture to provide the operation at the highest frequency 4960 MHz. The small antenna

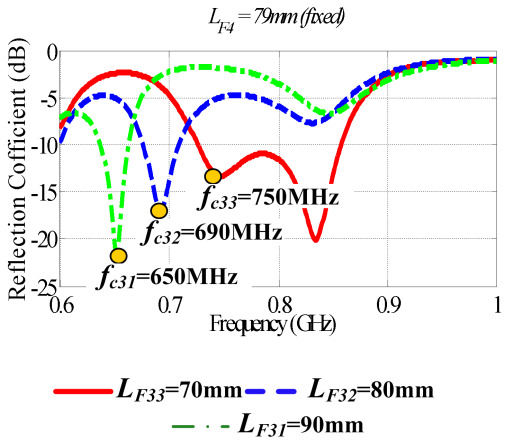

Fig. 5.9: Effect of change in parameter: L_{F3} on 750 MHz.

element, geometrical details of which are given in Figure 5.11, is continuously operating at 4960 MHz irrespective of the status of the MEMS switches. In contrast to the multi-layered structure in Hsu et al. [20], this antenna uses only one coaxial feed to provide RF energy to both the antennas. The main components of the larger antenna are connected to the outer conductor of coax and those of small antenna element are connected to the inner conductor of coax. This structure is advantageous in providing a compact multi-layered design with one coaxial feed. The small antenna element has its main radiating element oriented along the y-axis, hence, the integrity of radiation pattern is preserved. The simulated plot in Figure 5.12 indicates surface current concentration on the small antenna element at 4960 MHz. This confirms that the main radiating element is within the small antenna element whose resonant length, denoted by

$$L_{F5} \sim L_{p1} + W_t/2. \tag{5.7}$$

(Please find parameter L_{F5} in Figure 5.12; for the rest of parameters see Figure 5.11), is $\sim \lambda/4$ at 4960 MHz.

From Figure 5.12, it is also evident that at 4960 MHz the larger antenna has almost no surface current on it and hence is transparent to the small antenna element operating at a much higher frequency. Also, the RF ground metallization under the small antenna element (see Figure 5.4) has been etched away to help in omni-directional radiation at 4960MHz.

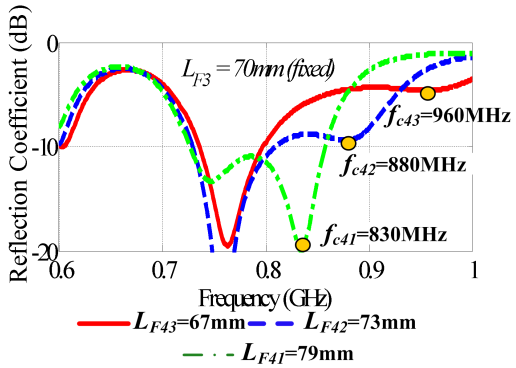

Fig. 5.10: Effect of change in parameter: L_{F4} on 830 MHz.

The short wall and the capacitor patch provide the reactive tuning to match the small antenna element.

To further support the working mechanism of the antenna, the effect of parameter L_{F5} on the resonant frequency of 4960 MHz is studied. For this parametric study, the design parameter L_{p1} (see Figure 5.11) is varied in order to change the length of surface current L_{F5}. As shown in Figure 5.13, independent of the parameters of the larger antenna, change in the parameter L_{F5} resulted in a shift in the resonant frequency with L_{F51}(=22 mm), L_{F52}(=18mm), and L_{F53}(=14mm) being $\sim \lambda/4$ resonant lengths at f_{c51}(4.75GHz),

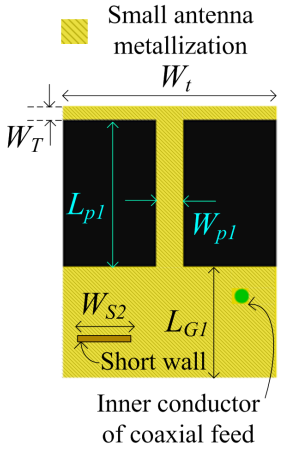

Fig. 5.11: Geometrical details of the small antenna element.

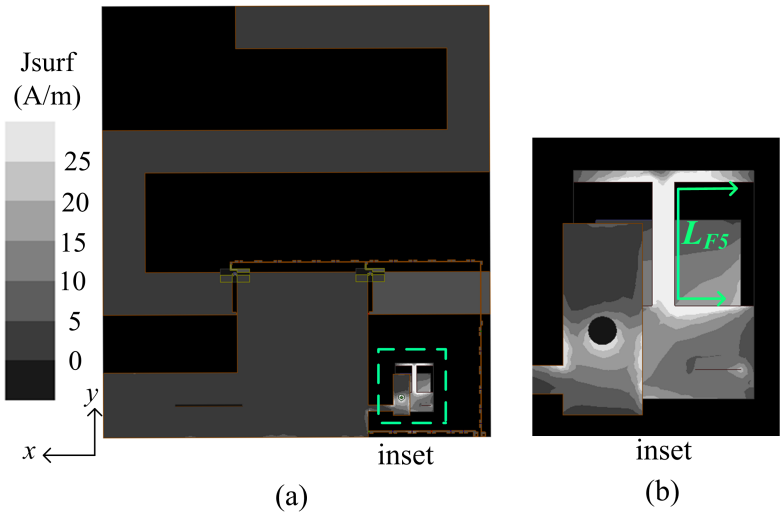

Fig. 5.12: Simulated surface current plot of the (a) entire antenna (bottom view), and (b) inset of small antenna element at 4960 MHz.

f_{c52}(4.87GHz), and f_{c53}(5.1GHz), respectively. The optimized parameters of the antenna are provided in Table 5.1.

5.2 Switch Fabrication and Integration

The switches used are ohmic contact, series RF MEMS switches, and they are specifically designed and fabricated by the authors for the proposed antenna. The switches are fabricated on 4 inch, quartz substrates ($\epsilon_r = 3.9$, $\tan\delta = 0.0001$) using a 5-mask surface micromachining process, which is illustrated in Figure 5.14(a)-(f). This process is very similar to the RADANT switch process [55,56]. It starts with sputtering and patterning of the 200 nm TaN resistive layer which has a surface resistance of 4 kΩ/square, and is used as resistive bias line for the switches (Figure 5.14(a)). Next, 10/200 nm of Cr/Au is deposited by thermal evaporation and patterned (Figure 5.14(b)), which is the first metal layer of the switches. Then, 1000 nm of Poly Methyl Methacrylate (PMMA) spin coated and cured as a sacrificial layer. It is patterned two times in order to define anchor parts of the switches and to open partial openings for the dimples (Figure 5.14(c)), which are formed at the tip of the cantilever and used for obtaining good metal to metal contact. A 200 nm Au seed layer is coated by thermal evaporation (Figure 5.14(d)), which is followed by the electroplating of the MEMS cantilevers, which also increases the thickness of the metal layer on the switches (Figure 5.14(e)). The final steps are the wet etching of the seed layer, wet etching of the sacrificial layer, and release of the RF MEMS switches using critical point drying (Figure

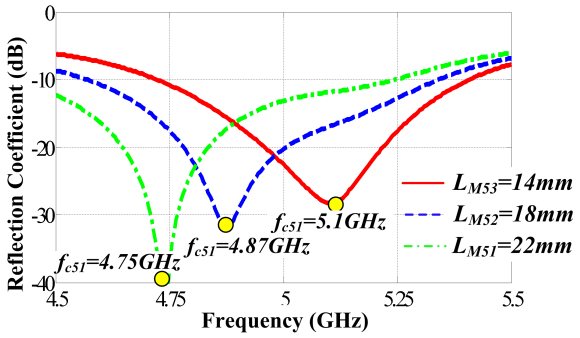

Fig. 5.13: Effect of change in parameter L_{F5} on 4960 MHz band.

Table 5.1: The optimized parameters of the proposed antenna design (in millimeters).

Parameter	*Value*	*Parameter*	*Value*	*Parameter*	*Value*
L_1	178	W_{lp}	7	W_{S1}	28
W_1	160	L_e	48.5	W_G	26.8
L_P	41.4	L_{m1}	36	W_m	17.5
W_P	54	L_{m2}	125	L_2	134
W_{md}	41.3	L_{m3}	87.5	W_2	126
W_{md1}	33.7	L_f	25	L_c	13.2
L_U	110	L_{G1}	8.3	W_c	12.7
W_U	16	W_t	16	W_{S2}	4
L_{p1}	11	W_{p1}	2	W_{sl}	2
L_{lp}	17	L_b	10.3	W_T	1
h_1	16.7	h_2	10.1	L_{sp}	26
D_{CG}	65				

5.14(f)). The SEM picture of the fabricated switch is shown in Figure 5.15.

The fabricated RF MEMS switches have been tested both for DC and RF performances. The DC tests have been performed using Agilent 4156C semiconductor parameter analyzer together with a DC probe station. The pull-down and operation voltages of the switches are 100 V and 120 V, respectively. The measured on-state DC resistance varies between 1-to-1.8 Ω. The calculated switching time is 5 μs. We have not run separate reliability tests on our switches, however, no failure has been observed throughout the testing of the switches integrated on the antenna.

For the RF characterization of the RF MEMS switches, Agilent 8722ES network analyzer has been used with a two-port, SOLT calibration in 1-20 GHz frequency band. The measured insertion loss and isolation of the switch at 5 GHz, which is the maximum frequency of interest, is better than 0.15 dB and 21 dB, respectively. In Figure 5.16, the measurement results of the fabricated switch in comparison with the simulation results shows very good agreement. The performances of the in-house fabricated MEMS switches are quite comparable to those of Radant MEMS switch [47]. Although, a high actuation voltage is a disadvantage of MEMS switch technology over the semiconductor switch technologies, i.e., p-i-n diode or field-effect transistor (FET) it also has some important advantages as well.

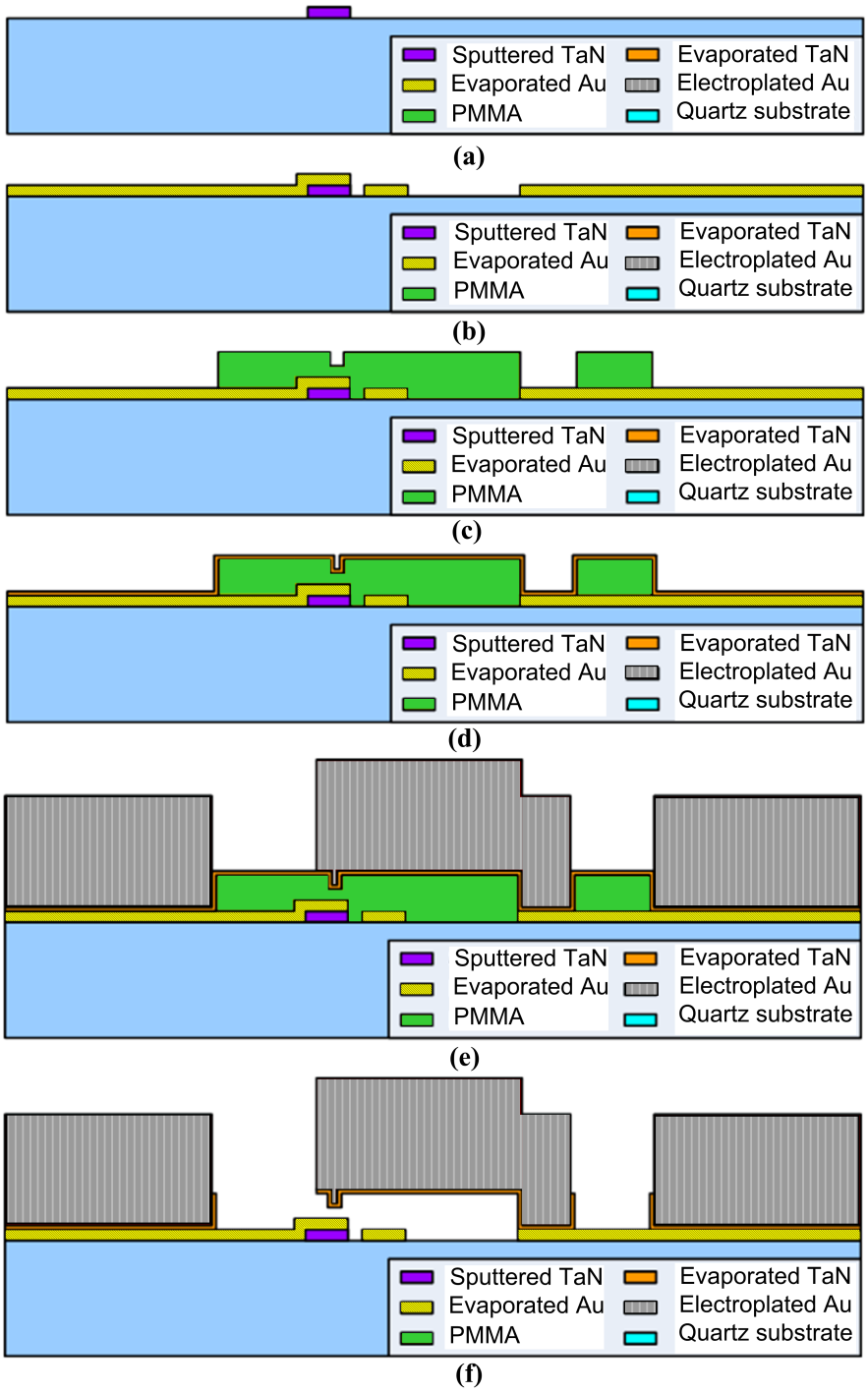

Fig. 5.14: (a)-(f) The micro-fabrication process flow of the USU ohmic contact, series RF MEMS switch.

1. A MEMS switch draws negligible amount of current in nano amperes as compared to a typical p-i-n diode drawing several milliamperes of current, which results in exceedingly low power consumption.

2. The performance metrics such as insertion loss and isolation of MEMS are better than a p-i-n diode or FET over the entire frequency of operation (220860 MHz).

3. Although it was not applied in this structure, MEMS can also be monolithically integrated into the antenna structure, which is not possible for semi-conductor switches namely p-i-n diode or FET.

As shown in Figure 5.17, the MEMS switch is initially integrated onto a small PCB with metallization to support three terminals namely RF-in, RF-out, and bias pad. This metallization is etched on single-sided copper clad RO4003C substrate ($12 \times 5.5mm^2$, t=0.508mm) with gold plating. The choice of gold plating aids in the wire-bonding of MEMS devices. The MEMS switch is initially attached to the MEMS PCB by epoxy and the three terminals of MEMS switch are wirebonded to the corresponding metallizations on the MEMS PCB (see Figure 5.17). Now, the MEMS PCB which houses the MEMS switch, is soldered to the reconfigurable layer metallization of the antenna at the required location. The bias pad is useful in applying DC voltage to actuate the MEMS switch. The photographs of the fabricated MEMS integrated antenna are shown in Figure 5.18.

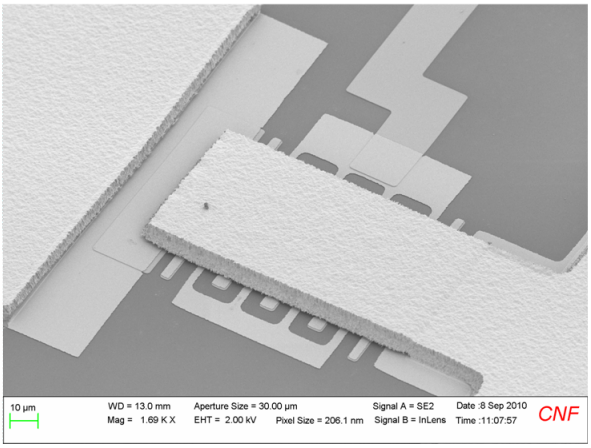

Fig. 5.15: SEM picture of fabricated MEMS device.

5.3 Results and Discussion

The reflection coefficient measurements of the fabricated antenna are made using Agilent 8722ES network analyzer with a one-port Short-Open-Load (SOL) calibration in 100 MHz- 6000 MHz frequency band. Figure 5.19 shows excellent agreement with simulated results where, ∼3%, 4%, 20%, and 17% fractional bandwidths have been measured in 220MHz, 470MHz, 800 MHz, and 4960 MHz bands, respectively.

To obtain the radiation patterns, the antenna prototype is placed on a rotor in the

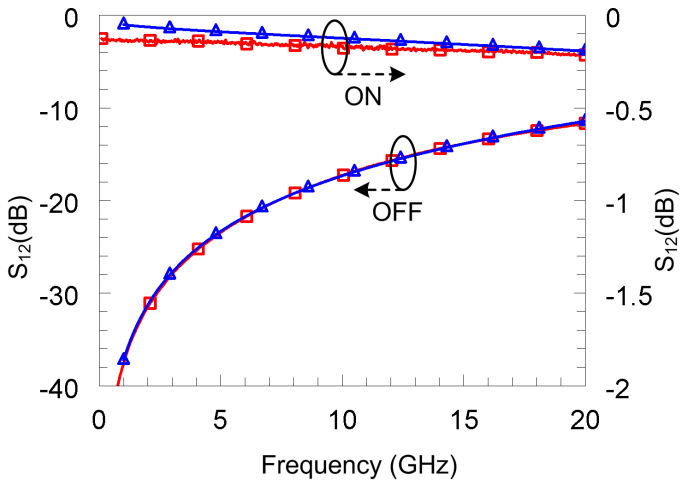

Fig. 5.16: The measurement results of the USU Ohmic Contact RF MEMS switch compared with the simulations.

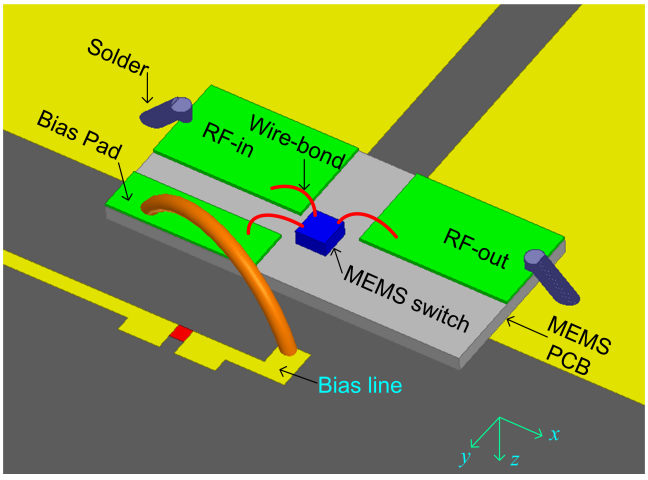

Fig. 5.17: Detailed schematic showing the integrated MEMS device within the antenna structure.

anechoic chamber, and a power supply was used to actuate the MEMS switches. The two-dimensional gain patterns of the antenna in xz- and xy-planes for all the PS bands are shown in Figures 5.20, 5.21, 5.22, and 5.23. The measured radiation patterns of the antenna could not be obtained at 220 MHz as the measurements were below the noise threshold. As seen from these figures, the measured and simulated radiation patterns agree reasonably well. A dipole-type radiation pattern is expected from the geometry and orientation of the main radiating elementsmeander, pole-structure, and small antenna elements. Correspondingly, a cosϕ-pattern in xy-plane and omni-directional pattern in xz-plane, in all four bands of operation (see Figures 5.20, 5.21, 5.22, and 5.23), confirms the analysis. The reduction of gain in the x-direction at 750 MHz may be attributed to the meander metallization. Although disconnected from pole-structure in mode 2, the close proximity of the meander metallization reduces the gain of the antenna along x-direction in xz- and xy-planes at 750 MHz. Moreover, the nulls in the radiation pattern along the $\theta = 15^o, -60^o$ directions in xz-plane at 4960 MHz may be attributed to the top patch metallization. Also, the null along x-direction in xy-plane at 4960 MHz might be due to pole-structure and asymmetric arm metallizations of the larger antenna. It is understood that these metallizations hin-

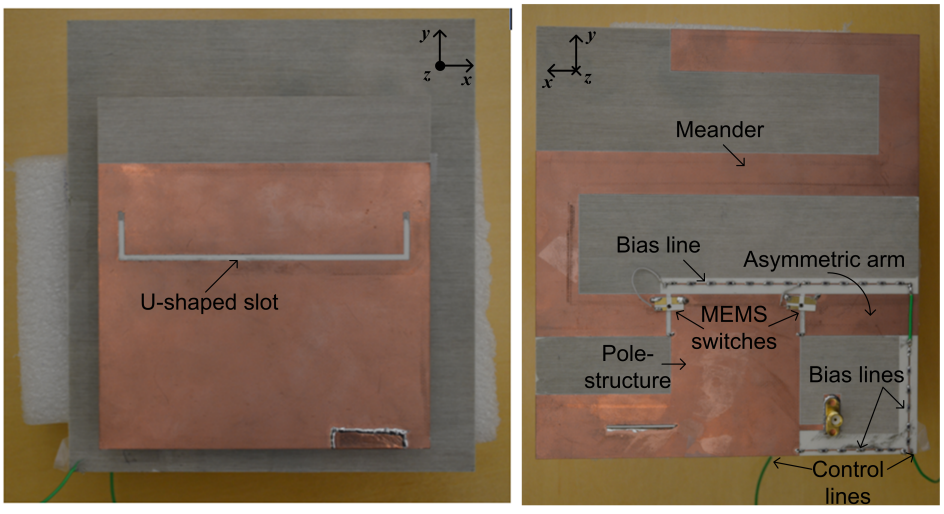

Fig. 5.18: Photographs of fabricated prototype of the MEMS integrated antenna - (a) bottom view, and (b) top view.

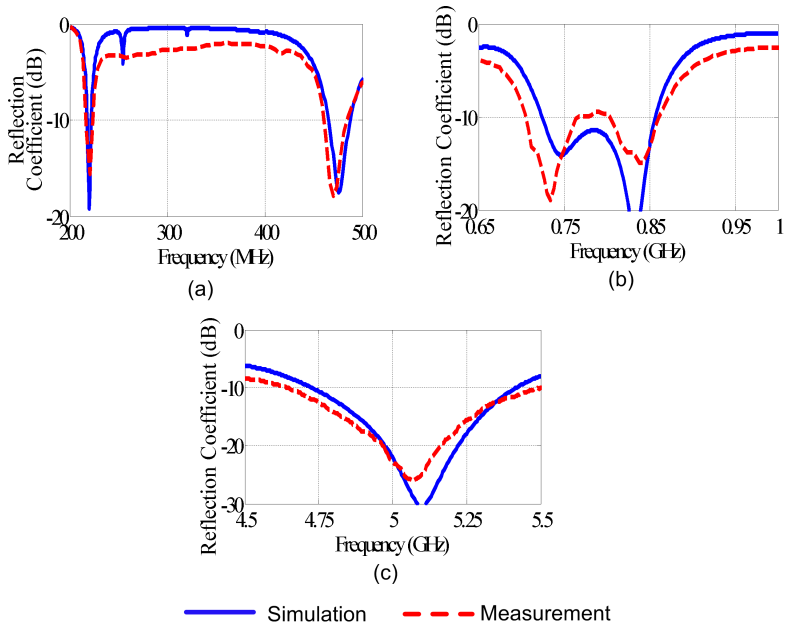

Fig. 5.19: Simulated and measured reflection coefficients of the antenna in (a) mode 1: 220 MHz, 470 MHz, (b) mode 2: 800 MHz, and (c) mode 1/2: 4960 MHz bands.

der the omni-directional capability of the small antenna element in those directions. The slight discrepancies between simulated and measured radiation patterns at 4960 MHz may be attributed to the high interaction of small antenna element with rotor and undesired radiation from power supply cables. The efficiency of the antenna has been measured using the well-known Wheeler-Cap method and is shown in Figure 5.24. The measured efficiencies of the antenna are ∼75%, 90%, and 60-90% over 220, 470, and 700 - 850 MHz frequency bands, respectively indicating a highly efficient radiator. The efficiency of the antenna at 4.9 GHz cannot be measured due to self-resonances of the Wheeler cap.

5.4 Conclusion

An electrically small RF MEMS integrated quad band antenna for Public Safety wireless communication systems is presented in this work. Combination of multi-band, broadband, multi-layered, and frequency reconfiguring techniques lead to a compact antenna design with simple architecture capable of operating over 220 MHz, 470MHz, 800 MHz, and 4960 MHz bands. Measured fractional bandwidths of ∼3%, 4%, 21%, and 17% have

been obtained in the four PS bands while maintaining the integrity in the radiation pattern.

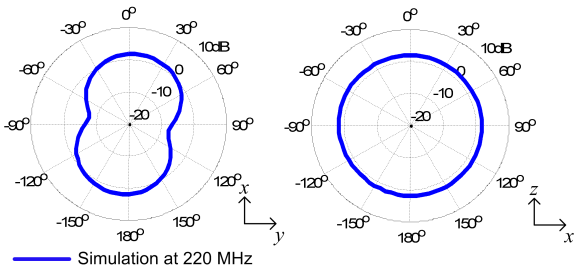

Fig. 5.20: Simulated and measured gain plots in xz- and xy-planes at 220 MHz.

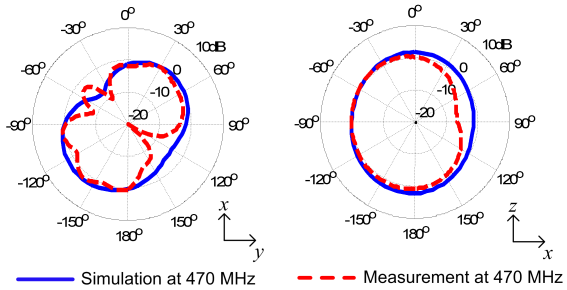

Fig. 5.21: Simulated and measured gain plots in xz- and xy-planes at 470 MHz.

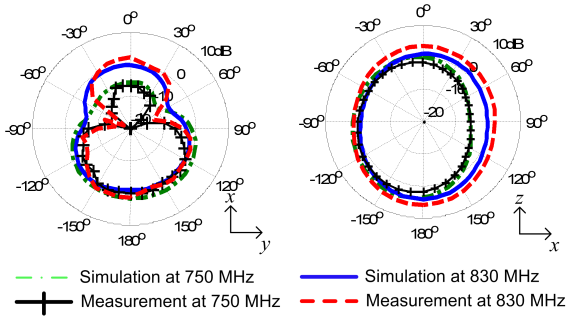

Fig. 5.22: Simulated and measured gain plots in xz- and xy-planes at 800 MHz.

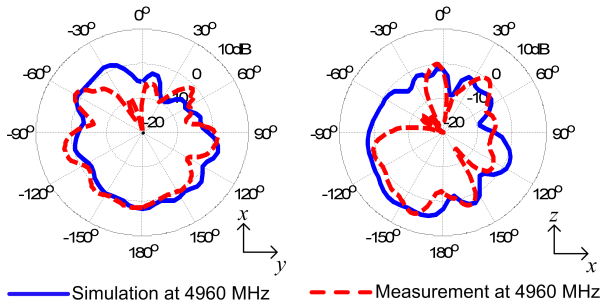

Fig. 5.23: Simulated and measured gain plots in xz- and xy-planes at 4960 MHz.

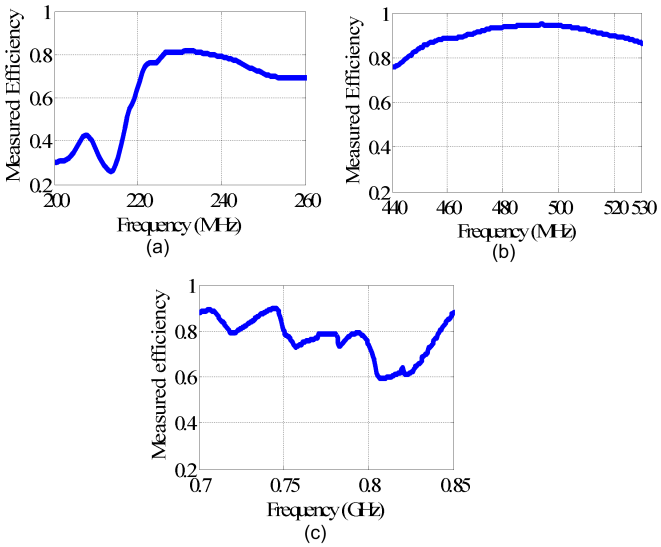

Fig. 5.24: Measured efficiencies of the antenna at (a) 220 MHz, (b) 470 MHz, and (c) 800 MHz.

Chapter 6

Pattern Reconfigurable Antenna for PS Applications

6.1 Antenna Structure and Working Mechanism

6.1.1 3-D Architecture and Integrated Components

The 3-D schematic and cross sectional diagrams of the pattern reconfigurable antenna are shown in Figures 6.1 and 6.2. The antenna architecture consists of three layers namely: Patch layer, Dielectric layer, and Reconfigurable parasitic layer. The patch layer consists of a coaxial fed patch antenna whose patch (with lateral area $S_x \times S_y mm^2$) and ground (with lateral area $L \times W mm^2$) metallizations are formed on either side of a 1.524 mm thick RO4003C substrate ($\epsilon_r = 3.55$, $\tan \delta = 0.0021$). The dielectric layer consists of three RO4003C substrates, with metal totally etched (removed) from both sides, stacked together. One of them (of 1.524 mm thickness) is cut into U-shape to encapsulate the surface mount devices (SMD) which are soldered to the lower face of the parasitic layer to provide DC bias circuitry (see Figures 6.2 and 6.3). The other two of them, with 1.524 mm and 0.813 mm thicknesses, serve to provide the dielectric medium between patch and reconfigurable parasitic layers. The low loss RO4003 substrate helps to reduce the size of the overall reconfigurable antenna.

The reconfigurable parasitic layer is formed on another 0.508 mm thick RO4003C substrate. The upper face of parasitic layer consists of 3 x 3 pixel metallization (each pixel having $P_x \times P_y mm^2$ lateral area) with gaps ($g_x \times g_y mm^2$) between adjacent pixels to integrate components, whereas, the lower face has the DC bias line metallization. Inset 1 of Figure 6.1 shows the components in the gaps between adjacent pixels on the upper face of parasitic layer: the interconnecting pin-diodes, DC-block capacitors (=1.8pF), and RF choke inductors ($I_1 = 1.8$ nH) in parallel to the pin-diodes. To choke RF from entering into

ground bias line (Gnd line in inset 2 of Figure 6.1) from pixels, another inductor (I_2 = 8.7 nH) is also integrated as shown in inset 2 of Figure 6.1. The DC connector is soldered to the connector pads (not shown in Figure 6.1) for supplying the actuation voltage (0V/1.5V) to pin-diodes.

The lower face of the parasitic layer has bias line metallization delimited by RF choke inductors (I_2 = 8.7 nH) in territory 1 and bias resistors (R = 62Ω) in territory 2 as shown in Figure 6.3. The 13 bias lines (1 Gnd + 12 actuation lines) supply the actuation voltage(0V/1.5V) and ground (0V) to the anode and cathode teminals of pin-diodes, respectively, through the plated vias(of 0.75 mm diameter). These vias connect the bias line and ground line metallizations on upper and lower faces of parasitic layer. The DC connector pads on the upper and lower faces of the parasitic layer are also connected through a different set of vias (of 1 mm diameter).

6.1.2 Biasing Scheme

The theory behind the working mechanism of a parasitic pixel layer based pattern reconfigurable antenna is explained in Yuan et al. [23]. Hence, it is not repeated here. The practical implementation of RF switching with the associated control circuitry and the reason behind the choice of particular SMD components (pin-diodes, RF chokes, bias resistors, and DC block capacitors) is explained in this work. The RF switch chosen for reconfigurability is Surface Mount Pin (SMP1345) from skyworks [57].

This switch provides an isolation of ~ -9dB and insertion loss of ~ -0.4dB at 4.96 GHz as provided from its datasheet [57]. The switch was modelled as a parallel combination of 0.12pF capacitance (C_{off}) and 2.5 kΩ resistance for OFF state; and 1.5Ω resistance (R_{on}) for ON state by a lumped RLC boundary condition in HFSSv14 [58].A series inductance of 0.7 nH is added to the pin-diode model to represent the lead inductance of SMP. The values of resistance and capacitance for the OFF and ON states of the switch were obtained from datasheet [57].

The inductor I_1 serves to connect all pixels together (DC-wise), thereby, providing DC ground to the cathodes of all pin-diodes. The ground voltage is supplied by the Gnd bias

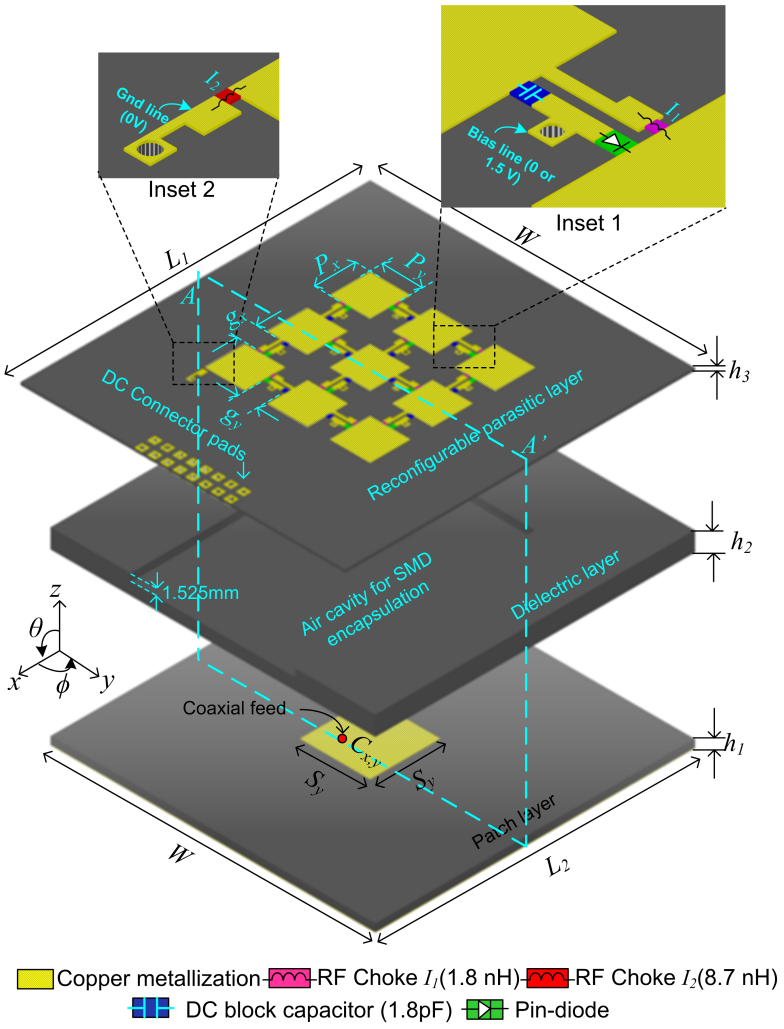

Fig. 6.1: 3-D schematic (for the sake of illustration the layers are suspended on top of each other) of the pattern reconfigurable antenna.

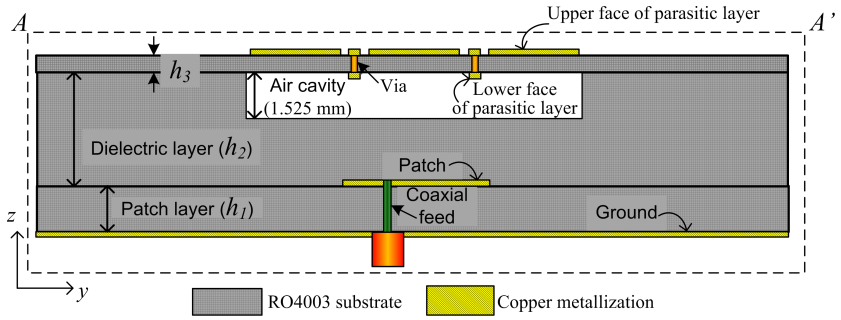

Fig. 6.2: Cross-sectional view of the pattern reconfigurable antenna.

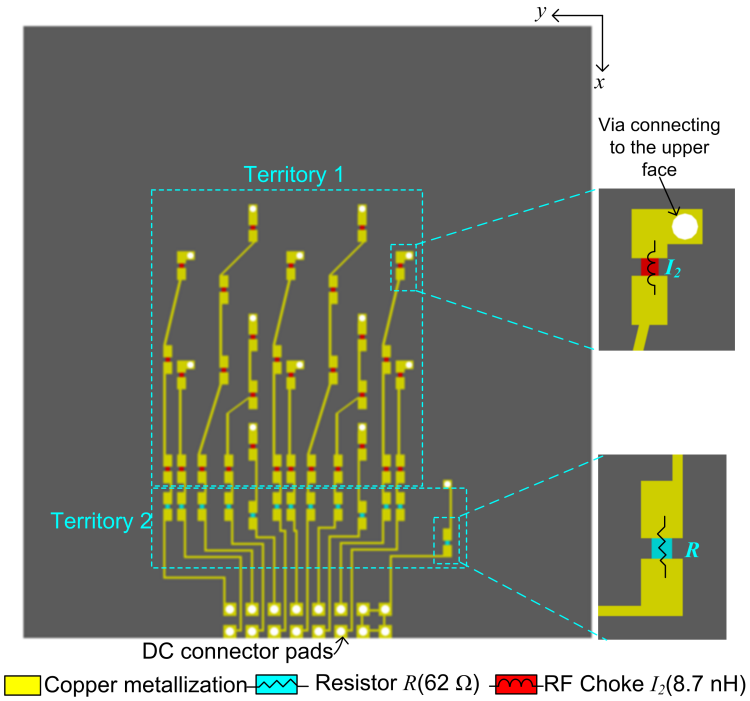

Fig. 6.3: Bottom view showing lower face of the parasitic layer with integrated SMD components.

line, shown in inset 2 of Figure 6.1. As already explained, the actuation voltages (0V/1.5V) applied through the 12 bias lines (on the lower face of the parasitic layer) are present at the anodes of pin-diode. The DC block capacitor (= 1.8pF) connected between the anode terminal of pin-diode and the adjacent pixel blocks the actuation voltage from being applied to the other pixel. Hence, the RF switches can be controlled individually through the bias lines.

The DC block capacitor is modelled as a series LC resonant circuit in HFSS using

$$SRF = \frac{1}{2\pi\sqrt{LC}}, \tag{6.1}$$

where L represents the lead inductance of the SMD, C (= 1.8pF) is the value of the capacitance chosen, and SRF (= 5.1 GHz) is the self resonant frequency obtained from datasheet. From Eq. (6.1) L is calculated as 0.54nH and it is verified that this series resonance provides sufficiently low impedance to RF path between pixels in the frequency

band of interest (4.94 4.99 GHz). The RF choke inductor, I_2 (= 8.7 nH), delimits the bias line metallization to avoid deleterious coupling effects on targetted antenna performances. This inductor, I_2(= 8.7 nH) is modelled as a parallel LC resonant circuit using Eq. (6.1) with its C (=0.096 pF) calculated from SRF = 5.5 GHz given in the datasheet. Here, C accounts for the parasitic capacitance between the terminals of inductor. This parallel resonance is verified to provide a high impedance to the RF path over 4.94 4.99 GHz. Similarly, the inductor I_1 is also modeled as a parallel LC circuit in HFSS where C is calculated as 0.055 pF using its $SRF = 16$ GHz from datasheet.

6.1.3 Improving Isolation Between Pixels

A transmission line model was simulated in HFSS to emulate the biasing scheme of pin-diode on the parasitic pixel surface. This model, as shown in Figure 6.4, consists of a 50Ω transmission line on a 0.813mm thick RO4003 substrate, with components (pin-diode, inductor I_1, DC block capacitor, and RF choke inductor I_2) integrated on it along with bias and Gnd lines to actuate the pin-diode.

The choice of inductor I_1 affects the isolation between ports 1 and 2 of the transmission line as shown in the parametric analyses (performed in HFSS) of Figure 6.5. The inductor I_1 forms a parallel resonant circuit with the OFF state capacitance(C_{off}) of the pin-diode to result in a high impedance at resonance, thereby, improving the isolation. As the value of I_1 increases from 1.8nH to 4.8 nH the resonant frequency decreases from f_{r1} (=4.94 GHz) to f_{r2} (3.8 GHz) as shown in the analyses. Accordingly, the isolation between ports 1 and 2 deteriorates from -17 dB to -7 dB in Figure 6.5. The frequencies $f_{ri=1to2}$ are not exactly equal to the parallel resonant frequencies of $I_{1i=1to2}$ and C_{off} using Eq. (6.1). The reason being, the parasitic effects of bias lines (actuation and gnd) and the land patterns of specific SMD components (pin-diode, inductors I_1 and I_2, and DC-block capacitor) shift the resonances to much lower frequencies than those obtained from Eq. (6.1).

The isolation between ports 1 and 2, which is a measure of isolation between pixels, significantly effects the beam tilting capability of MRA. To understand this phenomenon, a set of parametric analyses, in which the value of I_1 is varied from 1.8 nH to 4.8 nH, is

performed on a parasitic layer based patch antenna with a given switch configuration in HFSS. Figure 6.6 shows the variation of gain plot of this MRA in yz plane at 4.94 GHz with respect to I_1. It is noticed that, as the value of isolation deteriorates from -17 dB (for I_{11} = 1.8 nH) to -7 dB (for I_{12} = 4.8 nH) in Figure 6.5, the maximum direction to which the beam can be tilted decreases from 45^o (G_1 =5.6dB) to 30^o (G_2 =3.7dB) in Figure 6.6.

From full-wave simulations, it was also noticed that the insertion loss between pixels, controlled by the ON state resistance (R_{on}) of the pin-diode [59], affects the maximum gain of the antenna obtained in the direction of interest. To support this argument, a parametric analyses (see Figure 6.7) was run on the HFSS model (which was used to extract the results of Figure 6.6) to see the effect of R_{on} on the maximum gain obtained. It is demonstrated that, as R_{on} increases from 0.5Ω to 12Ω, the maximum gain decreased from G_1 = 5.6dB to G_3 = 4.8dB, while maintaining the 45^o tilt in yz plane. These parametric analyses justify the reason behind choosing particular SMD components for reconfigurability.

Accordingly, the pixel-area ($P_x \times P_y mm^2$) and the thickness (h_2) of the dielectric layer

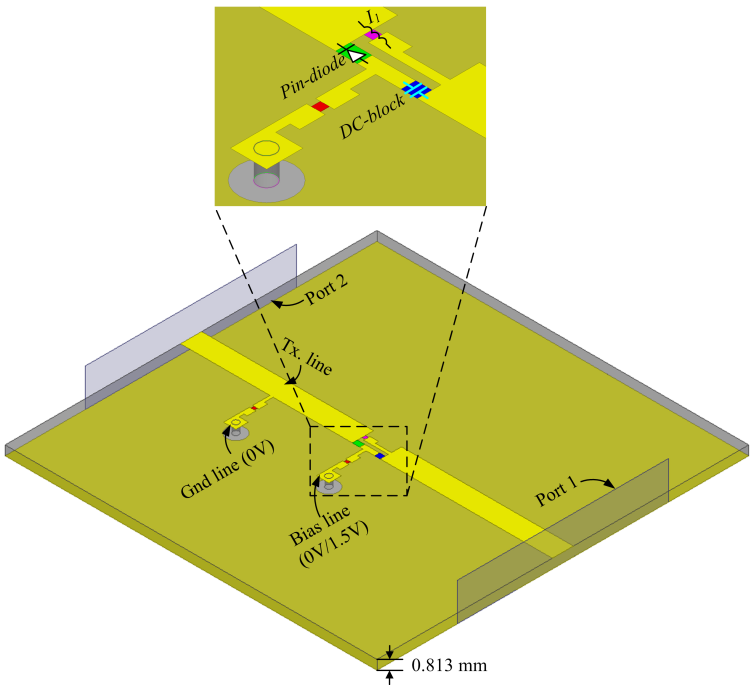

Fig. 6.4: Transmission line model in HFSS emulating the biasing scheme of pindiode on the parasitic pixel surface.

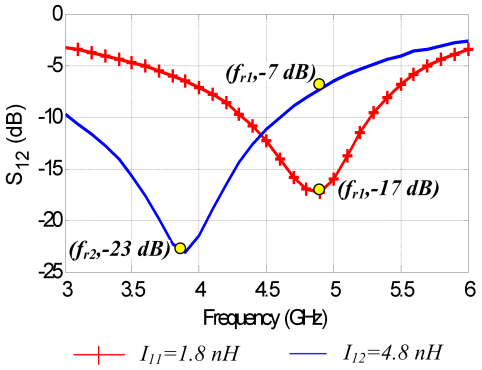

Fig. 6.5: The affect of the value of inductor I_1 on isolation (dB) between ports 1 and 2 of transmission line in Figure 6.4.

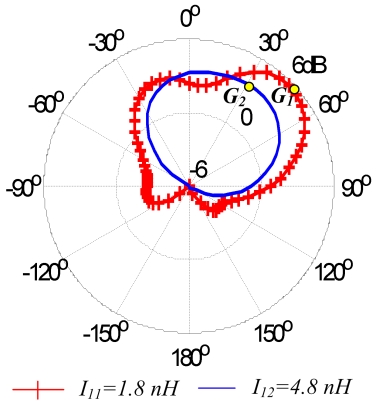

Fig. 6.6: The affect of the value of inductor I_1 on beam tilting capability of MRA at 4.94 GHz.

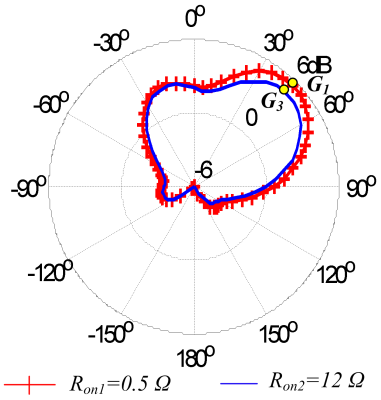

Fig. 6.7: The affect of parameter R_{on} on obtained maximum gain of MRA at4.94 GHz.

along with the dimensions of patch antenna ($S_x \times S_y mm^2$) have been optimized to maximize the gain of MRA in the directions of interest: $\theta \in -40^o, 0^o, 40^o; \phi \in -45^o, 0^o, 45^o, 90^o$ over 4.94 - 4.99 GHz band. These nine different beam directions are available in four principal planes as shown in Figure 6.8 with respect to the parasitic layer. The gap-area between pixels ($g_x \times g_y mm^2$) is fixed by the SMD component size and the space required for soldering them. The position of coaxial cable on patch is given by $C_{xy} = (C_x, C_y)$, where C_x and C_y are measured from the center of patch. The optimized parameters are given in Table 6.1.

6.2 Results and Discussion

In the presented antenna, 12 pin-diode switches are integrated between adjacent pixels on the reconfigurable parasitic layer. Their statuses, which are determined by running a multi-objective genetic algorithm (GA) optimization [60] in conjunction with full-wave

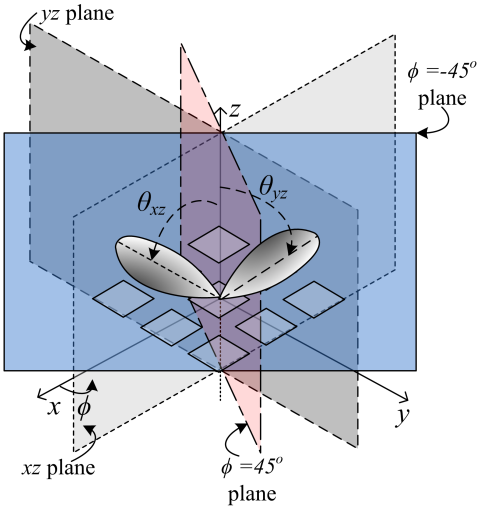

Fig. 6.8: Conceptual diagram showing the four principal planes: xz, yz, $\phi = 45^o$, and $\phi = -45^o$ planes with respect to a parasitic layer.

Table 6.1: The critical design parameters of the MRA (all dimensions are in mm).

Parameter	*Value*	*Parameter*	*Value*	*Parameter*	*Value*	*Parameter*	*Value*
P_x	8	S_x	14	g_x	4.5	h_1	1.524
P_y	8	S_y	14	g_y	4.5	h_2	3.861
h_3	0.508	W	65	L_1	70	L_2	64
C_x	0	C_y	-3.7				

analysis, result in nine different beam directions pertaining to: $\theta \in -40^o, 0^o, 40^o; \phi \in -45^o, 0^o, 45^o, 90^o$ over 4.94 - 4.99 GHz band. The upper face of the parasitic layer shows the switch numbering in Figure 6.9, in which, 0 indicates the ground pin (0V), and 1-12 are the actuation pins (0/1.5V). The corresponding optimized switch configurations are given in Table 6.2.

In Figures 6.10, 6.11, 6.12, and 6.13, the simulated results of the MRA for nine different modes of operation, is shown. As shown, 4.94 - 4.99 GHz PS band is covered in all modes of operation. The total gain plot (in dB) of the MRA showing tilted beams in four principal

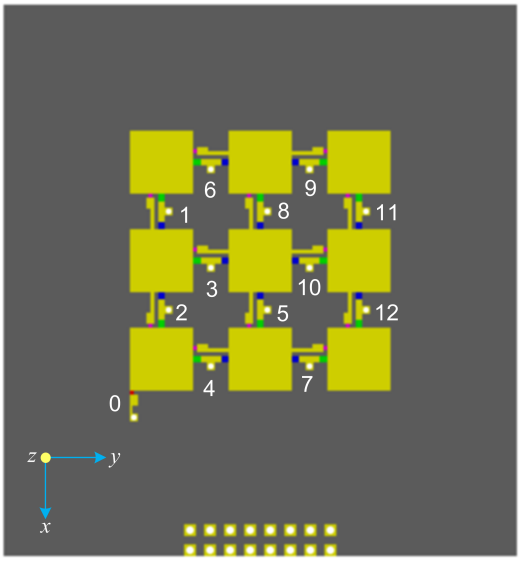

Fig. 6.9: Upper face of parasitic layer with switch numbering.

Table 6.2: Switch configurations of the antenna obtained from GA to result in nine different beam directions (0 and 1 correspond to OFF and ON states, respectively).

Switch number	*0*	*1*	*2*	*3*	*4*	*5*	*6*	*7*	*8*	*9*	*10*	*11*	*12*
$\phi = 0^o; \theta = 0^o$	0	0	0	0	0	0	0	0	0	0	0	0	0
$\phi = 0^o; \theta = 30^o$	0	1	1	0	0	1	1	0	0	0	0	1	1
$\phi = 0^o; \theta = -30^o$	0	0	1	0	1	0	0	0	1	0	0	1	1
$\phi = 90^o; \theta = 45^o$	0	0	1	1	0	0	1	0	1	1	0	0	1
$\phi = 90^o; \theta = -45^o$	0	0	1	0	1	0	1	1	1	1	1	0	0
$\phi = 45^o; \theta = 45^o$	0	0	1	0	0	1	1	1	0	1	0	1	1
$\phi = 45^o; \theta = -45^o$	0	1	1	0	1	0	1	1	0	1	0	0	0
$\phi = -45^o; \theta = 45^o$	0	1	0	0	1	0	0	1	0	1	0	1	1
$\phi = -45^o; \theta = -45^o$	0	1	1	0	1	1	1	0	0	1	0	0	1

planes ($\phi \in -45^o, 0^o, 45^o, 90^o$) is shown in Figures 6.14, 6.15, 6.16, and 6.17.

In Figures 6.10 - 6.17, the result corresponding to $\theta = 0^o$ direction refers to the broadside mode of operation. As it is shown, the tilt behavior in $\phi = 0^o(xz)$ plane is not good when compared to the other planes. The reason being, the bias lines of the MRA which are along the x-direction (see Figure 6.3), restrict the maximum tilt direction to 30^o as opposed to 45^o in other planes. Realized gains in all the directions are in the range of 4-6 dB.

The measurement results showing the reflection coefficient of the nine modes of 4.9 GHz MRA is shown in Figures 6.18, 6.19, 6.20, and 6.21.

As the simulations were not accurately modeling the measurements, the problem in the simulation model needs to be identified. The first suspicion was on the value of parasitic capacitances used for lumped RF chokes (= 8.7 nH on bias line) and the parallel inductors (= 1.8 nH besides switch). The previously used values are given in Table 6.3 with their corresponding Self Resonant Frequencies (SRF). These SRFs were obtained from

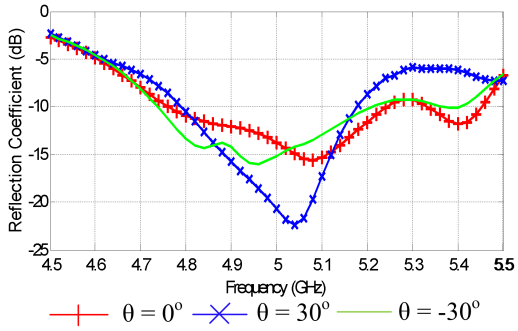

Fig. 6.10: The simulated reflection coefficient of the MRA in $\phi = 0^o$ (xz) plane.

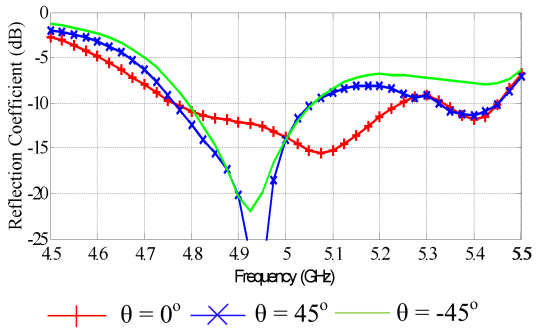

Fig. 6.11: The simulated reflection coefficient of the MRA in $\phi = 45^o$ plane.

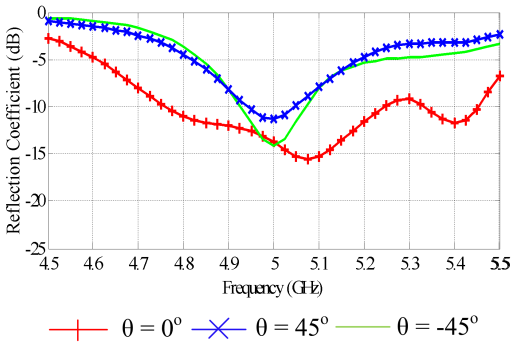

Fig. 6.12: The simulated reflection coefficient of the MRA in $\phi = 90^o$ (yz) plane.

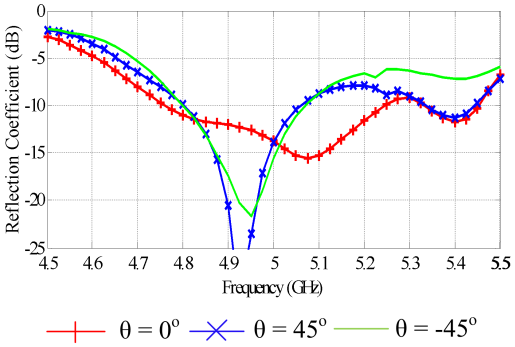

Fig. 6.13: The simulated reflection coefficient of the MRA in $\phi = -45^o$ plane.

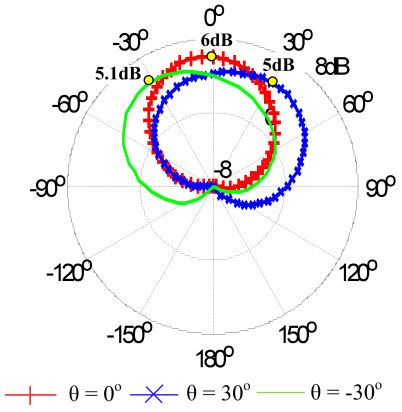

Fig. 6.14: The simulated total gain plot (in dB) of the MRA at 4.94 GHz in $\phi = 0^o$ (xz) plane.

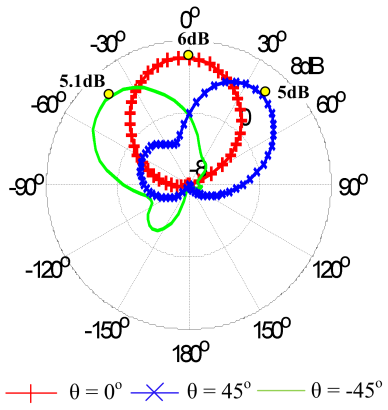

Fig. 6.15: The simulated total gain plot (in dB) of the MRA at 4.94 GHz in $\phi = 45^o$ plane.

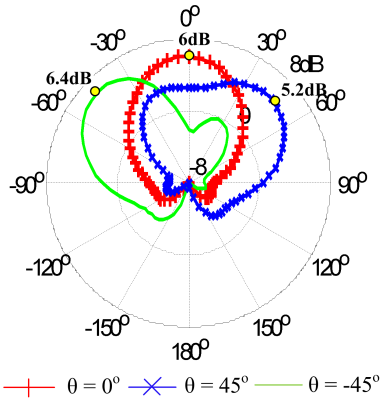

Fig. 6.16: The simulated total gain plot (in dB) of the MRA at 4.94 GHz in $\phi = 90^o$ (yz) plane.

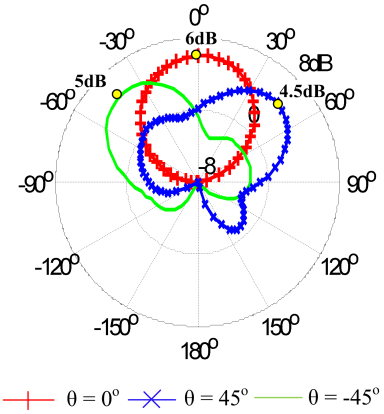

Fig. 6.17: The simulated total gain plot (in dB) of the MRA at 4.94 GHz in $\phi = -45^o$ plane.

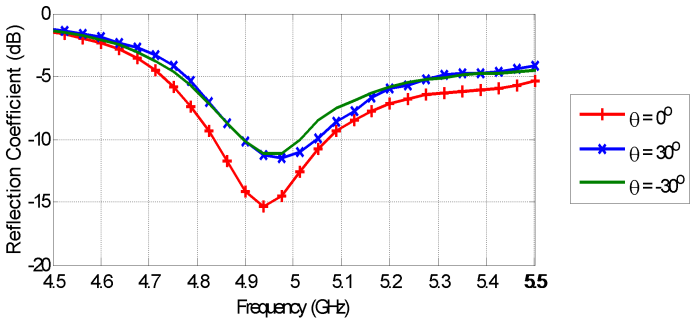

Fig. 6.18: The measured reflection coefficient of the MRA in $\phi = 0^o$ (xz) plane.

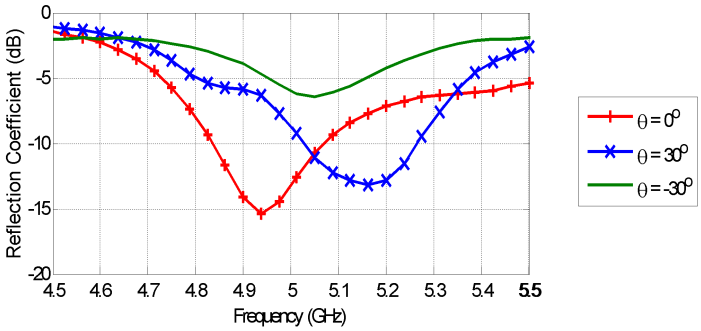

Fig. 6.19: The measured reflection coefficient of the MRA in $\phi = 45^o$ plane.

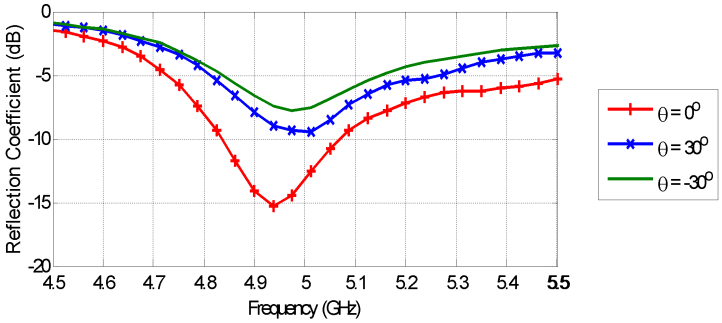

Fig. 6.20: The measured reflection coefficient of the MRA in $\phi = 90^o$ (yz) plane.

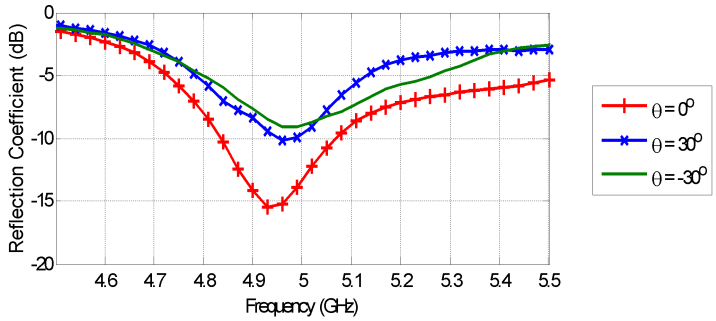

Fig. 6.21: The measured reflection coefficient of the MRA in ϕ = -45^o plane.

the datasheets of the components (SRF1). It seems that the value of SRF specified in the datasheet deviates a lot from the actual value which is obtained by looking at the S parameters of the de-embedded devices (SRF2). These revised values are also provided in Table 6.3.

The DC block capacitance was previously modeled as a series RLC circuit in HFSS. Simulations in HFSS suggested that, the resistance and inductance of RLC circuit along with the lead inductance of the pin-diode are responsible for increasing the BW in simulation, whereas the obtained BW in measurement was low. After removing these lumped components from DC bock and pin-diodes and changing the parasitic capacitances (of SMD inductors) the following fit between simulations and measurements is obtained as shown in Figures 6.22 - 6.30 which is acceptable for practical purposes.

The tilt behavior corresponding to the previously provided switch configurations for all modes of operation is lost when the changes described above were introduced in simulation in order to predict the measurement better. Also significant gain reduction was observed. The completed parasitic pixel layer prototype (which was used in the measurement in Figures

Table 6.3: Using different sources to calculate the parasitic capacitance (C_{par}) of the parallel inductor and RF choke on bias line.

Inductor	*SRF1*	C_{par} *using SRF1*	*SRF2*	C_{par} *using SRF2*
1.8 nH	16 GHz	0.055pF	25 GHz	0.02pF
8.7 nH	5.5 GHz	0.096pF	8.1 GHz	0.038pF

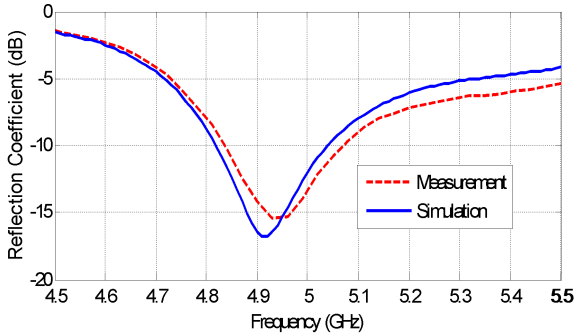

Fig. 6.22: The simulated and measured reflection coefficient of the MRA in $\theta = 0^o$ direction of $\phi = 0^o$ (xz) plane.

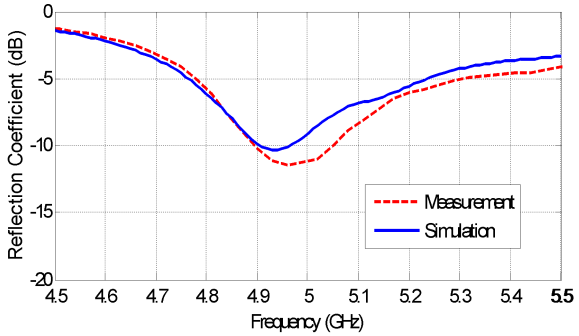

Fig. 6.23: The simulated and measured reflection coefficient of the MRA in $\theta = 30^o$ direction of $\phi = 0^o$ (xz) plane.

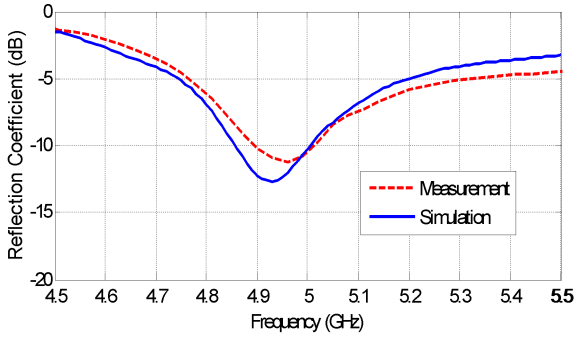

Fig. 6.24: The simulated and measured reflection coefficient of the MRA in $\theta = -30^o$ direction of $\phi = 0^o$ (xz) plane.

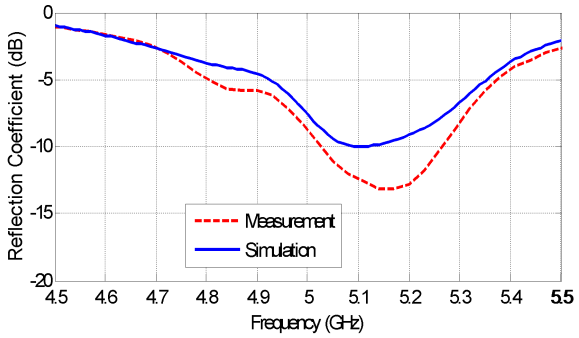

Fig. 6.25: The simulated and measured reflection coefficient of the MRA in $\theta = 30^o$ direction of $\phi = 90^o$ (yz) plane.

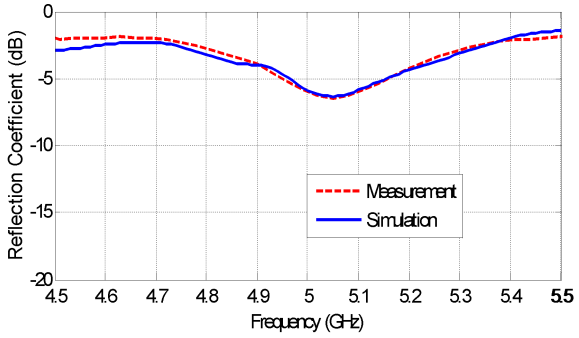

Fig. 6.26: The simulated and measured reflection coefficient of the MRA in $\theta = -30^o$ direction of $\phi = 90^o$ (yz) plane.

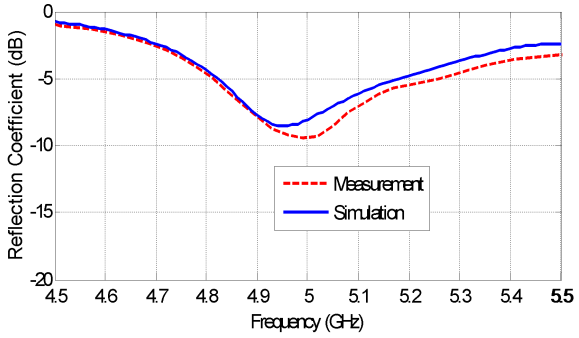

Fig. 6.27: The simulated and measured reflection coefficient of the MRA in $\theta = 30^o$ direction of $\phi = 45^o$ plane.

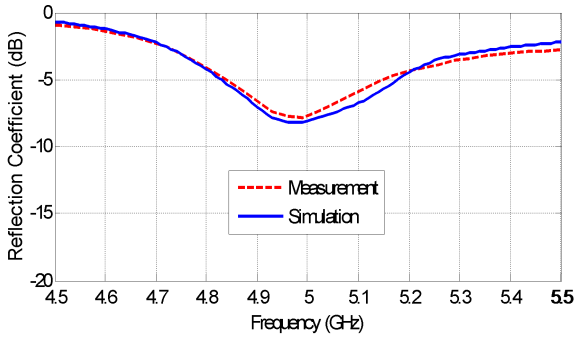

Fig. 6.28: The simulated and measured reflection coefficient of the MRA in $\theta = -30^o$ direction of $\phi = 45^o$ plane.

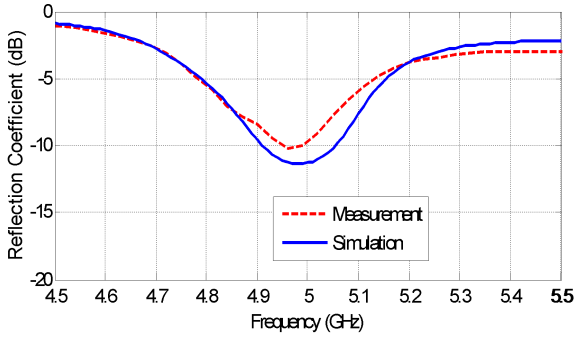

Fig. 6.29: The simulated and measured reflection coefficient of the MRA in $\theta = 30^o$ direction of $\phi = -45^o$ plane.

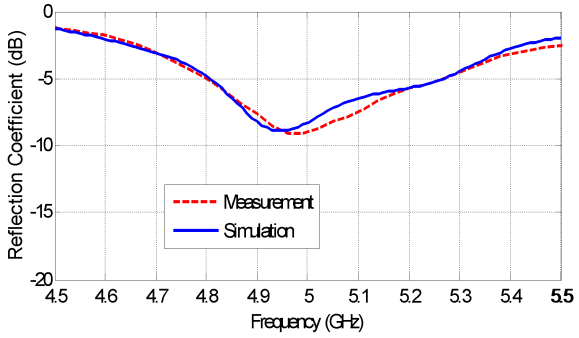

Fig. 6.30: The simulated and measured reflection coefficient of the MRA in $\theta = -30^o$ direction of $\phi = -45^o$ plane.

6.22 - 6.30) was employed in an MRA model in which the RO4003C substrate was entirely replaced by air in order to enhance the gain. Before starting a GA on top of this model, the patch dimensions and the height of the air layer were optimized along with the location of the coaxial cable to result in the model shown in Figure 6.31.

The corresponding optimized switch configurations obtained by running GA on the optimized model are given in Table 6.4.

The fabricated and assembled MRA prototype with all components soldered for reconfigurability is shown in Figure 6.32.

In Figures 6.33, 6.34, 6.35, 6.36, and 6.37, the simulated and measured reflection coefficient results of the MRA for nine different modes of operation, with good agreement between them, are shown. The simulated total gain plots (in dB) of the MRA showing tilted beams in four principal planes ($\phi \in -45^o, 0^o, 45^o, 90^o$) are shown in Figures 6.38, 6.39, 6.40, and 6.41.

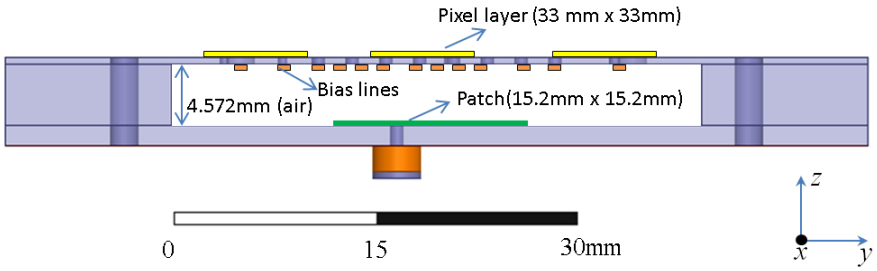

Fig. 6.31: Cross-section view of the optimized 4.9 GHz MRA model.

Table 6.4: Switch configurations of the antenna obtained from GA to result in nine different beam directions (0 and 1 correspond to OFF and ON states, respectively).

Switch number	*0*	*1*	*2*	*3*	*4*	*5*	*6*	*7*	*8*	*9*	*10*	*11*	*12*
$\phi = 0^o; \theta = 0^o$	0	0	0	0	0	0	0	0	0	0	0	0	0
$\phi = 0^o; \theta = 30^o$	0	0	1	0	1	0	0	0	1	0	0	0	0
$\phi = 0^o; \theta = -30^o$	0	1	0	0	1	1	1	1	0	0	0	0	1
$\phi = 90^o; \theta = 30^o$	0	0	1	0	1	0	1	1	1	1	1	0	0
$\phi = 90^o; \theta = -30^o$	0	0	1	1	0	1	0	1	1	1	0	0	1
$\phi = 45^o; \theta = 30^o$	0	0	1	0	0	0	1	0	1	0	1	0	1
$\phi = 45^o; \theta = -30^o$	0	1	0	1	0	1	0	1	0	0	0	1	0
$\phi = -45^o; \theta = 30^o$	0	1	0	0	1	1	0	0	0	1	1	1	0
$\phi = -45^o; \theta = -30^o$	0	1	0	1	1	1	0	0	1	0	0	0	0

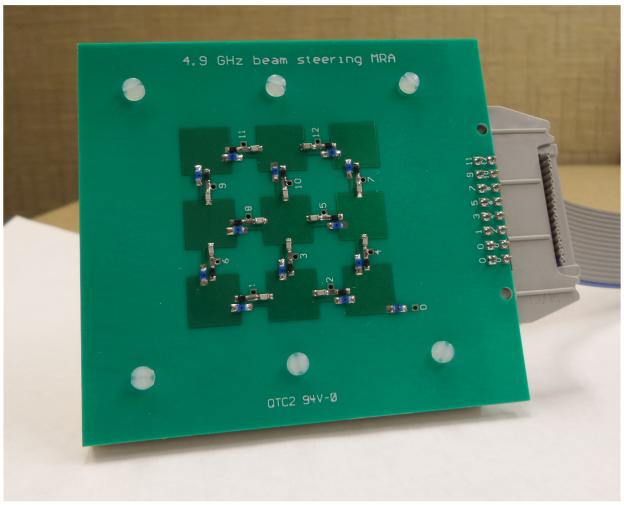

(a)

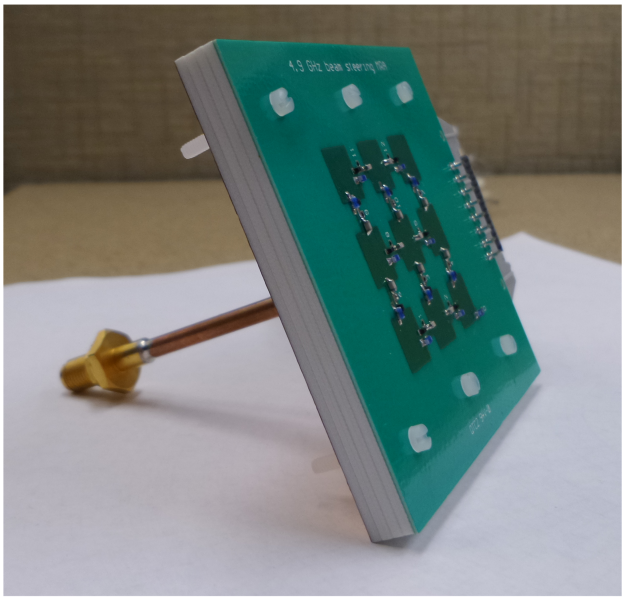

(b)

Fig. 6.32: Photographs of the fabricated and assembled MRA showing (a) top, and (b) side views.

6.3 Future Work

The radiation pattern characterization of the MRA is pending.

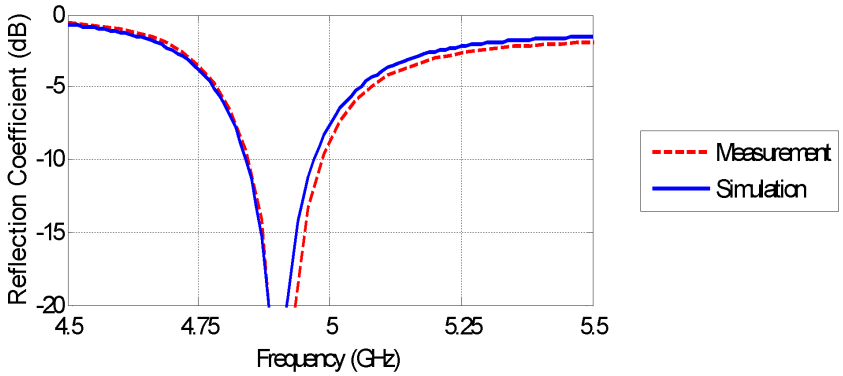

Fig. 6.33: The simulated and measured reflection coefficient of the MRA in broadside operation.

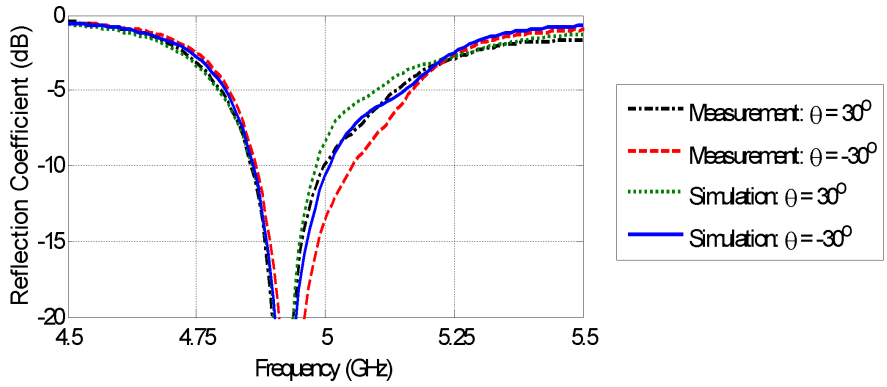

Fig. 6.34: The simulated and measured reflection coefficient of the MRA in $\phi = 0^o$ (xz) plane.

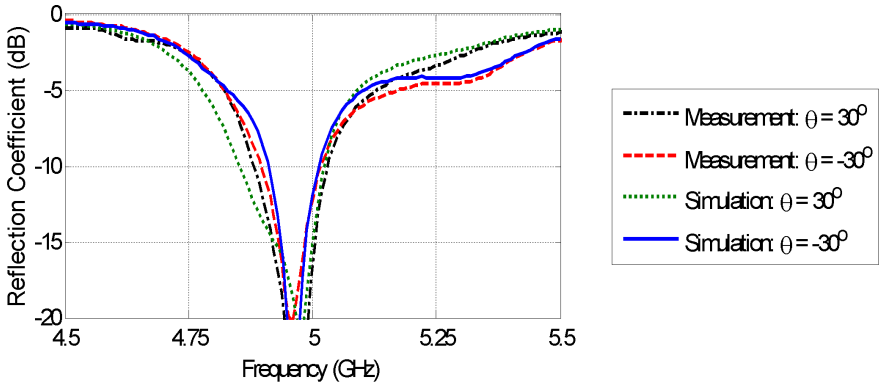

Fig. 6.35: The simulated and measured reflection coefficient of the MRA in $\phi = 45^o$ plane.

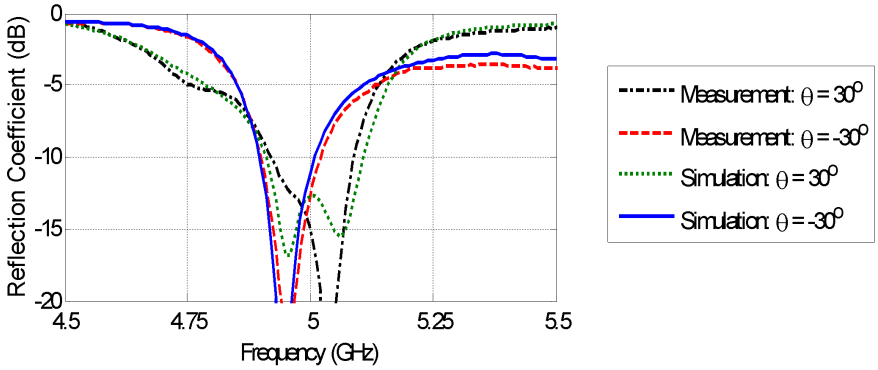

Fig. 6.36: The simulated and measured reflection coefficient of the MRA in $\phi = 90^o$ (yz) plane.

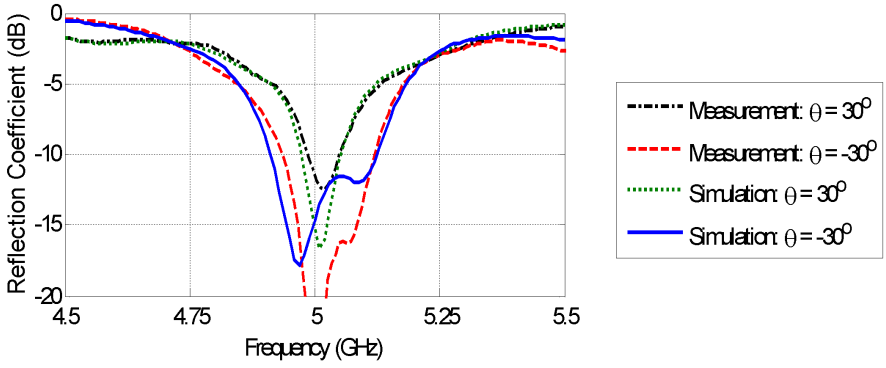

Fig. 6.37: The simulated and measured reflection coefficient of the MRA in $\phi = $ -45^o plane.

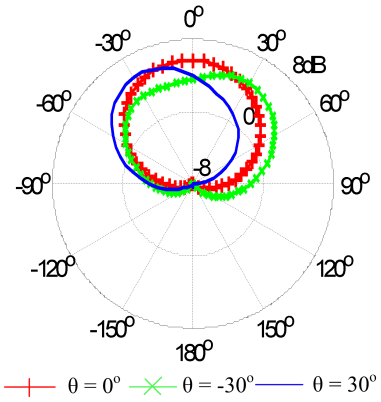

Fig. 6.38: The simulated total gain plot (in dB) of the MRA at 4.94 GHz in $\phi = 0^o$ (xz) plane.

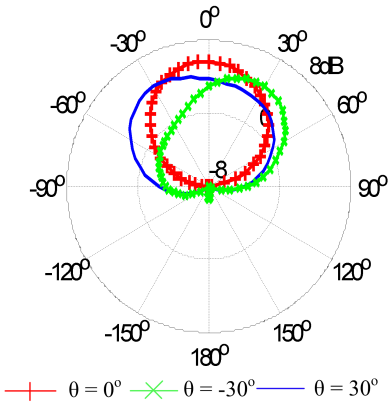

Fig. 6.39: The simulated total gain plot (in dB) of the MRA at 4.94 GHz in $\phi = 45^o$ plane.

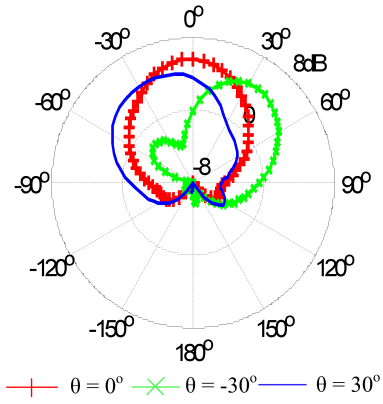

Fig. 6.40: The simulated total gain plot (in dB) of the MRA at 4.94 GHz in $\phi = 90^o$ (yz) plane.

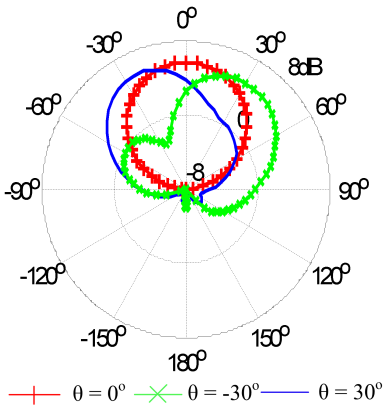

Fig. 6.41: The simulated total gain plot (in dB) of the MRA at 4.94 GHz in ϕ = -45^o plane.

Chapter 7

3-D Micro-Fabricated Broadband Patch Antenna for WiGig Applications

7.1 Introduction

Among the printed antennas, patch antennas allow for easier integration with RF-front end systems due to their compatibility with microwave integrated circuits. To enhance the BW of CPW fed patches with omni-directional radiation, a coplanar waveguide (CPW)-fed slot coupled patch approach is employed in Lu et al. [61]. To obtain a directional radiation pattern, a conductor backing is used for a CPW-fed slot antenna in Liu et al. [62]. Combining these two techniques, a conductor backed (CB) CPW-fed loop slot (formed on quartz substrate) sourcing a micro-fabricated patch antenna on 3-D thick structural SU-8 layers is presented in this work. This BW enhancement technique, which utilizes the quartz substrate for the loop metallization, is advantageous in simplifying the overall antenna architecture when compared to the stacked patch design [63], as the latter technique would need an additional layer for the stacked patch. The antenna design, in this work, is carried out in conjunction with micro-fabrication process compatibility and mechanical integrity of the 3-D structure. The developed SU-8 based micro-fabrication process presented in this work can also be applied to reconfigurable antenna technologies for the next generation WiGig systems.

7.2 Antenna Design

The antenna as depicted in Figures 7.1 and 7.2, is a CPW-fed broadband patch antenna micro-fabricated on an RF compatible quartz substrate ($\epsilon_r = 3.9$, $tan\delta = 0.0002$ at 60 GHz). The feed metallization, which consists of a 50 ΩCB CPW, along with the loop is formed on a 525 μm thick quartz substrate. The SU-8 based 3-D substrate is micro-fabricated on

top of the feed metallization as described in Section 7.3. The 3-D substrate consists of an SU-8 membrane which is supported via SU-8 posts. The patch antenna metallization is finally formed on this 3-D substrate. The location of SU-8 posts and the thickness of SU-8 membrane (S_t) dictate the mechanical stability of the 3-D antenna. As SU-8 is quite lossy, an intelligent design trade-off between the mechanical integrity of the 3-D structure and the performance of the antenna needs to be incorporated. Accordingly, air cavities are incorporated in the 3-D SU-8 substrate to reduce the dielectric loss which would in turn enhance the performance of the antenna. The height of the air cavity (A_t), which is also the height of SU-8 posts, has an effect on the impedance BW and realized gain of the antenna.

To enhance the BW of patch antenna a CB CPW-fed rectangular loop slot (with dimensions L_l, L_w, and L_t) couples the energy to the patch antenna. The resonant length of the loop is calculated as

$$L_l + L_w/2 \sim \lambda/g/2, \tag{7.1}$$

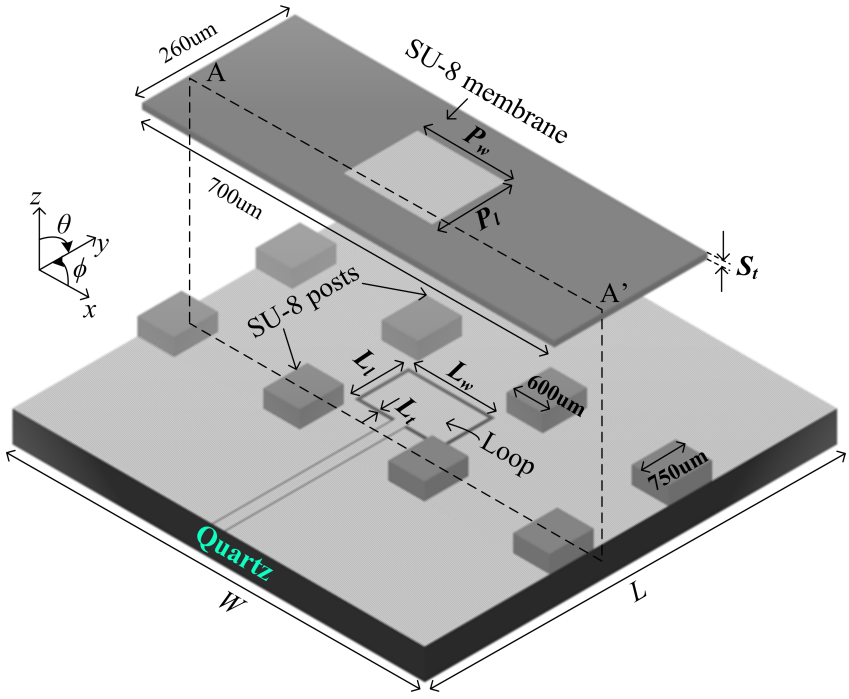

Fig. 7.1: Schematic depicting 3-D drawing of the antenna (For the sake of illustration, the SU-8 membrane is suspended on top of the CPW metallization).

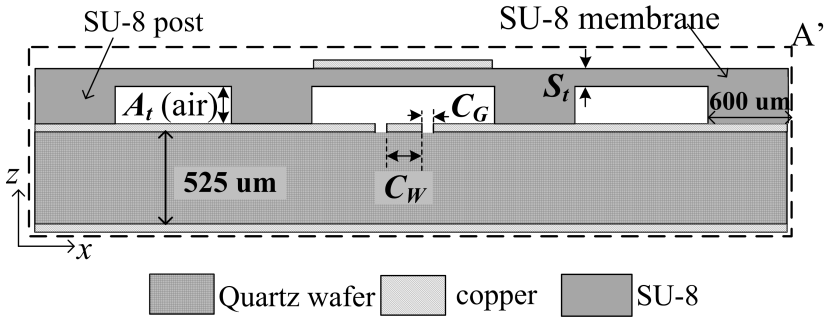

Fig. 7.2: Schematic depicting crosssectional drawing of the antenna.

where λ/g is the guide wavelength in quartz substrate at the resonant frequency (f_s). The substrate thickness of CB CPW fed loop slot plays an important role in broadening the radiation BW of the antenna. One of the main contributions of this work is not only to improve the antenna performances in the WiGig band but also to make the antenna design compatible with micro-fabrication processes, resulting in efficient and economic fabrication. Therefore, a 525μm thick quartz substrate, which is micro-fabrication friendly as well as electrically thick to aid in broadband WiGig communication, is chosen. The patch antenna dimensions are calculated using the following equations [64]:

$$P_l \sim \frac{c}{2f_p\sqrt{\epsilon_r}}, \tag{7.2}$$

$$P_l < P_w < 2P_l, \tag{7.3}$$

where c is the speed of light; f_p is the resonant frequency, and ϵ_r is the effective dielectric constant. The initial dual band response of the loop slot coupled patch antenna is shown in Figure 7.3, where the resonances at $f_p = 62.5$ GHz and $f_s = 77$ GHz correspond to patch and loop slots, respectively, according to Eqs. (7.1), (7.2), and (7.3). The parameters of CB CPW-fed loop and patch along with those of 3-D SU-8 substrate are jointly optimized to combine the patch and loop resonances resulting in a broader BW. Also, the standard thickness of the micro-fabrication compatible quartz wafer (525 μm) is incorporated into the design optimization to attenuate possible surface waves. The height (A_t) and lateral area (2.6 x 2.6mm^2 - 4 x 0.75 x 0.6 mm^2= 4.96mm^2) of air cavity beneath the patch, which

suppresses the surface waves [30] and broadens the BW, can be precisely controlled within the realm of micro-fabrication feasibility using custom made SU-8 3-D architectures. This methodology, taking the advantage of monolithically micro-fabricated 3-D structures, provides greater design flexibility and cost reduction when compared to etching away portions of bulky substrates or creating vias/holes in substrates with standard thickness [29, 30].

The optimized design parameters of the patch element, CPW-fed loop, and the 3-D substrate obtained from full-wave simulation are provided in Table 7.1. Using these optimized parameters and Eq. (7.2), the effective dielectric constant (ϵ_r) of the SU-8 based 3-D structure including quartz wafer is verified to be ∼3.8 which is in between that of quartz (ϵ_r=3.9) and SU-8 (ϵ_r∼3.1). This design methodology not only minimizes the dielectric loss of SU-8 through air cavities, but also results in compact antenna size due to higher effective dielectric constant. Secondly, the patch metallization on top of the SU-8 substrate focuses the EM energy to result in a narrower beamwidth which is otherwise broader for a standard CPW-fed loop. Finally, the patch metallization also decreases the cross polarization level to at-least 16 dB (as opposed to ∼9dB in standard CPW-fed loop) below the co-polarization level of the presented antenna as shown in Section 7.4.

7.3 Micro-Fabrication

A 4-mask level, microwave-compatible micro-fabrication process is developed utilizing 3-D thick SU-8 coating & patterning processes as well as standard thin-film deposition and

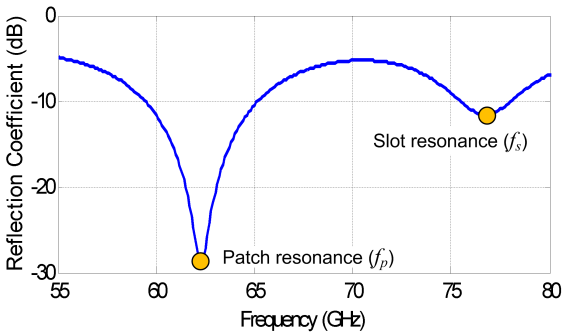

Fig. 7.3: Initial dual band response of CB CPW fed slot loop coupled patch antenna with slot and patch resonances separated prior to design optimization.

Table 7.1: The critical design parameters of the 3-D WiGig antenna (all dimensions are in mm).

Parameter	*Value*	*Parameter*	*Value*	*Parameter*	*Value*	*Parameter*	*Value*
W	7	P_w	1.5	L_l	0.92	C_G	0.02
L	7	P_l	1.25	L_w	1.47	C_W	0.191
L_t	0.06	S_t	0.1	A_t	0.2		

patterning/etching processes. Prior to fabrication, 4-inch RF-compatible/low-loss quartz substrates ($\epsilon_r = 3.9$, $tan\delta = 0.0002$ at 60 GHz) were cleaned using standard acid/solvent cleaning, DI-water rinsing, nitrogen-blow drying, and de-hydration baking on a 120^{o}C hot-plate.

As summarized schematically in Figure 7.4, the fabrication process started with physical vapor deposition (PVD) and patterning of the CPW metal layer which was formed of Titanium/Copper (Ti/Cu) where Ti functioned as the 10 nm thick adhesion layer and Cu thickness was ∼300 nm (see Figure 7.4(a)). Sputtering and thermal evaporation were the most dominantly used PVD methods, whereas the patterning was realized using either a lift-off or wet metal-etch process. After the metallic CPW was formed, blank Ti/Cu deposition on the backside of quartz wafer was implemented which functioned as the ground metal layer (see Figure 7.4(b)). Later SU-8 coating and patterning process consisting of two mask layers was carried out (see Figure 7.4(c)). A 300 μm-thick SU-8 layer was reached using two consecutive spin coating of 150 μm layers and soft-baked at 95^{o}C for 45 and 90 minutes after each layer deposition, which was followed by two separate exposures. The first (second in the overall process) mask was used to cross-link the post regions for a total dose of 300 mJ/cm^2. A lower exposure dose (95 mJ/cm^2) was used in the second (third mask in the overall process) mask with the aim of cross-linking only the 100 μm upper layer of the membrane areas. Immediately after the exposure steps, a 3-min post-exposure bake (PEB) at 55^{o}C was applied with sufficient ramp-up and ramp-down durations to minimize the stress accumulation within the structural SU-8 layers. Patch metal deposition and patterning followed using ∼300 nm-thick Ti/Cu DC-sputtering and wet-etch patterning using the fourth lithography mask (see Figure 7.4(d)). Finally, the sample is soaked

into SU-8 developer solution within an ultrasonic bath, targeting to dissolve and remove the uncross-linked SU-8 layer underneath the partially exposed membrane (see Figure 7.4(e)).

Agitated development process for 7-8 min was enough to completely remove the unprocessed SU-8 material and the membranes were released successfully. The micro-fabrication process of our 3-D WiGig antenna was completed with a hard baking process of the device over a hot plate at 110 ^{o}C to strengthen the structure by further crosslinking the SU-8 layers. Figure 7.5 shows a scanning electron microscope (SEM) picture of a completed device.

7.4 Measurements and Characterization

The performance of the micro-fabricated loop-coupled patch antenna with CPW feed has been measured with an Agilent 8510C vector network analyzer (VNA) together with a GSG-probe station from 55 to 70 GHz.

The pitch of the probes (distance between one ground tip and the signal tip) is of 150 μm. The CPW feeding lines of the patch antenna were designed to perfectly accommodate to this probe pitch. One port calibration process was performed manually measuring three known standards (i.e., open, short, and broadband matched load terminations) in order to establish the measurement reference planes. The wafer with the micro-fabricated patch antenna prototypes was placed over the sample stage.

Since the antenna was designed with a CB CPW feed, the effect of the metal plate of sample stage in the measurement setup has been minimized. The sample stage has a movable metal plate that allows probes to contact anywhere on the wafer surface with precise motion in a 2-D plane (x-y directions). The stage is equipped with a vacuum chuck to fix the wafer to the metal plate, with the aim to ensure the perfect contact of the probe tips with the CPW feeding the patch antenna. A PC communicates with VNA in order to control the process, run the calibration software and store the measurements.

The simulated and measured reflection coefficients, with good agreement between them, are plotted in Figure 7.6, for a frequency range from 57 to 67 GHz. Slight variation between measured and simulated results can mainly be attributed to the fabrication tolerances. The

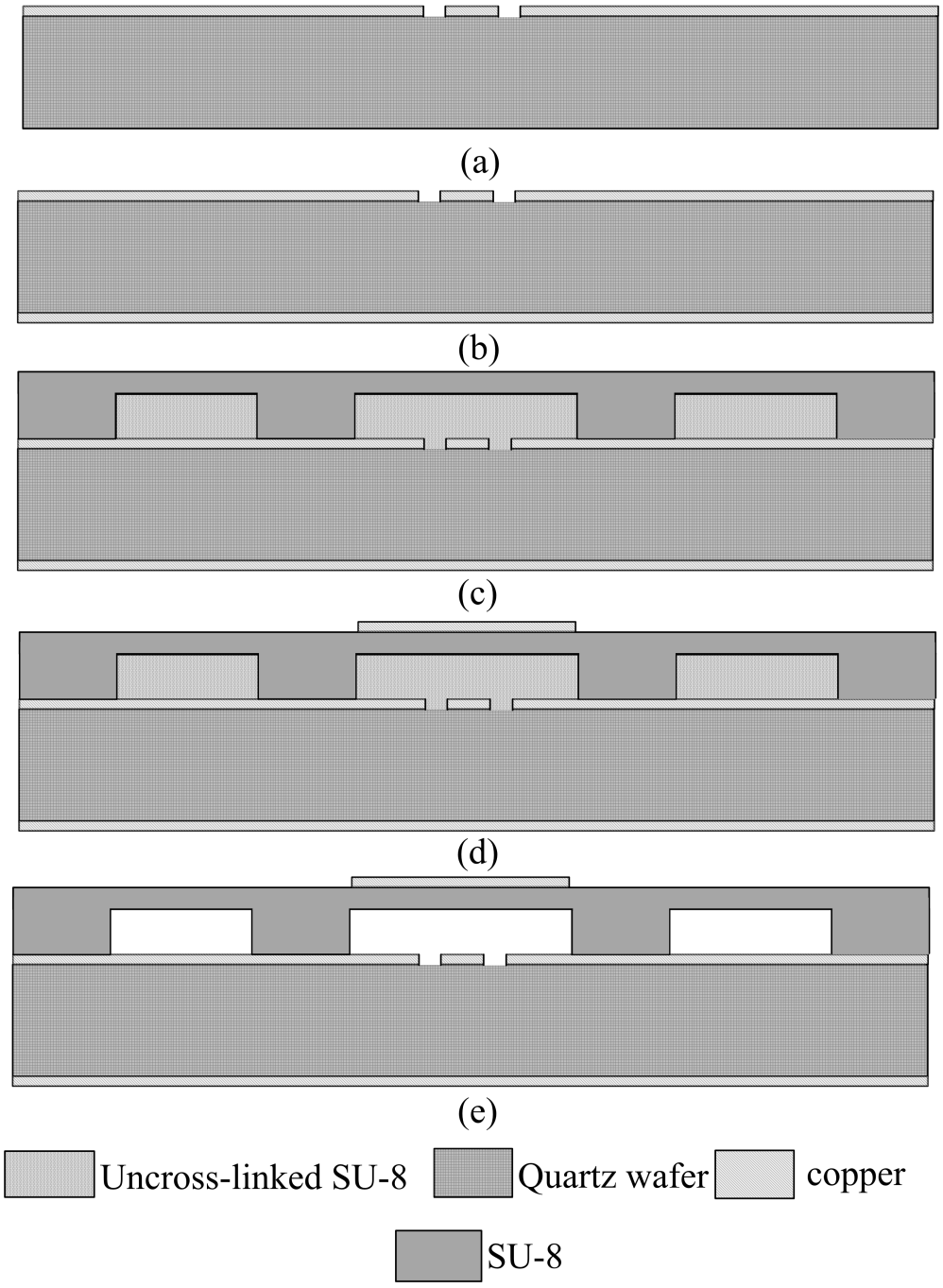

Fig. 7.4: (a-e)Cross-sectional schematic representation of the four-mask level SU- 8-based 3-D micro-fabrication process flow.

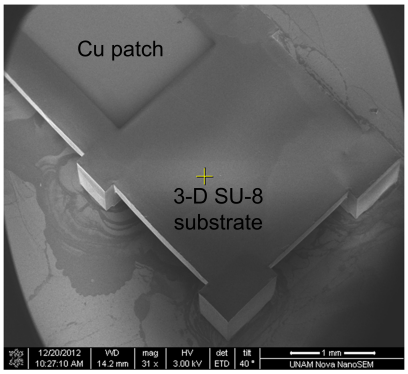

Fig. 7.5: Angled-view SEM micrograph of a completed antenna device with SU-8 posts and fully-released SU-8 membrane along with patterned Cu patch metal layer on top.

reflection coefficient shows that the antenna has a 2:1 VSWR BW of greater than 9 GHz ($\sim$ 15% of fractional BW), which covers the entire frequency range of the IEEE 802.11ad (57-66 GHz). The simulated radiation patterns of the linearly polarized antenna in xz plane at 57 GHz and 66 GHz are shown in Figures 7.7(a) and 7.7(b), respectively, showing a patch type pattern, as expected (at the time of this work, we did not have the capability of performing radiation pattern measurements at 60 GHz). The cross polarization level is at-least 16 dB below the co-polarization level of the antenna. The realized maximum gain of the antenna is relatively constant and is in the range $\sim$5.5 to 7 dB over the entire BW as shown in Figure 7.8. Higher gain is obtained due to the presence of air cavities in the 3-D SU-8 substrate, which effectively reduces the dielectric loss.

7.5 Conclusion

A CPW-fed broadband patch antenna compatible with IEEE 802.11ad standard (WiGig) is designed, micro-fabricated, and characterized. The measured reflection coefficient data is in good agreement with the simulation giving $\sim$ 15% BW. The simulated radiation patterns with reasonably constant gain values (5.5 to 7 dB) in the broadside direction over the entire WiGig band (57 to 66 GHz) indicate a design with low dielectric loss. The SU-8 based 3-D micro-fabrication processes developed for this antenna structure provides an important advantage for custom made reconfigurable antennas which might also be greatly useful in WiGig applications.

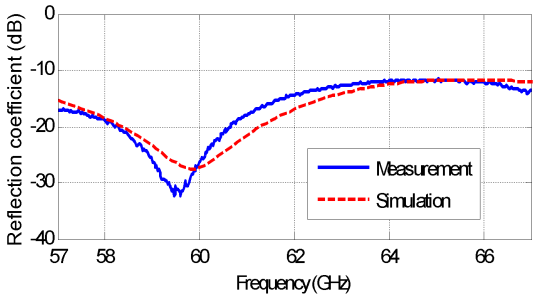

Fig. 7.6: Simulated and measured magnitudes of S11 parameter (reflection coefficient) for a frequency range from 57 to 67 GHz obtained for the micro-fabricated broadband patch antenna.

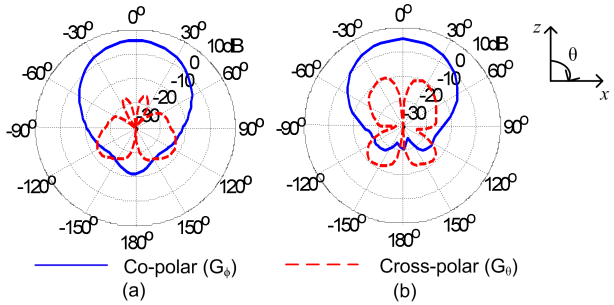

Fig. 7.7: Simulated realized gain plot (dB) of the antenna in xz plane at (a) 57 GHz, and (b) 66 GHz.

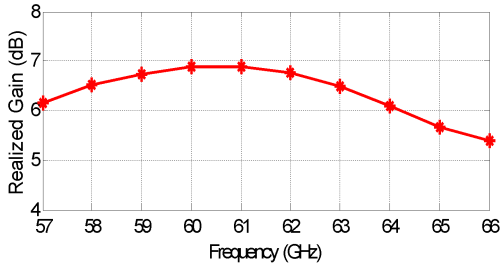

Fig. 7.8: Simulated realized gain (dB) in the broadside direction of the antenna with respect to frequency.

Chapter 8

Broadband Beam-Steering MRA and MRAA for WiGig Applications

8.1 MRA Structure and Working Mechanism

The antenna depicted in Figures 8.1 and 8.2 is a parasitic layer-based MRA utilizing a 3-D SU-8 layer for increased antenna performances. The conductor backed CPW metallization on 525μm thick Quartz substrate feeds a loop slot ($L_l \times L_w$) which in-turn couples EM energy to the patch metallization ($P_l \times P_w$). This patch metallization is deposited on top of another 260 μm thick Quartz substrate. The centers of patch and loop slot metallizations should lie on a straight line pointing in $\theta = 0^o$ (z)-direction for broad-side radiation. The loop slot coupled patch antenna forms the driven antenna element and the beam steering is accomplished by a reconfigurable parasitic layer formed on a 3-D SU-8 substrate. The 3-D SU-8 substrate with air-cavities is carefully engineered to provide sufficient mechanical robustness as well as enhanced antenna performances. The volume occupied by air-cavities ($\sim$ 4mm $\times$ 4mm $\times$ $A_t$mm - 4 $\times$ 0.6mm $\times$ 0.6mm $\times$ A_t) is carefully optimized by controlling the SU-8 membrane thickness (S_t) along with the location and area occupied by SU-8 posts. Micro-fabrication feasibility must also be taken into account while satisfying the other requirements. Hence, the design methodology of this MRA at 60 GHz taking into account ease of micro-fabrication, mechanical robustness, and enhanced antenna performances is quite different from conventional antenna design methodologies.

The reconfigurable parasitic layer consists of 3 x 3 metallic pixels ($Pi_l \times Pi_w$) with gaps ($G_l \times G_w$) between adjacent pixels. The interconnecting switches between adjacent pixels in this work are perfect open/short switches. In other words, the presence or absence of a short metallic strip (75μm $\times$ 100 μm) between adjacent pixels represents ON or OFF states

of switch, respectively. The driven antenna element design is quite similar to the antenna presented in Chapter 7. The main difference being, the 3-D SU-8 substrate for patch metallization has been replaced by a 260μm Quartz substrate to avoid the fabrication complexities of an antenna model employing double SU-8 structures - for the patch and reconfigurable parasitic layers. This resulted in reducing the impedance and radiation BW of the driven antenna from 57 - 66 GHz to 59 - 66 GHz. The overall pixel-area (taking into account the lateral pixel size and gap between adjacent pixels) and the height of the SU-8 membrane (A_t) are optimized to provide the following beam steering modes over 59 - 66 GHz band: $\theta \in \{-30^o, 0^o, 30^o\}$; $\phi \in \{-45^o, 0^o, 45^o, 90^o\}$. These nine beam directions are spread over four principal planes namely $\phi \in \{-45^o, 0^o, 45^o, 90^o\}$ as shown in Figure 8.3. The optimized parameters are provided in Table 8.1. L_1 is chosen to be less than L to facilitate the contact of measurement probes on CPW metallization.

The beam steering functionality of the parasitic layer can be explained as follows. Dynamic opening and closing of switches on the parasitic layer helps in forming directive and reflective slot configurations which effectively steer the beam into different directions. This mechanism is quite similar to the radiation from a printed Yagi-Uda antenna [65] which utilizes reflectors and directors. In essence, the reconfigurable parasitic layer can be thought of as a reconfigurable printed slot Yagi-Uda antenna.

8.2 MRA Results and Discussions

The top view of the 60 GHz MRA showing switch locations is depicted in Figure 8.4. Their statuses, which are determined by running a multi-objective genetic algorithm (GA) optimization [60] in conjunction with full-wave analysis, result in nine different beam directions pertaining to: $\theta \in -30^o, 0^o, 30^o; \phi \in -45^o, 0^o, 45^o, 90^o$ over 59 66 GHz band. The corresponding optimized switch configurations are given in Table 8.2.

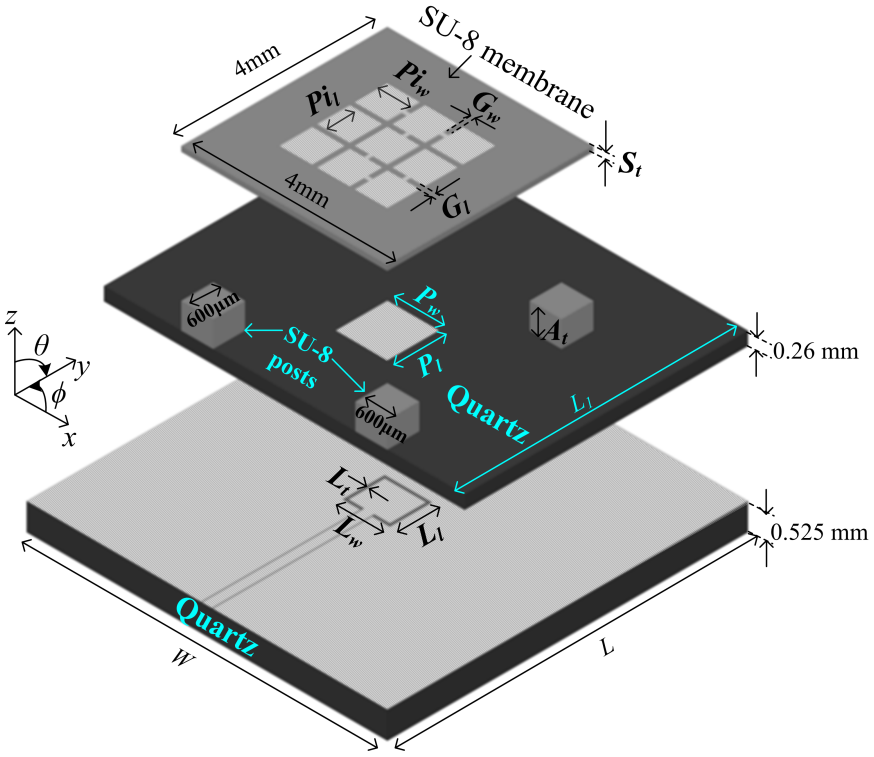

Fig. 8.1: Schematic depicting 3-D drawing of the 60 GHz MRA (For the sake of illustration, the SU-8 membrane is suspended on top of the patch metallization).

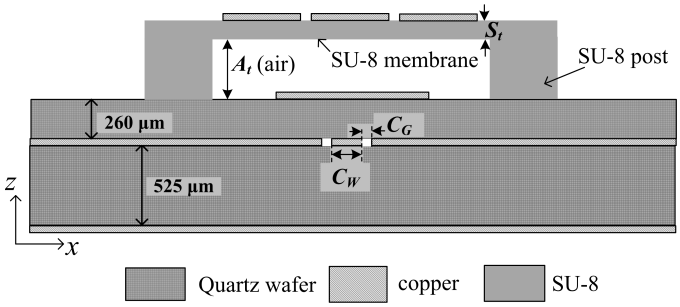

Fig. 8.2: Schematic depicting side-view of 60 GHz MRA.

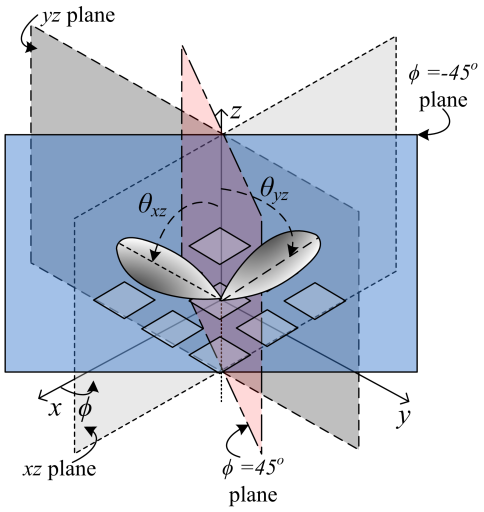

Fig. 8.3: Conceptual diagram showing the four principal planes: xz, yz, $\phi = 45^o$, and $\phi = -45^o$ planes with respect to a parasitic layer.

Table 8.1: The critical design parameters of the 60 GHz MRA (all dimensions are inmm).

Parameter	*Value*	*Parameter*	*Value*	*Parameter*	*Value*	*Parameter*	*Value*
Pi_l	0.63	Pi_w	0.63	G_l	0.1	G_w	0.1
W	7	P_w	1	L_l	0.82	C_G	0.02
L	7	P_l	1	L_w	0.92	C_W	0.191
L_t	0.06	S_t	0.1	A_t	0.4	L_1	5.5

The simulated reflection coefficients for all the nine modes of operation are given in Figures 8.5, 8.6, 8.7, and 8.8. The common BW in these figures indicates the frequency range over which the tilt behavior is maintained. The total realized gain (in dB) plots of the 60 GHz MRA in four principal planes at 62.5 GHz is shown in Figures 8.9, 8.10, 8.11, and 8.12. The realized gain values of all the nine directions over the entire 59 - 66 GHz band are in the range ∼5.5-7.5dB as shown in Figures 8.13, 8.14, 8.15, and 8.16.

8.3 2 x 1 MRAA Structure

The 2 x 1 MRAA designed for 60 GHz communications is shown in Figures 8.17 and 8.18. The MRAA structure consists of parasitic layer-based loop slot coupled patch antenna in a 2 x 1 linear array. The feed network consists of a 50 Ω CPW line which is divided into two 100 Ω lines to form a T-junction. These 100 Ω lines are converted to 50 Ω using $\lambda/4$

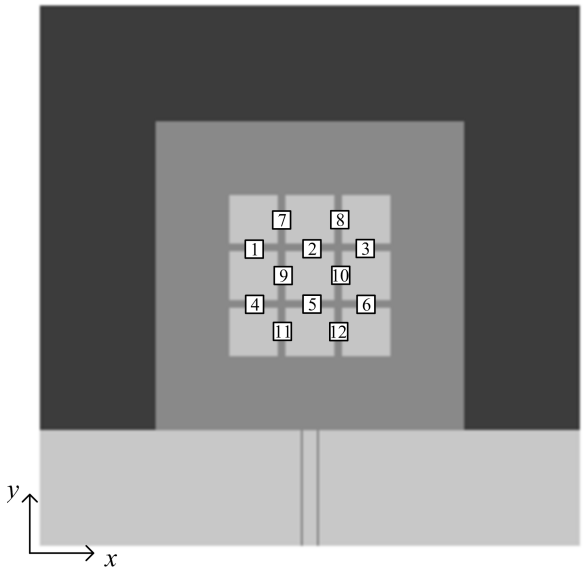

Fig. 8.4: Top view of MRA showing switch locations.

Table 8.2: Switch configurations of the 60 GHz MRA obtained from GA to result in nine different beam directions (0 and 1 correspond to OFF and ON states, respectively).

Switch number	*1*	*2*	*3*	*4*	*5*	*6*	*7*	*8*	*9*	*10*	*11*	*12*
$\phi = 0^o; \theta = 0^o$	0	0	0	0	0	0	0	0	0	0	0	0
$\phi = 0^o; \theta = 30^o$	0	1	0	0	0	1	1	0	1	0	1	0
$\phi = 0^o; \theta = -30^o$	0	1	0	1	0	0	0	1	0	1	0	1
$\phi = 90^o; \theta = 30^o$	1	1	0	1	0	1	1	0	1	1	1	1
$\phi = 90^o; \theta = -30^o$	1	0	1	1	1	0	1	1	1	1	1	0
$\phi = 45^o; \theta = 30^o$	0	1	1	0	0	1	1	0	1	0	0	1
$\phi = 45^o; \theta = -30^o$	0	0	1	1	1	1	0	0	0	1	1	0
$\phi = -45^o; \theta = 30^o$	1	0	0	0	0	0	0	1	0	1	1	0
$\phi = -45^o; \theta = -30^o$	0	1	0	0	1	0	1	1	0	0	0	1

transformers whose impedance is 70.7 Ω (see Figure 8.17). The two elements are separated by a distance (S_p) equal to $\lambda/2$ at 60 GHz, where λ is measured in free-space. The value of the parameters corresponding to patch, loop, parasitic pixel layer and 3-D SU-8 substrate of the MRAA are the as the 60 GHz MRA, hence, not repeated here.

The switch numbering followed in Figure 8.4 is also the same for MRAA. This design is capable of tilting the beam into $\theta \in -30^o, 0^o, 30^o$ in $\phi = 90^o$ (xz) plane without the use of phase-shifters as shown in the following section.

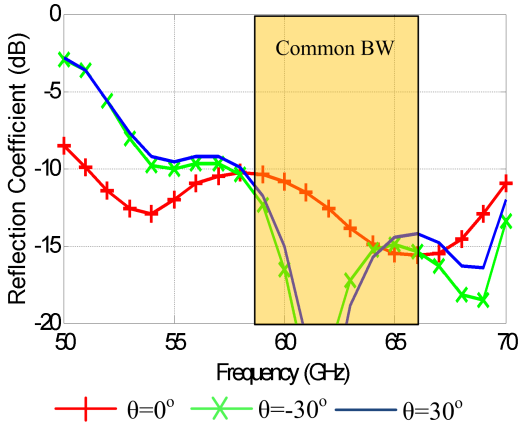

Fig. 8.5: The simulated reflection coefficient of the MRA in $\phi = 0^o$ (xz) plane.

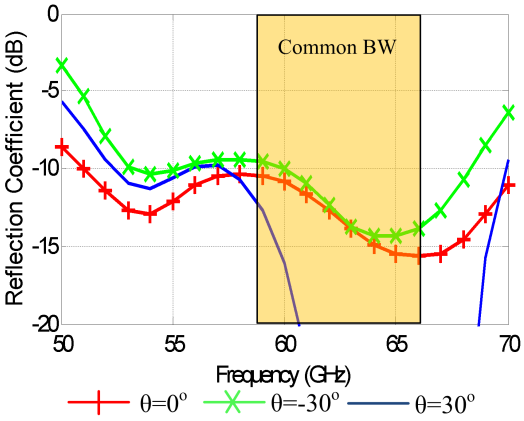

Fig. 8.6: The simulated reflection coefficient of the MRA in $\phi = 45^o$ plane.

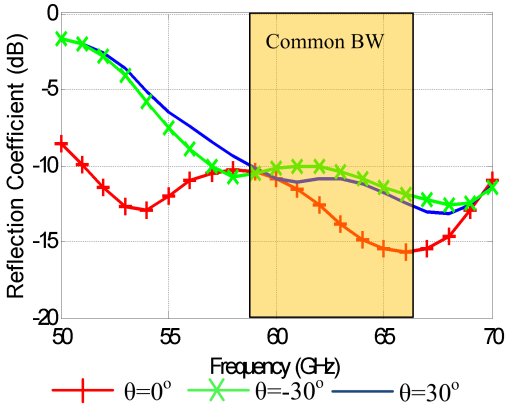

Fig. 8.7: The simulated reflection coefficient of the MRA in $\phi = 90^o$ (yz) plane.

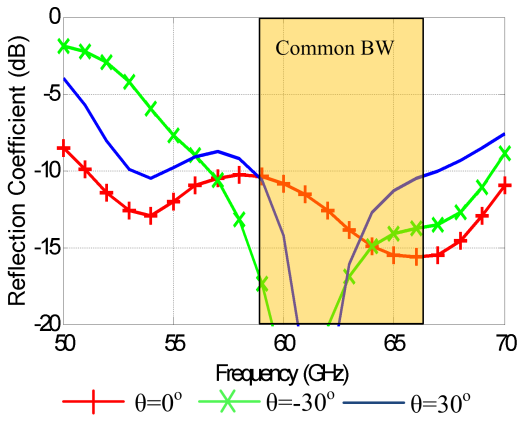

Fig. 8.8: The simulated reflection coefficient of the MRA in ϕ = -45^o plane.

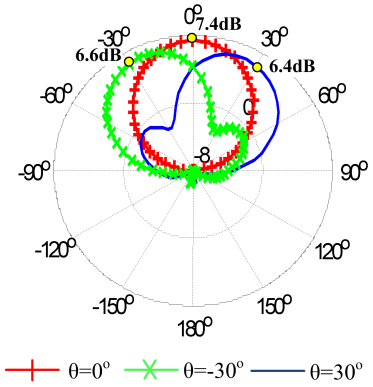

Fig. 8.9: The simulated total realized gain plot (in dB) of the MRA at 62.5 GHz in $\phi = 0^o$ (xz) plane.

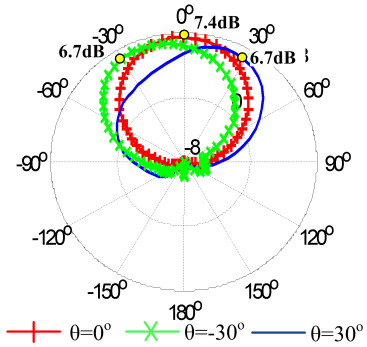

Fig. 8.10: The simulated total realized gain plot (in dB) of the MRA at 62.5 GHz in $\phi = 45^o$ plane.

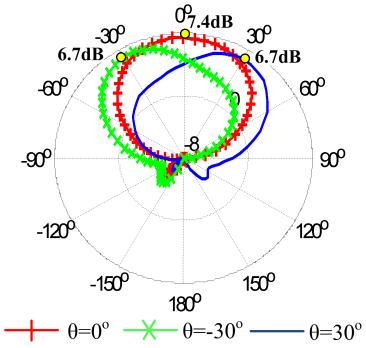

Fig. 8.11: The simulated total realized gain plot (in dB) of the MRA at 62.5 GHz in $\phi = 90^o$ (yz) plane.

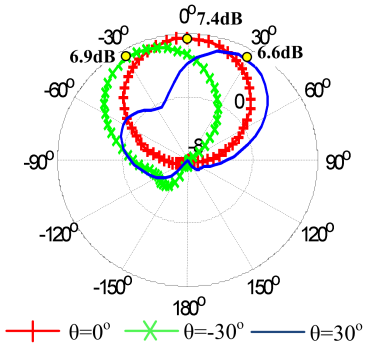

Fig. 8.12: The simulated total realized gain plot (in dB) of the MRA at 62.5 GHz in $\phi =$ -45^o plane.

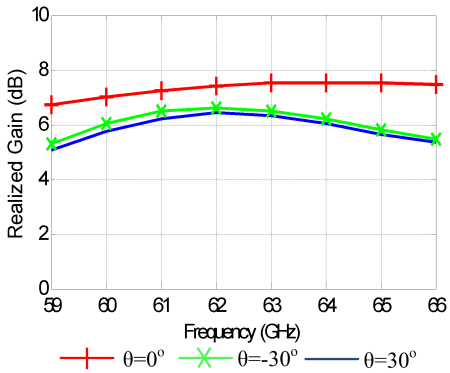

Fig. 8.13: The simulated realized gain values over 59-66 GHz band for three directions $\theta \in -30^o, 0^o, 30^o$ in $\phi = 0^o$ (xz) plane.

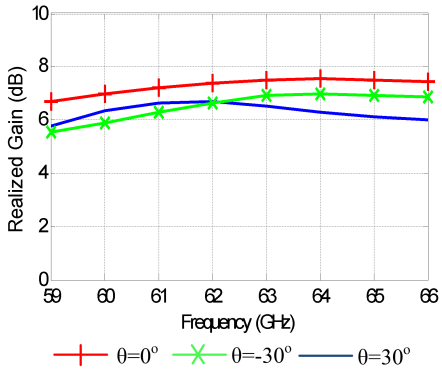

Fig. 8.14: The simulated realized gain values over 59-66 GHz band for three directions $\theta \in -30^o, 0^o, 30^o$ in $\phi = 45^o$ plane.

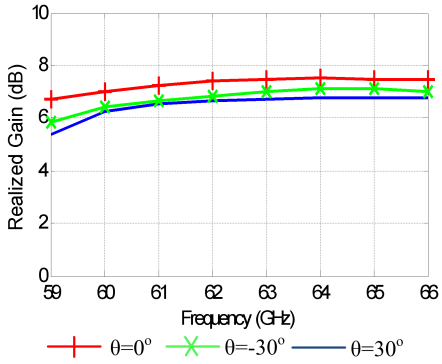

Fig. 8.15: The simulated realized gain values over 59-66 GHz band for three directions $\theta \in -30^o, 0^o, 30^o$ in $\phi = 90^o$ (yz) plane.

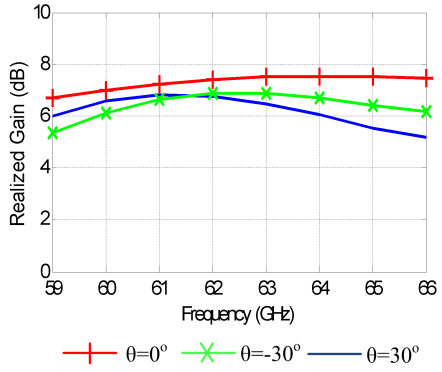

Fig. 8.16: The simulated realized gain values over 59-66 GHz band for three directions $\theta \in -30^o, 0^o, 30^o$ in $\phi =$ -45^o plane.

8.4 MRAA Results and Discussions

The optimized switch configurations corresponding to three modes of operation are given in Table 8.3. The reflection coefficient plots of the MRAA showing tilt modes in ϕ=90^o (yz) plane with seven GHz common BW is shown in Figure 8.19. The realized gain plot of the MRAA in $\phi = 90^o$ (yz) plane is shown in Figure 8.20. The realized gain values in all the three directions in $\phi = 90^o$ (yz) plane is shown in Figure 8.21. The loss of gain in broadside direction may be attributed to the losses in CPW feeding.

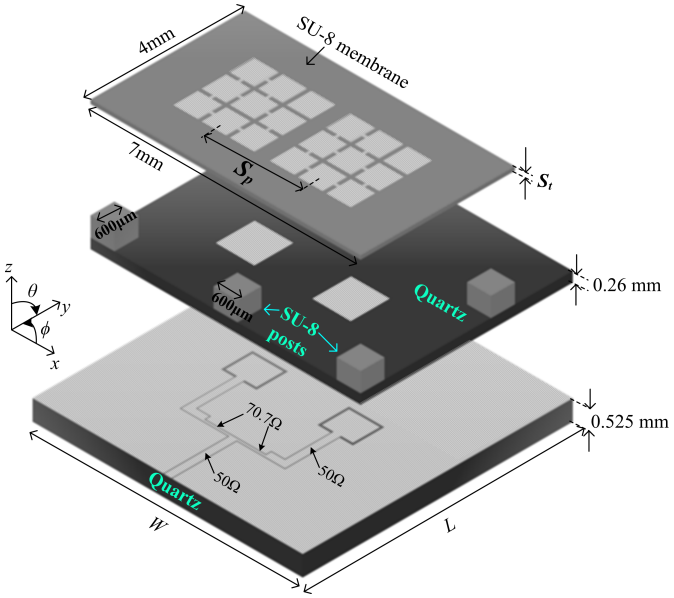

Fig. 8.17: Schematic depicting 3-D drawing of the 60 GHz MRAA (For the sake of illustration, the SU-8 membrane is suspended on top of the patch metallization).

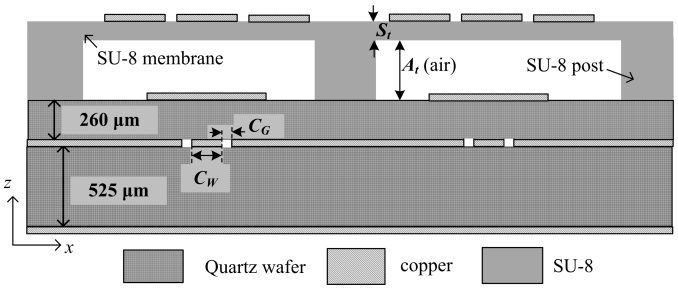

Fig. 8.18: Schematic depicting side-view of 60 GHz MRAA.

Table 8.3: Switch configurations of the 60 GHz MRAA obtained from GA to result in three different beam directions (0 and 1 correspond to OFF and ON states, respectively).

Switch number	*1*	*2*	*3*	*4*	*5*	*6*	*7*	*8*	*9*	*10*	*11*	*12*
$\phi = 0^o; \theta = 0^o$	0	0	0	0	0	0	0	0	0	0	0	0
$\phi = 90^o; \theta = 30^o$	1	1	0	1	0	1	1	0	1	1	1	1
$\phi = 90^o; \theta = -30^o$	1	0	1	1	1	0	1	1	1	1	1	0

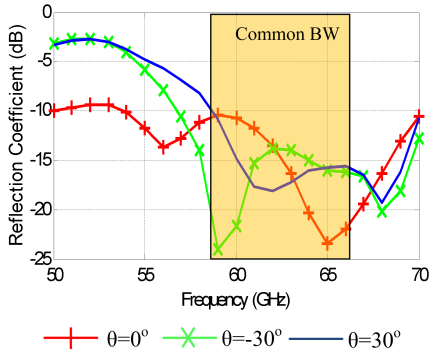

Fig. 8.19: The simulated reflection coefficient of the MRAA in $\phi = 90^o$ (yz) plane.

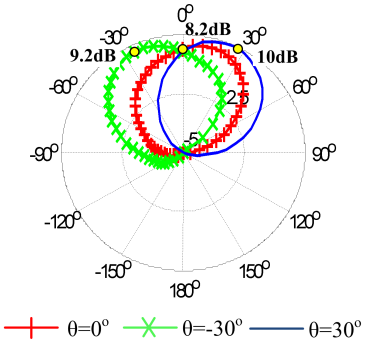

Fig. 8.20: The simulated total realized gain plot (in dB) of the MRAA at 62.5 GHz in $\phi = 90^o$ (yz) plane.

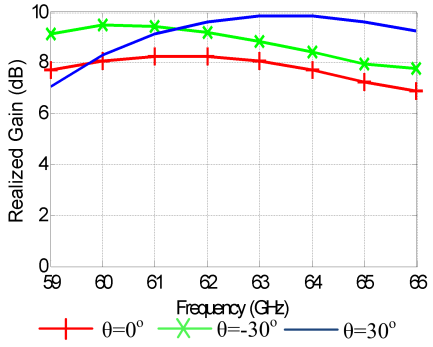

Fig. 8.21: The simulated realized gain values over 59-66 GHz band for three directions $\theta \in -30^o, 0^o, 30^o$ in $\phi = 90^o$ plane.

Chapter 9

Conclusions and Future Work

The design, fabrication, test, and characterization of a multi-band antenna capable of operating over 220, 470, 800, and 4900 MHz bands to enhance multi-band multi-mode communications is accomplished. Two MEMS switches are integrated into this design for reconfigurability. To increase the capacity of a PS MIMO system which inturn enhances its spectral efficiency, the design, fabrication, test, and impedance characterization of beam-steering MRA operating at 4.99 GHz is completed. The radiation pattern measurement and characterization of the MRA targetting nine different beam directions over the 4.94-4.99 GHz band is pending. The design of beam steering MRA and 2 x 1 MRAA for WiGig applications is accomplished. Ideal switches were used in this work to demonstrate beam tilting capabilities in the 60 GHz band. The micro-fabrication, measurement, and characterization of the designs constitute the future work.

References

[1] J. H. Winters, "On the capacity of radio communication systems with diversity in a rayleigh fading environment," *IEEE Journal on Selected Areas in Communications*, vol. 5, no. 5, pp. 871–878, 1987.

[2] P. N. Fletcher, M. Dean, and A. R. Nix, "Mutual coupling in multi-element array antennas and its influence on mimo channel capacity," *Electronics Letters*, vol. 39, no. 4, pp. 342–344, 2003.

[3] "Special issue on multi-function antennas and antenna systems," *IEEE Transactions on Antennas and Propagation*, vol. 52, no. 10, pp. 2807–2807, 2004.

[4] B. A. Cetiner, J. Y. Qian, H. P. Chang, M. Bachman, G.-P. Li, and F. De Flaviis, "Monolithic integration of RF MEMS switches with a diversity antenna on PCB substrate," *IEEE Transactions on Microwave Theory and Techniques*, vol. 51, no. 1, pp. 332–335, 2003.

[5] L. N. Pringle, P. H. Harms, S. P. Blalock, G. N. Kiesel, E. J. Kuster, P. G. Friederich, R. J. Prado, J. M. Morris, and G. S. Smith, "A reconfigurable aperture antenna based on switched links between electrically small metallic patches," *IEEE Transactions on Antennas and Propagation*, vol. 52, no. 6, pp. 1434–1445, 2004.

[6] C. J. Hansen, "Wigig: Multi-gigabit wireless communications in the 60 GHz band," *IEEE Wireless Communications*, vol. 18, no. 6, pp. 6–7, Dec. 2011.

[7] J.-S. Chen, "Multi-frequency characteristics of annular-ring slot antennas," *Microwave and Optical Technology Letters*, vol. 38, no. 6, pp. 506–511, 2003.

[8] F. Croq and D. M. Pozar, "Multi-frequency operation of microstrip antennas using aperture-coupled parallel resonators," *IEEE Transactions on Antennas and Propagation*, vol. 40, no. 11, pp. 1367–1374, 1992.

[9] F. Le Bolter and A. Louzir, "Multi-band annular slot antenna for WLAN applications," in *Proceedings of the Eleventh International Conference on Antennas and Propagation (IEE Conference Publication No. 480)*, vol. 2, pp. 529–532, 2001.

[10] H. Tehrani, T.-Y. Yun, and K. Chang, "A multi-frequency microstrip-fed shorted square ring slot line antenna," in *Proceedings of the International Symposium Antennas and Propagation Society, IEEE*, vol. 2, pp. 920–923, 1999.

[11] H. Tehrani and K. Chang, "A multi-frequency microstrip-fed annular slot antenna," in *Proceedings of the Antennas and Propagation Society International Symposium, IEEE*, vol. 2, pp. 632–635, 2000.

[12] C. Puente-Baliarda, J. Romeu, R. Pous, and A. Cardama, "On the behavior of the SIERPINSKI multi-band fractal antenna," *IEEE Transactions on Antennas and Propagation*, vol. 46, no. 4, pp. 517–524, 1998.

[13] H. Mopidevi, D. Rodrigo, O. Kaynar, L. Jofre, and B. A. Cetiner, "Compact and broadband antenna for LTE and public safety applications," *Antennas and Wireless Propagation Letters, IEEE*, vol. 10, pp. 1224–1227, 2011.

[14] B.-C. Kim, J. D. Park, and H. D. Choi, "Tapered type PIFA design for mobile phones at 1800 MHz," in *Proceedings of the 57th IEEE Semiannual Vehicular Technology Conference, VTC-Spring*, vol. 2, pp. 1012–1014, Apr. 2003.

[15] F. Wang, Z. Du, Q. Wang, and K. Gong, "Enhanced-bandwidth PIFA with T-shaped ground plane," *Electronics Letters*, vol. 40, no. 23, pp. 1504–1505, 2004.

[16] A. Khoshniat, H. S. Mopidevi, and B. A. Cetiner, "Broadband capacitively fed tapered type PIFA with modified ground plane," *Electronics Letters*, vol. 46, no. 7, pp. 474–475, 2010.

[17] B. A. Cetiner, G. R. Crusats, L. Jofre, and N. Biyikli, "RF MEMS integrated frequency reconfigurable annular slot antenna," *IEEE Transactions on Antennas and Propagation*, vol. 58, no. 3, pp. 626–632, 2010.

[18] M. Unlu, Y. Damgaci, H. S. Mopidevi, O. Kaynar, and B. A. Cetiner, "Reconfigurable, tri-band RF MEMS PIFA antenna," in *Proceedings of the IEEE International Symposium on Antennas and Propagation (APSURSI)*, pp. 1563–1565, 2011.

[19] M. Unlu, H. Mopidevi, A. Zohur, and B. A. Cetiner, "Frequency reconfigurable, 220 - 5000 MHz, five-band RF MEMS PIFA," in *Proceedings of the IEEE 55th International Midwest Symposium on Circuits and Systems (MWSCAS)*, pp. 65–68, 2012.

[20] S.-H. Hsu, Y.-J. Ren, and K. Chang, "A dual-polarized planar-array antenna for S-band and X-band airborne applications," *Antennas and Propagation Magazine, IEEE*, vol. 51, no. 4, pp. 70–78, 2009.

[21] S. Zhong, Z. Sun, and X. Tang, "Progress in dual-band dual-polarization shared-aperture SAR antennas," *Frontiers of Electrical and Electronic Engineering in China*, vol. 4, no. 3, pp. 323–329, 2009.

[22] D. Rodrigo, Y. Damgaci, M. Unlu, B. A. Cetiner, J. Romeu, and L. Jofre, "Antenna reconfigurability based on a novel parasitic pixel layer," in *Proceedings of the 5th European Conference on Antennas and Propagation (EUCAP)*, pp. 3497–3500, 2011.

[23] X. Yuan, Z. Li, D. Rodrigo, H. S. Mopidevi, O. Kaynar, L. Jofre, and B. A. Cetiner, "A parasitic layer-based reconfigurable antenna design by multi-objective optimization," *IEEE Transactions on Antennas and Propagation*, vol. 60, no. 6, pp. 2690–2701, 2012.

[24] T. Seki, N. Honma, K. Nishikawa, and K. Tsunekawa, "A 60-GHz multi-layer parasitic microstrip array antenna on LTCC substrate for system-on-package," *IEEE Microwave and Wireless Components Letters*, vol. 15, no. 5, pp. 339–341, May 2005.

[25] Y.-P. Zhang, M. Sun, K. M. Chua, L. L. Wai, D. Liu, and B. P. Gaucher, "Antenna-in-package in LTCC for 60-GHz radio," in *Proceedings of the International Workshop on Antenna Technology: Small and Smart Antennas Metamaterials and Applications, IWAT*, pp. 279–282, Mar. 2007.

[26] S.-H. Wi, Y.-B. Sun, I.-S. Song, S.-H. Choa, I.-S. Koh, Y.-S. Lee, and J.-G. Yook, "Package-level integrated antennas based on LTCC technology," *IEEE Transactions on Antennas and Propagation*, vol. 54, no. 8, pp. 2190–2197, Aug. 2006.

[27] S. Seok, N. Rolland, and P.-A. Rolland, "Millimeter-wave quarter-wave patch antenna on benzocyclobutene polymer," in *Proceedings of the 38th European Microwave Conference*, pp. 1018–1021, Oct. 27–31, 2008.

[28] A. Campo and C. Greiner, "SU-8: a photoresist for high-aspect-ratio and 3-D submicron lithography," *Journal of Micromechanics and Microengineering*, vol. 17, pp. R81–R95, 2007.

[29] G. P. Gauthier, A. Courtay, and G. M. Rebeiz, "Microstrip antennas on synthesized low dielectric-constant substrates," *IEEE Transactions on Antennas and Propagation*, vol. 45, no. 8, pp. 1310–1314, Aug. 1997.

[30] D. R. Jackson, J. T. Williams, and A. K. Bhattacharyya, "Microstrip patch designs that do not excite surface waves," *IEEE Transactions on Antennas and Propagation*, vol. 41, pp. 1026–1037, Aug. 1993.

[31] Z. Li, D. Rodrigo, L. Jofre, and B. A. Cetiner, "A new class of antenna array with a reconfigurable element factor," *IEEE Transactions on Antennas and Propagation*, vol. 61, no. 4, pp. 1947–1955, Apr. 2013.

[32] S. Sesia, I. Toufik, and M. Baker, *Analysis, Design, and Measurement of Small Low Profile Antennas*. Norwood, MA: Artech House, 2009.

[33] K. Hirasawa and M. Haneishi, *LTE: The UMTS Long Term Evolution*. Wiley Online Library, 1993.

[34] B.-C. Kim, J. D. Park, and H. D. Choi, "Tapered type PIFA design for mobile phones at 1800 MHz," in *Proceedings of the 57th IEEE Semiannual Vehicular Technology Conference, VTC-Spring*, vol. 2, pp. 1012–1014, Apr. 2003.

[35] R.-A. Bhatti, S. Yi, and S.-O. Park, "Compact antenna array with port decoupling for LTE-standardized mobile phones," *Antennas and Wireless Propagation Letters, IEEE*, vol. 8, pp. 1430–1433, 2009.

[36] D. Yuan, Z. Du, K. Gong, and Z. Feng, "A novel dual-band printed diversity antenna for mobile terminals," *IEEE Transactions on Antennas and Propagation*, vol. 55, no. 7, pp. 2088–2096, 2007.

[37] X. Song, J. Fu, and W. Wang, "Design of a dual band and broadband microstrip monopole antenna," in *Proceedings of the 8th International Symposium on Antennas, Propagation, and EM Theory, ISAPE*, pp. 237–239, 2008.

[38] C.-Y. Pan, T.-S. Horng, W.-S. Chen, and C.-H. Huang, "Dual wideband printed monopole antenna for WLAN/WIMAX applications," *Antennas and Wireless Propagation Letters, IEEE*, vol. 6, pp. 149–151, 2007.

[39] G. A. E. Vandenbosch, "Capacitive matching of microstrip antennas," *Electronics Letters*, vol. 31, no. 18, pp. 1535–1536, 1995.

[40] Ansoft HFSS, Ansoft Corporation, Canonsburg, PA. [Online]. Available: http://www.ansoft.com, 2007.

[41] P. Miskovsky, J. M. Gonzalez-Arbesu, and J. Romeu, "Antenna radiation efficiency measurement in an ultrawide frequency range," *Antennas and Wireless Propagation Letters, IEEE*, vol. 8, pp. 72–75, 2009.

[42] B. A. Cetiner, H. Jafarkhani, J.-Y. Qian, H. J. Yoo, A. Grau, and F. De Flaviis, "Multifunctional reconfigurable MEMS integrated antennas for adaptive MIMO systems," *Communications Magazine, IEEE*, vol. 42, no. 12, pp. 62–70, Dec. 2004.

[43] F. Yang and Y. Rahmat-Samii, "Patch antennas with switchable slots (PASS) in wireless communications: concepts, designs, and applications," *Antennas and Propagation Magazine, IEEE*, vol. 47, no. 2, pp. 13–29, Apr. 2005.

[44] S. Yang, C. Zhang, H. K. Pan, A. E. Fathy, and V. K. Nair, "Frequency-reconfigurable antennas for multi-radio wireless platforms," *Microwave Magazine, IEEE*, vol. 10, no. 1, pp. 66–83, Feb. 2009.

[45] E. Erdil, K. Topalli, M. Unlu, O. A. Civi, and T. Akin, "Frequency tunable microstrip patch antenna using RF MEMS technology," *IEEE Transactions on Antennas and Propagation*, vol. 55, no. 4, pp. 1193–1196, Apr. 2007.

[46] HFSS v12, Ansoft Corporation, Pittsburgh, PA, USA, 2002.

[47] Radant MEMS, Stow, MA, USA. [Online]. Available: http://www.radantmems.com/.

[48] G. H. Huff and J. T. Bernhard, "Integration of packaged RF MEMS switches with radiation pattern reconfigurable square spiral microstrip antennas," *IEEE Transactions on Antennas and Propagation*, vol. 54, no. 2, pp. 464–469, Feb. 2006.

[49] M. Unlu, Y. Damgaci, H. S. Mopidevi, O. Kaynar, and B. A. Cetiner, "Reconfigurable, tri-band RF MEMS PIFA antenna," in *Proceedings of the IEEE International Symposium on Antennas and Propagation (APSURSI)*, pp. 1563–1565, July 2011.

[50] ANSYS HFSS, version 13.0, Ansoft Corporation, build: July 18 2007. [Online]. Available: http://www.ansoft.com.

[51] T. Huynh and K.-F. Lee, "Single-layer single-patch wideband microstrip antenna," *Electronics Letters*, vol. 31, no. 16, pp. 1310–1312, Aug. 1995.

[52] ROHACELL HF foam, Evonik Industries AG, Rellinghauser Strabe111, 45128 Essen, Germany.

[53] ANSYS HFSS ver. 13.0, Ansoft Corporation, Canonsburg, PA, USA, July 18, 2007. [Online]. Available: http://www.ansoft.com.

[54] Y. Saito and T. Fukusako, "Low-profile and electrically small meander-line antenna using a capacitive feed structure," *Antennas and Wireless Propagation Letters, IEEE*, vol. 11, pp. 1281–1284, 2012.

[55] P. M. Zavracky, N. E. McGruer, R. H. Morrison, and D. Potter, "Microswitches and microrelays with a view toward microwave application," *International Journal on RF and Microwave Computer-Aided Engineering*, vol. 9, pp. 338–347, 1999.

[56] N. E. McGruer, P. M. Zavracky, R. Morrison, S. Majumder, D. Potter, and M. Schirmer, "RF and current handling performance of electrostatically actuated microswitches," in *Proceedings of the Sensors Exposition, Cleveland, OH*, Sept. 1999.

[57] SMP1345 Pin Diode, Skyworks, Woburn, MA. [Online]. Available: http://www.skyworksinc.com/uploads/documents/200046M.pdf.

[58] ANSYS HFSS ver. 14.0, Ansys Corporation, build: October 22, 2011. [Online]. Available: http://www.ansys.com.

[59] D. M. Pozar, *Microwave Engineering, 4th edition.* Hoboken: John Wiley & Sons, 2012.

[60] K. Deb, A. Pratap, S. Agarwal, and T. Meyarivan, "A fast and elitist multi-objective genetic algorithm: NSGA-II," *IEEE Transactions on Evolutionary Computation*, vol. 6, no. 2, pp. 182–197, Apr. 2002.

[61] S.-W. Lu, T.-F. Huang, and P. Hsu, "CPW-fed slot-loop coupled patch antenna on narrow substrate," *Electronics Letters*, vol. 35, no. 9, pp. 682–683, 29 Apr. 1999.

[62] H. C. Liu, T. S. Horng, and N. G. Alexopoulos, "Radiation from aperture antennas with a coplanar waveguide feed," in *Proceedings of the IEEE Antennas and Propagation Society Symposium Digital Archive*, pp. 1820–1823, 1992.

[63] R. Q. Lee, K. F. Lee, and J. Bobinchak, "Characteristics of a two-layer electromagnetically coupled rectangular patch antenna," *Electronics Letters*, vol. 23, no. 20, pp. 1070–1072, 24 Sept. 1987.

[64] *Microstrip Antenna Design Handbook.* Boston: Artech House, 2001.

[65] A. Y. Simba, M. Yamamoto, T. Nojima, and K. Itoh, "Planar-type sectored antenna based on slot yagi–uda array," *IEE Proceedings-Microwaves, Antennas and Propagation*, vol. 152, no. 5, pp. 347–353, 2005.

Vita

Hema Swaroop Mopidevi

Patent

- Broadband Antenna Systems and Methods - Inventors: Cetiner, B.A.; Mopidevi, H.; Rodrigo, D.; Jofre, L.; US 2013/0120213 A1, May 2013.

Published and Prepared Journal Articles

- Reduced Overhead Training for Multi Reconfigurable Antennas with Beam-Tilting Capability, Eslami, H.; Sukumar, C.P.; Rodrigo, D.; Mopidevi, S.; Eltawil, A.M.; Jofre, L.; Cetiner, B.A., *IEEE Transactions on Wireless Communications*, vol. 9, no. 12, pp. 3810-3821, Dec. 2010.

- Broadband capacitively fed tapered type PIFA with modified ground plane, Khoshniat, A.; Mopidevi, H.S.; Cetiner, B.A., *Electronics Letters*, vol. 46, no. 7, pp. 474-475, Apr. 2010.

- Compact and Broadband Antenna for LTE and Public Safety Applications, Mopidevi, H.; Rodrigo, D.; Kaynar, O.; Jofre, L.; Cetiner, B.A., *Antennas and Wireless Propagation Letters, IEEE*, vol. 10, pp. 1224-1227, 2011.

- A Parasitic Layer-Based Reconfigurable Antenna Design by Multi-Objective Optimization, Xiaoyan Yuan; Zhouyuan Li; Rodrigo, D.; Mopidevi, H.S.; Kaynar, O.; Jofre, L.; Cetiner, B.A., *IEEE Transactions on Antennas and Propagation*, vol. 60, no. 6, pp. 2690-2701, June 2012.

- Beam-steering antenna based on parasitic layer, Li, Z.; Mopidevi, H.; Kaynar, O.; Cetiner, B.A., *Electronics Letters*, vol. 48, no. 2, pp. 59-60, Jan. 2012.

- RF MEMS Reconfigurable Two-Band Antenna, Zohur, A.; Mopidevi, H.; Rodrigo, D.; Unlu, M.; Jofre, L.; Cetiner, B.A., *Antennas and Wireless Propagation Letters, IEEE*, vol. 12, pp. 72-75, 2013.

- A Quad band antenna for Public Safety Applications, Mopidevi, H.; Damgaci, Y.; Rodrigo, D.; Jofre, L.; Cetiner, B.A., *Antennas and Wireless Propagation Letters, IEEE*, vol. 13, pp. 1231-1234, 2014.

- Three-dimensional micro-fabricated broadband patch antenna for WiGig applications, Mopidevi, H.; Hunerli, H.V.; Cagatay, E.; Biyikli, N.; Imbert, M.; Romeu, J.; Jofre, L.; Cetiner, B.A., *Antennas and Wireless Propagation Letters, IEEE*, vol. 13, pp. 828-831, 2014.

- Pattern Reconfigruable Antenna for Public Safety applications, Mopidevi, H.; Rodrigo, D.; Jofre, L.; Cetiner, B.A., *To be submitted to IEEE Transactions on Antennas and Propagation*, 2014.

- Broadband beam steering MRA for 60 GHz communications, Mopidevi, H.; Hunerli, H.V.; Biyikli, N.; Imbert, M.; Romeu, J.; Jofre, L.; Cetiner, B.A., *To be submitted to IEEE Transactions on Antennas and Propagation*, 2014.

Published Conference Papers

- RF-N/MEMS integrated reconfigurable antenna for public safety applications, Yuan, X.; Damgaci, Y.; Mopidevi, H.; Cetiner, B.A., in *Proceedings of the Antennas and Propagation Society International Symposium*, pp. 1-4, June 2009.

- MEMS integrated reconfigurable antenna for cognitive public safety radios, Khoshniat, A.; Mopidevi, H.; Damgaci, Y.; Rodrigo, D.; Jofre, L.; Cetiner, B.A., in *Proceedings of the Fourth European Conference on Antennas and Propagation (EuCAP)*, pp.1-3, Apr. 2010.

- Reconfigurable, tri-band RF MEMS PIFA antenna, Unlu, M.; Damgaci, Y.; Mopidevi, H.S.; Kaynar, O.; Cetiner, B.A., in *Proceedings of the IEEE International Symposium on Antennas and Propagation (APSURSI)*, pp. 1563-1565, July 2011.

- Frequency reconfigurable, 220-5000 MHz, five-band RF MEMS PIFA, Unlu, M.; Mopidevi, H.; Zohur, A.; Cetiner, B.A., in *Proceedings of the 55th International Midwest Symposium on Circuits and Systems (MWSCAS), IEEE*, pp. 65-68, Aug. 2012.